

UNDERSTANDING THE FORMATION
OF MAGNETIC FIELD AND PLASMA
STRUCTURES IN THE MAGNETOTAIL
VIA THE RECONNECTION PROCESS

Segheen Beyene

Mullard Space Science Laboratory
Department of Space and Climate Physics
University College London

A thesis submitted to UCL for the degree of Doctor of Philosophy

March 2013

I, Segheen Beyene, confirm that the work presented in this thesis is my own. Where information has been derived from other sources, I confirm that this has been indicated in the thesis.

Signed:

The first study of the thesis has been previously published:

Beyene, S., Owen, C. J., Walsh, A. P., Forsyth, C., Fazakerley, A. N., Kiehas, S., Dandouras, I., and Lucek, E.: Cluster observations of a transient signature in the magnetotail: implications for the mode of reconnection, *Ann. Geophys.*, 29, 2131-2146, doi:10.5194/angeo-29-2131-2011, 2011

Abstract

This thesis studies the formation of products of magnetotail reconnection using models and observations. Three studies are presented, the first is an analysis of observations from the Cluster spacecraft, located in different regions of the magnetotail, which allow simultaneous sampling of a Travelling Compression Region (TCR) in the lobe and the underlying magnetic structure in the plasma sheet causing it. Previous work suggests that these structures are created by either single-X-line time-dependent reconnection, forming a flux-bulge, or multiple-X-line reconnection, forming a flux-rope. The observations are analysed and compared to the predictions of these models to determine which mode of reconnection created the structure.

The second study presents an adaptation to a single particle model of time-dependent reconnection in the magnetotail previously published by Owen and Cowley (1987). This new model relaxes the cold plasma approximation and assesses the stress balance conditions on reconnected field lines threading the current sheet when the outflow particles have a perpendicular pressure. This is modeled as a result of pitch angle scattering of field-aligned inflow particles as they cross the current sheet on hairpin-like reconnected field lines. The new results show that this accounts for a flux-bulge and a TCR which is consistent with observations.

The third study presents a numerical particle model which simulates the evolution of a plasmoid, modeled as a single magnetic field loop in the

magnetotail. The model magnetotail has a magnetic, density and velocity gradient along the tail axis. The plasma within the plasmoid splits into two groups, the movement of these groups causes the plasmoid size to oscillate. The initial tailward movement of the plasmoid is caused by the magnetic gradient but continues in its absence due to the net momentum of the plasma inside the plasmoid, with the tailward travelling particles travel faster than the Earthward travelling particles.

Acknowledgements

Firstly I would like to thank my supervisors, Professors Chris Owen and Andrew Fazakerley for their help and guidance over the years. Thank you to my parents for everything before and during the PhD, they went above and beyond their parental duty and I am very grateful of that. Thank you to my sister Melei for all of the help, knowledge and for looking out for me during the early years. Thank you to my brother, Aflay for the times he cooked dinner, for bringing me along to the Jay-Z and Kanye West concert and for being someone to hang out with during the breaks between work. Thank you to my sister Settiti for the long talks about music and TV shows and the healthy eating and travelling you do that is inspiring. Thank you to my brother-in-law, Hermon, for helping me perfect the personal statement of my PhD application and for helping me with my car troubles.

Thank you to Phillip Hunt for all the help during the undergrad days. Thank you to my office mates, Andrew Walsh, Colin Forsyth and Roger Duthie for answering my many questions. Thank you to all of the people who drove me to and from the lab: Kimberly Steed, Annie Wellbrock, Sheila Kanani, Missagh Medipour, Ehsan Pedram, Awat Rahimi & Paul Prior. Thank you to Dr. Stefan Kiehas, Dr. Elizabeth Lucek, Dr. Iannis Dandouras for helping on the first study and to the teams behind the Cluster Active Archive, the QSAS software and the CIS, PEACE and FGM instruments of Cluster. Finally, I would like to thank the Science and Technology Funding Council (STFC) for funding my PhD.

Contents

Abstract	3
Acknowledgements	5
Contents.....	6
List of Figures	9
List of Tables.....	11
List of Acronyms.....	11
1 Introduction.....	12
1.1 Plasma Physics	13
1.1.1 Plasma	13
1.1.2 Single particle motion	15
1.1.3 Kinetic Theory	22
1.1.4 MagnetoHydroDynamics (MHD).....	23
1.2 Magnetospheric Physics	30
1.2.1 Coordinate systems	30
1.2.2 Solar Wind.....	31
1.2.3 Magnetosphere	32
1.2.4 Dungey Cycle.....	42
1.2.5 NENL model of Substorms.....	45
1.2.6 Travelling Compression Regions.....	47
1.3 Modes of Reconnection.....	50
1.3.1 Multiple X-line Reconnection (MXR).....	50
1.3.2 MHD Model of Time Dependent Reconnection.....	54
1.3.3 Cold Particle Model of Time Dependent Reconnection	60
2 Cluster Observations of a Transient Signature in the Magnetotail: Implications for the Mode of Reconnection	62
2.1 Introduction	62
2.2 Comparison of the Reconnection Products	64

2.3	Instrumentation.....	65
2.3.1	FGM	66
2.3.2	PEACE	67
2.3.3	CIS.....	71
2.3.4	Cluster location and separation	73
2.4	Observations	74
2.5	Analysis	89
2.5.1	Orientation of Magnetic Structure	89
2.5.2	Velocity Calculation.....	90
2.5.3	Configuration in MVA derived co-ordinate system	93
2.5.4	Observations in MVA derived co-ordinate system.....	95
2.6	Discussion.....	99
2.6.1	Interpretation of observations	99
2.6.2	Multiple-X-line Reconnection Interpretation	104
2.6.3	Time Dependent Reconnection Interpretation	105
2.7	Conclusions	106
	Chapter 3	108
3	Modelling the Effects of Time-Varying Reconnection Leading to the Formation of Travelling Compression Regions in the Magnetotail	108
3.1	Introduction	108
3.1.1	Comparison of the two existing models.....	109
3.2	Cold Particle Model of Time-Dependent Reconnection.....	110
3.2.1	Marginal Firehose Stability Equation	110
3.2.2	Frames of Reference	113
3.2.3	Separatrix Height	116
3.2.4	Height of PO boundary	120
3.3	A New Hot Particle Model of Time-Dependent Reconnection ...	124
3.3.1	Horizontal Stress balance.....	124
3.3.2	Vertical Pressure Balance	131

3.3.3	Magnetic Signature	135
3.4	Results	137
3.4.1	Model Specifications.....	137
3.4.2	Outgoing velocity	138
3.4.3	Structure of the tail.....	140
3.4.4	Variations in the magnetic field signatures with height	143
3.4.5	Lobe Compression	146
3.4.6	Evolution with time after reconnection ceases	148
3.5	Discussion.....	151
3.6	Conclusion	160
4	Plasmoid Evolution in a Simple Numerical Particle Simulation	163
4.1	Introduction	163
4.2	Model.....	166
4.2.1	Plasmoid Specifics	166
4.2.2	Stress Balance for Multi Speed Particles	169
4.2.3	Tracking	173
4.2.4	Model Specifications.....	176
4.3	Results	180
4.4	Discussion.....	191
4.5	Conclusions	202
5	Conclusions and Future Work	205
5.1	Conclusions	205
5.2	Future work	210
6	Appendix.....	213
6.1	Bipolar signature database.....	213
6.2	Distribution Functions.....	215
6.3	Stress Balance.....	218
6.4	Forces at an interface.....	219

6.5	Solution to Cubic Equation	221
7	Bibliography	223

List of Figures

Figure 1:	Magnetic Reconnection.	28
Figure 2:	Magnetic Reconnection Models	29
Figure 3:	Parker spiral.....	32
Figure 4:	The Magnetosphere.	35
Figure 5:	The Plasma Mantle.	40
Figure 6:	The Velocity Filter Effect.....	42
Figure 7:	The Dungey Cycle.....	44
Figure 8:	Substorm Phases.....	46
Figure 9:	Travelling Compression Region.....	49
Figure 10:	Multiple X-Line Reconnection.....	51
Figure 11:	Flux Rope Magnetic Signature.....	52
Figure 12:	Time Dependant Reconnection	55
Figure 13:	Flux Bulge Magnetic Signature 1.....	58
Figure 14:	Flux Bulge Magnetic Signature 2.....	59
Figure 15:	Cold Particle Model in the Magnetotail	61
Figure 16:	Top Hat Analyser	67
Figure 17:	Spacecraft Position.	74
Figure 18:	Multi-Spacecraft Observations.....	75
Figure 19:	C2 observations	78
Figure 20:	C4 observations.	81
Figure 21:	C1 observations	84
Figure 22:	C3 observations	87

Figure 23: Spacecraft Configuration in the MVA Co-ordinate	94
Figure 24: Observations in the MVA co-ordinate system	96
Figure 25: Results Diagram.	104
Figure 26: Cold Particle Model in Velocity Space	114
Figure 27: Cold Particle Model Lobe	117
Figure 28: Cold Particle Model PO region.	121
Figure 29: Hot Particle Model in Velocity Space.....	125
Figure 30: Velocity vs Pitch angle.....	130
Figure 31: Hot Particle Model PO region	131
Figure 32: Outflow Velocity in Earth's Rest Frame vs Pitch Angle	139
Figure 33: Shape of PO region.....	140
Figure 34: Flux Bulge Magnetic Signature: Variations With Height 1....	144
Figure 35: Flux Bulge Magnetic Signature: Variations With Height 2....	145
Figure 36: $\Delta B/B$ % vs pitch angle	146
Figure 37 Magnetic Signature of Flux Bulge: Variations With Time 1 ...	149
Figure 38: Magnetic Signature of Flux Bulge: Variations With Time 2..	151
Figure 39: Plasmoid	164
Figure 40: Magnetic Loop Representing the Plasmoid	167
Figure 41: Particle Tracking	174
Figure 42: Plasmoid Parameters vs Downtail Distance.....	182
Figure 43: Plasmoid Parameters vs Time.	184
Figure 44: Particle Velocity Plot 1.....	186
Figure 45: Particle Velocity Plot 2.....	189
Figure 46: Field Line Kink.....	219

List of Tables

Table 1: Magnetotail Values Pre and Post Plasma Region Expansion..... 148
Table 2: List of dates and times of bipolar signatures 1. 213
Table 3: List of dates and times of bipolar signatures 2. 214

List of Acronyms

PO regionPlasma Outflow Region
NENL.....Near Earth Neutral Line
NEML.....Near Earth Magnetic Loop end
DNL.....Distant Neutral Line
DML.....Distant Magnetic Loop end
MXR.....Multiple-X-Line Reconnection
TDR.....Time Dependent reconnection
O&C87.....Owen and Cowley 1987 paper

Chapter 1

Introduction

Magnetic reconnection is a key process in magnetotail dynamics. It facilitates the interaction of the solar wind with the magnetosphere which leads to several magnetospheric phenomena. Magnetic flux from the solar wind is added to the magnetosphere on the dayside and magnetic flux is removed from the magnetosphere on the nightside, in both cases by magnetic reconnection. Yet there are many unanswered questions about the process, some of which, may be answered by the study of the magnetic structures found within the magnetosphere which are thought to be created by reconnection. In this thesis, magnetic structures were observed, modeled and analysed to increase our understanding of the process of magnetic reconnection. The products themselves are also worthy of study in their own right; the knowledge of these structures and their evolution is not complete due to limited spacecraft observation and spacecraft range. In this thesis, these are modeled to gain a complete picture of the structures and to investigate how they evolve with time. Gaining knowledge of magnetic reconnection, its products and their evolution will lead to a more complete picture of magnetotail dynamics.

1.1 Plasma Physics

1.1.1 Plasma

A plasma is quasi-neutral gas of ionised particles that exhibits collective behavior. A plasma is formed when a neutral gas is heated to the extent that the random thermal energy is greater than the potential energy associated with the attractive force between ions and electrons. Each atom splits into one ion and one or more electrons. As the initial charge is zero, the sum of the separated charged particles is also zero. At small scales, the gas is charged due to the separate ions and electrons that make up the plasma, but on larger scales these charges cancel out leaving no net charge; this is a characteristic of plasma called quasi-neutrality.

1.1.1.1 Debye shielding

If a plasma gains a net charge in a region, the particles of opposite charge will be attracted to that region, this has the effect of moving the system back towards neutrality. This process is called Debye shielding. The electric potential experienced by a particle a distance r from another particle with a charge q is known as the coulomb potential and is:

$$\Phi_C(r) = \frac{q}{4\pi\epsilon_0 r} \quad (1.1)$$

where ϵ_0 is the permittivity of free space. In a plasma, the potential experienced by a particle a distance r from another particle is reduced due to Debye shielding, the resulting potential is known as the Debye potential and is:

$$\Phi_D(r) = \frac{q}{4\pi\epsilon_0 r} e^{-\frac{r}{\lambda_D}} \quad (1.2)$$

where λ_D is the Debye length (the length scale on which Debye shielding occurs). The equation for the Debye length is:

$$\lambda_D = \left(\frac{\epsilon_0 k T_e}{n_e q_e^2} \right)^{\frac{1}{2}} \quad (1.3)$$

where k is Boltzmann's constant, T_e is the electron temperature and n_e is the electron density (assuming $n_e \sim n_i$ and $T_e \sim T_i$). The equation is written in terms of the electron parameters rather than those of the ions as electrons are more mobile and respond much more quickly in the presence of unbalanced charges. An ionised gas can be considered as quasi-neutral if:

$$L \gg \lambda_D \quad (1.4)$$

the length scale of the gas, L , is much larger than the Debye length. For ionised gases of length scales near the Debye length, separate charges would be observed whereas on larger scales the charges cancel out and hence the gas is quasi-neutral. This is one of three criteria that must be met for an ionised gas to be quasi-neutral and hence to be considered a plasma. The second plasma criteria is related to the number of particles within the Debye sphere, which is a sphere of radius λ_D centred on an unshielded charge. Electrons less than the Debye length away from an unshielded charge (and hence within the Debye sphere) will move to shield the charge, the number of these electrons is given by N_D . The second plasma criteria requires a large number of electrons (within the Debye sphere) taking part in Debye shielding:

$$N_D = \frac{4\pi}{3} n_e \lambda_D^3 \gg 1 \quad (1.5)$$

The third plasma criteria is related to the plasma frequency. If the plasma is perturbed, and thus the quasi-neutrality is disturbed, the particles will react and redistribute to return towards neutrality. As the electrons are more mobile than the ions, the ions are relatively still and the electrons oscillate around them. The frequency of this oscillation is called the electron plasma frequency and is equal to:

$$\omega_{pe} = \left(\frac{n_e q_e^2}{m_e \epsilon_0} \right)^{\frac{1}{2}} \quad (1.6)$$

For the electrons to be unaffected by the collisions with neutrals, the average time between two electron-neutral collisions τ_n must be larger than the inverse of the plasma frequency:

$$\omega_{pe} \tau_n \gg 1 \quad (1.7)$$

1.1.2 Single particle motion

There are several methods used to understand the dynamics of plasmas. The simplest method involves use of single charged particle physics, which involves tracking each particle by solving its equations of motion. In space plasmas, the mean free path is generally large and hence the effects of collisions between particles can be ignored, only the effect of the electric and magnetic fields on each particle need be considered.

1.1.2.1 Particle Motion in a Uniform Magnetic Field

If a particle with charge q , velocity \mathbf{v} and mass m experiences an electric field \mathbf{E} and magnetic field \mathbf{B} , the equation of motion is:

$$m \frac{d\mathbf{v}}{dt} = q(\mathbf{E} + \mathbf{v} \times \mathbf{B}) \quad (1.8)$$

If the electric field is zero and the magnetic field is constant and non-zero, differentiating the above equation with respect to time, results in:

$$\frac{d^2\mathbf{v}}{dt^2} = \left(-\frac{qB}{m}\right)^2 \mathbf{v} \quad (1.9)$$

This is the equation for simple harmonic motion; the frequency of oscillation (also known as the gyro-, larmor or cyclotron frequency) is given by:

$$\omega_G = \left(-\frac{qB}{m}\right) \quad (1.10)$$

If the magnetic field is directed along Z then, the simple harmonic oscillator has solutions of the form:

$$x - x_o = r_g \sin \omega_g t \quad (1.11)$$

$$y - y_o = r_g \cos \omega_g t$$

The radius of the gyration (also known as the gyro- or larmor radius) is:

$$r_G = \frac{v_{\perp}}{\omega_G} \quad (1.12)$$

Thus the presence of the magnetic field will cause the particles to gyrate in the plane perpendicular to the magnetic field, around a guiding centre, with a frequency of ω_G and a radius of r_G ; both values depend on charge,

magnetic field strength and mass. If a particle has a constant velocity along the magnetic field (V_{\parallel}) and is gyrating around a guiding centre with a velocity perpendicular to the magnetic field (V_{\perp}), then the resulting motion is helical. The angle between the velocity vector and the magnetic field direction is called the pitch angle α and can be calculated using:

$$\alpha = \arctan\left(\frac{|V_{\perp}|}{|V_{\parallel}|}\right) \quad (1.13)$$

If the pitch angle is 0° or 180° then the particle is moving parallel or anti parallel respectively along the field line. A particle with any other pitch angle has a non-zero perpendicular velocity and thus traces a helical path.

1.1.2.2 $\mathbf{E} \times \mathbf{B}$ drift

If a constant uniform electric field is present in addition to the magnetic field, the particle path will deviate from a simple helix. By differentiating equation 1.8 with respect to time while the electric field is non-zero and constant results in:

$$\frac{d^2\mathbf{v}}{dt^2} = -\omega_G^2\left(\mathbf{v} - \frac{\mathbf{E} \times \mathbf{B}}{B^2}\right) \quad (1.14)$$

$$\frac{d^2\mathbf{v}}{dt^2} = -\omega_G^2(\mathbf{v} - \mathbf{v}_d) \quad (1.15)$$

where \mathbf{v}_d is:

$$\mathbf{v}_d = \frac{\mathbf{E} \times \mathbf{B}}{B^2} \quad (1.16)$$

which is the drift velocity of the guiding centre. For a particle gyrating perpendicular to a magnetic field, the addition of a constant electric field will increase the gyrovelocity and gyroradius for one half of the gyration

and decrease it for the other half compared to the situation without an electric field. The combination of the effects of the two halves causes a net velocity and hence the motion of the guiding centre which is known as $\mathbf{E} \times \mathbf{B}$ drift. Note that this acts perpendicular to both the electric field and magnetic field.

1.1.2.3 Gradient drift

Drift motion can also be caused by a non-uniform magnetic field (e.g. a magnetic field with a gradient, $\nabla B \neq 0$). Assuming the length scale of the magnetic gradient is greater than that of the gyroradius, the Taylor expansion of the magnetic field vector about the guiding centre of the particle can be written:

$$\mathbf{B} = \mathbf{B}_o + (\mathbf{r} \cdot \nabla) \mathbf{B}_o \quad (1.17)$$

Combining this with equation 1.8 gives:

$$m \frac{d\mathbf{v}}{dt} = q(\mathbf{v} \times \mathbf{B}_o) + q(\mathbf{v} \times (\mathbf{r} \cdot \nabla) \mathbf{B}_o) \quad (1.18)$$

The velocity term includes both gyromotion and drift motion $\mathbf{v} = \mathbf{v}_g + \mathbf{v}_\nabla$. As $\mathbf{v}_g \gg \mathbf{v}_\nabla$, the above equation becomes:

$$m \frac{d\mathbf{v}_\nabla}{dt} = q(\mathbf{v}_\nabla \times \mathbf{B}_o) + q[\mathbf{v}_g \times (\mathbf{r} \cdot \nabla) \mathbf{B}_o] \quad (1.19)$$

For periods longer than a gyration, it is useful to average over one gyration. This causes the first term on the right to disappear as any acceleration experienced by the particle as it moves to the weaker magnetic field is cancelled out by its subsequent deceleration during its movement into the

stronger field. Taking the cross product of equation 1.8 with \mathbf{B}_0/B_0^2 and combining it with equation 1.16 and 1.19 results in:

$$\mathbf{v}_\nabla = -\frac{1}{B_0^2} \langle [\mathbf{v}_g \times (\mathbf{r} \cdot \nabla) \mathbf{B}_0] \times \mathbf{B}_0 \rangle \quad (1.20)$$

where the angle brackets indicate an average over a gyroperiod. Assuming \mathbf{B} is aligned with the z-direction and varies only in x, $\mathbf{B}_0 = B_0(x)\hat{\mathbf{z}}$, the above equation becomes:

$$v_\nabla = -\frac{1}{B_0} \langle v_g x \frac{dB_0}{dx} \rangle \quad (1.21)$$

Replacing v_g and x with equations 1.11 and 1.12 results in:

$$v_{\nabla x} = -\frac{v_\perp r_g}{B_0} \langle \sin \omega_g t \cos \omega_g t \frac{dB_0}{dx} \rangle \quad (1.22)$$

$$v_{\nabla y} = -\frac{v_\perp r_g}{B_0} \langle \sin^2 \omega_g t \frac{dB_0}{dx} \rangle \quad (1.23)$$

By taking the gyroperiod average of the above, $v_{\nabla x}$ will disappear as it has the product of a sin and cos term. For the $v_{\nabla y}$ term, averaging over the \sin^2 term will result in a factor of $1/2$ and hence the drift velocity will only have a y component.

$$\mathbf{v}_\nabla = \pm \frac{v_\perp r_g}{2B_0} \langle \frac{\partial B_0}{\partial x} \rangle \hat{\mathbf{y}} \quad (1.24)$$

For a magnetic gradient in a general direction, the drift velocity equation is:

$$\mathbf{v}_\nabla = \frac{mv_\perp^2}{2qB^3} (\mathbf{B} \times \nabla B) \quad (1.25)$$

This shows that a magnetic gradient leads to a drift perpendicular to both the magnetic field and gradient. The drift velocity is dependent on q and hence the direction of the drift is charge dependent.

1.1.2.4 Generalised drift

Equation 1.16 shows the electric drift velocity. The equation can be adapted to give a generalised drift velocity for any particle in a magnetic field which also experiences a force. Replacing \mathbf{E} in equation 1.16 with $\mathbf{F} = q\mathbf{E}$, returns:

$$\mathbf{v}_d = \frac{\mathbf{F} \times \mathbf{B}}{qB^2} \quad (1.26)$$

This shows that forces which do not depend on charge will lead to a charge dependent drift.

1.1.2.5 Curvature drift

A drift also occurs when the magnetic field is curved. In this situation, particles with a parallel velocity, v_{\parallel} experience a centrifugal force:

$$\mathbf{F}_R = mv_{\parallel}^2 \frac{\mathbf{R}_c}{R_c^2} \quad (1.27)$$

where R_c is the radius of curvature of the field lines. By substituting the above equation into the generalised drift velocity equation (equation 1.26), the curvature drift velocity is obtained:

$$\mathbf{v}_R = \frac{mv_{\parallel}^2}{q} \frac{\mathbf{R}_c \times \mathbf{B}}{R_c^2 B^2} \quad (1.28)$$

In a cylindrical symmetrical magnetic field $-\nabla B = \frac{B}{R_c} \mathbf{R}_c$, thus the total drift resulting from both gradient and curvature drift is:

$$\mathbf{v}_B = \mathbf{v}_R + \mathbf{v}_{\nabla} = \left(v_{\parallel}^2 + \frac{1}{2} v_{\perp}^2 \right) \frac{\mathbf{B} \times \nabla B}{\omega_g B^2} \quad (1.29)$$

1.1.2.6 Magnetic mirroring

A particle's magnetic moment, μ , is defined as the ratio of its kinetic energy and the magnetic field strength:

$$\mu = \frac{mv_{\perp}^2}{2B} = \frac{mv^2 \sin^2 \alpha}{2B} \quad (1.30)$$

where v_{\perp} is replaced with $v \sin \alpha$ using the pitch angle defined in equation 1.13. The magnetic moment is an adiabatic invariant of the particle motion; that is, it remains constant if the electromagnetic field doesn't vary rapidly over the time scale of a particle gyroperiod or the length scale of a particle gyroradius. If no electric field is present, the energy of the particle is a constant of its motion. As the magnetic moment is also constant then a particle moving into a region of greater magnetic field strength will experience a change in pitch angle. Thus the magnetic field strength is related to a particle's pitch angle, the relationship between the two is:

$$\frac{\sin^2 \alpha_2}{\sin^2 \alpha_1} = \frac{B_2}{B_1} \quad (1.31)$$

Thus if a particle's pitch angle is known and the magnetic field strength at a particular location, it is possible to calculate the particle's pitch angle at any other location on the particle trajectory using the magnetic field strength at that location. If a particle moves into a region of converging magnetic field topology, i.e. into a region of greater magnetic field strength, its pitch angle will increase, this will cause it to gyrate faster perpendicular to the field line and move slower parallel to it. As the energy of the particle is constant, its energy perpendicular to the field will increase and its energy parallel to the field will decrease. At the point where the pitch angle increases to 90° , the particle is no longer moving parallel to the field; this

location is called the mirror point. The particle is then pushed back by the parallel component of the force that causes gradient drift. When a particle arrives at its mirror point, it will be reflected, this is referred to as magnetic mirroring.

1.1.3 Kinetic Theory

Another way of describing the behaviour of a plasma is to use kinetic theory which involves tracking the characteristics of the plasma as a whole rather than the individual particles. In this regime, particles occupy a volume in the six dimensional space, known as phase space, which is made up of the three dimensions of position and velocity (six dimensions in total). A plasma distribution can be described by the phase space density or distribution function $f(\mathbf{v}, \mathbf{x}, t)$; values of the macroscopic properties of the system (e. g. density, bulk velocity, pressure) at a given location in position space can be found by taking moments of the distribution, or integrating over the velocity space contributions (e.g. Paschmann et al., 2000). Calculating the i -th moment requires calculating:

$$M_i(\mathbf{x}, t) = \int f(\mathbf{v})v^i d^3\mathbf{v} \quad (1.32)$$

The first, second and third moments can be found from the above equation using $i = 0, 1, 2$ and correspond to the density, bulk velocity and pressure respectively:

$$n = \int f(\mathbf{v})d^3\mathbf{v} \quad (1.33)$$

$$\mathbf{v}_b = \frac{1}{n} \int f(\mathbf{v})\mathbf{v}d^3\mathbf{v} \quad (1.34)$$

$$P = m \int f(\mathbf{v})(\mathbf{v} - \mathbf{v}_b)(\mathbf{v} - \mathbf{v}_b) d^3\mathbf{v} \quad (1.35)$$

1.1.4 MagnetoHydroDynamics (MHD)

Single particle physics is useful for analysing plasmas if the dynamics of only a small number of particles are required to understand the system. However, this method becomes complicated and/or time consuming for plasmas consisting of a large number of particles. In such cases, an alternate way of analysing the behaviour of plasmas consisting of a large number of particles is to use MagnetoHydroDynamics (MHD). This treats the plasma as a fluid in which the properties of the individual constituent particles are averaged out. It is thus valid for timescales longer than the gyroperiod (the inverse of the gyrofrequency) and length scales larger than the gyroradius. Assuming quasi-neutrality (which implies $n_i = n_e = n$), for a species s , the continuity equation is:

$$\frac{\partial n_s}{\partial t} + \nabla \cdot (n_s \mathbf{v}_s) = 0 \quad (1.36)$$

This represents a statement that the number of particles is conserved. The equation of motion for such an MHD plasma is:

$$n_s m_s \left(\frac{\partial \mathbf{v}_s}{\partial t} + (\mathbf{v}_s \cdot \nabla) \cdot \mathbf{v}_s \right) = -\nabla \cdot \mathbf{P}_s + n q_s (\mathbf{E} + \mathbf{v} \times \mathbf{B}) \quad (1.37)$$

where the right hand side consists of the forces of the pressure gradient, electric field and magnetic field respectively. An Ohm's law can be generated by subtracting the equations of motion (equation 1.37) of the ions from that of the electrons and including a simplified collisional term that leads to the resistivity η :

$$\mathbf{E} + \mathbf{v} \times \mathbf{B} = \eta \mathbf{j} + \frac{1}{nq_e} (\mathbf{j} \times \mathbf{B} - \nabla \cdot \mathbf{P}_e) + \frac{m_e}{nq_e^2} \frac{d\mathbf{j}}{dt} \quad (1.38)$$

where \mathbf{j} is the current density ($\mathbf{j} = nq\mathbf{v}$). For most space plasma applications, the electron pressure gradient $\nabla \cdot \mathbf{P}_e$ and the rate of change of current density $\frac{d\mathbf{j}}{dt}$ are generally small and hence vanish from the equation; if the hall term ($\mathbf{j} \times \mathbf{B}$) is neglected the equation becomes:

$$\mathbf{E} + \mathbf{v} \times \mathbf{B} = \eta \mathbf{j} \quad (1.39)$$

Introducing also Maxwell's equations:

$$\text{Ampère's law:} \quad \nabla \times \mathbf{B} = \mu_o \mathbf{j} + \frac{1}{c^2} \frac{\partial \mathbf{E}}{\partial t} \quad (1.40)$$

$$\text{Faraday's law:} \quad \nabla \times \mathbf{E} = -\frac{\partial \mathbf{B}}{\partial t} \quad (1.41)$$

$$\text{Gauss' Law for B:} \quad \nabla \cdot \mathbf{B} = 0 \quad (1.42)$$

$$\text{Gauss' Law for E:} \quad \nabla \cdot \mathbf{E} = \frac{\rho}{\epsilon_o} \quad (1.43)$$

Substituting Ampère's law into Ohm's law (equation 1.39), taking the curl of the equation and substituting in Faraday's law and the vector identity $\nabla \times (\nabla \times \mathbf{B}) = \nabla(\nabla \cdot \mathbf{B}) - \nabla^2 \mathbf{B}$ results in:

$$\frac{\partial \mathbf{B}}{\partial t} = \nabla \times (\mathbf{v} \times \mathbf{B}) + \frac{\eta}{\mu_o} \nabla^2 \mathbf{B} \quad (1.44)$$

This is the magnetic induction equation; it shows that the change in the magnetic field over time can be due to convection of the plasma (first term on the right) and/or due to the diffusion of the magnetic field through a plasma (second term on the right). In situations when the diffusion term is significant in the equation, the plasma is able to diffuse perpendicular to the magnetic field. If the convection term dominates, there can be no net

motion of the plasma perpendicular to the magnetic field; both move together in this direction and the magnetic field is said to be “frozen in” to the plasma. The ratio of the convection term and the diffusion term defines the Magnetic Reynolds Number, which is used as a measure of whether the movement of the particles is convection- or diffusion-dominated. This can be found using a dimensional analysis of the magnetic induction equation (equation 1.44):

$$\frac{B}{\tau} = \frac{vB}{L} + \frac{B}{\sigma\mu_0L^2} \quad (1.45)$$

where τ is the time period of magnetic variations, v is the velocity perpendicular to the field line, L is the length over which the field line varies and σ is the conductivity (which is the inverted resistivity, $\sigma = \frac{1}{\eta}$).

Using the above equation the magnetic Reynolds number, the ratio of the 2 terms on the RHS, is:

$$R_m = \frac{vB/L}{B/\sigma\mu_0L^2} = \frac{vB\sigma\mu_0L^2}{BL} = vL\sigma\mu_0 \quad (1.46)$$

Note that in many space plasmas applications in which the conductivity is high and/or the spatial scales are long, the Reynolds number is very high, and the frozen-in condition is a good approximation when considering the bulk motion of the plasma within a given magnetic field. This is also known as ‘ideal MHD’ since it is equivalent to the case of zero resistivity. In this case, Ohm’s law is simply:

$$\mathbf{E} + \mathbf{v} \times \mathbf{B} = 0 \quad (1.47)$$

1.1.4.1 Magnetic Forces and Plasma Beta

Charged particles within a plasma are subject to the Lorentz force, which is represented by $\mathbf{j} \times \mathbf{B}$ when no electric field is present; this is also known as the magnetic force density. This force can be mathematically separated into two components which are found by crossing Ampère's law (equation 1.40) with \mathbf{B} which can be rewritten as:

$$\mathbf{j} \times \mathbf{B} = \frac{1}{\mu_0} (\nabla \times \mathbf{B}) \times \mathbf{B} = -\frac{\nabla B^2}{2\mu_0} + \frac{(\mathbf{B} \cdot \nabla) \mathbf{B}}{\mu_0} \quad (1.48)$$

The first term on the right hand side is the force arising from the gradient of the magnetic pressure, $B^2/2\mu_0$, which acts perpendicular to the field direction. The second term is the magnetic tension force, which acts to straighten any curvature in the field. It is useful to compare the magnetic pressure to the plasma pressure to give an indication of which of the two dominates the dynamics of the system; the ratio of the two is the plasma beta:

$$\beta = \frac{nkT2\mu_0}{B^2} \quad (1.49)$$

A high beta ($\beta > 1$) indicates the plasma pressure is dominant and hence the movement of the magnetic field is dominated by the movement of the plasma. A low beta ($\beta < 1$) indicates the magnetic pressure dominates and hence the movement of the plasma is dominated by the movement of the magnetic field.

1.1.4.2 Magnetic Reconnection

Magnetic reconnection is a process in which the magnetic field lines are reconfigured, changing their magnetic topology. The process begins with two separate plasmas located in regions of space with anti-parallel magnetic field components. Due to Ampère's law, a current sheet (a plane of current) must exist between two plasmas of different magnetic orientation. The additional presence of a spatially-uniform electric field, which has a component in a direction perpendicular to the magnetic field, will cause the particles to $E \times B$ drift in a direction perpendicular to both E and B . As the field is frozen in to the plasma, the field also drifts with the plasma. Thus this may cause both the plasma and the field lines to move towards the current sheet, this movement is directed towards the current sheet on both sides of it due to the antiparallel magnetic fields on either side of the current sheet. For reconnection to occur a region must form where the frozen-in condition breaks down (due to the occurrence of small scale gradients or anomalous resistivity of some kind), this causes the field and plasma to move separately. This region is called the diffusion region and forms within the current sheet. The magnetic field lines reconfigure within this region as shown in Figure 1.

Magnetic tension causes the newly-formed highly-kinked field lines to retreat; once they have moved outside of the diffusion region, the frozen-in condition applies to these field lines once more. As the magnetic field lines retreat, any particles on the field line that subsequently interact with the field line kink are accelerated in the direction parallel to the field line. The location at which reconnection occurs is referred to as the X-line (or neutral line) and the field lines connected to the X-line at any point in time form

the boundary between reconnected and non-reconnected field regions. This boundary is referred to as the magnetic separatrix.

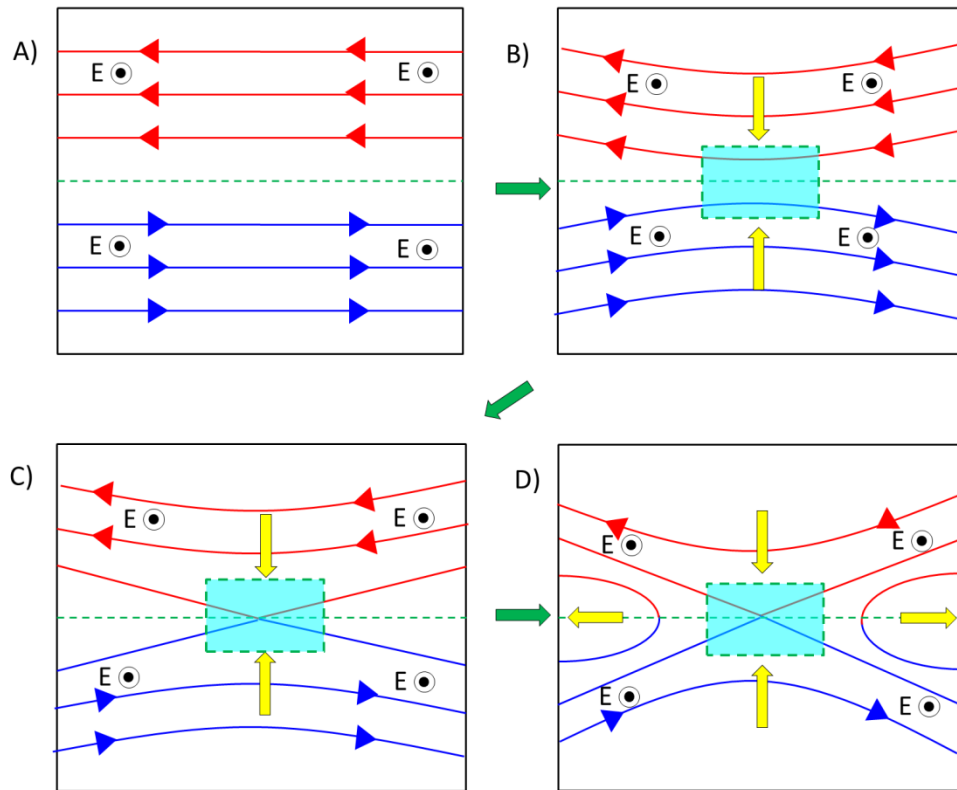


Figure 1: Diagram showing the action of the magnetic reconnection process. Panel A shows anti-parallel field lines separated by a current sheet (green dashed line). Panel B shows that the field lines $E \times B$ drift towards the current sheet and a diffusion region (a location where the frozen-in condition breaks down, turquoise square) forms. Panel C shows the field lines reconfigure within the diffusion region. Panel D shows the newly kinked field lines recoil away from the diffusion region.

The earliest steady state model of magnetic reconnection was the Sweet-Parker model (Parker, 1957). In this model the diffusion region is long (parallel to the current sheet) and thin (perpendicular to the current sheet) which is depicted in the left panel of Figure 2. The rate of reconnection,

R_{SP} , is defined as the ratio of the outflow velocity to the inflow velocity; its relationship to the Magnetic Reynolds Number is:

$$R_{SP} = \frac{1}{\sqrt{R_m}} \quad (1.50)$$

(Harra & Mason, 2004). In space plasmas R_M is high which, according to the above equation, will lead to a slow reconnection rate. The reconnection rate predicted by this model is so slow that it cannot account for the magnetospheric phenomena that are now known to result from magnetic reconnection.

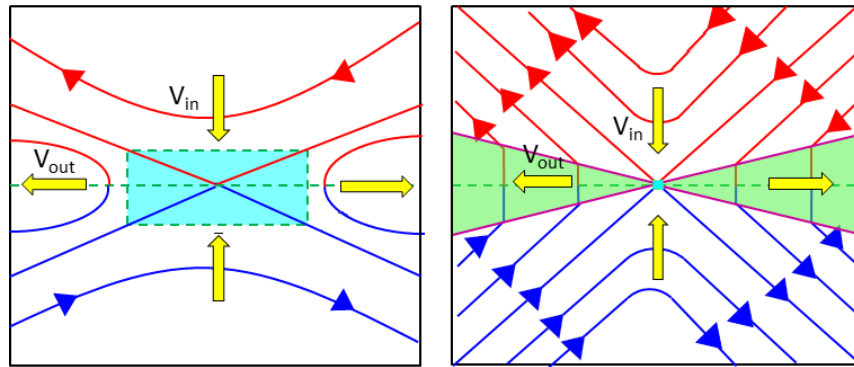


Figure 2: Diagram of the reconnection models. The yellow arrows indicate the inflow and outflow directions and the dashed green line at the centre is the current sheet. The left panel shows the Sweet-Parker model of reconnection. In this model the diffusion region is extended (parallel to the current sheet) and thin (perpendicular to the current sheet). The right panel shows the Petschek reconnection model. In this model, the diffusion region is small (turquoise square at the centre) and the plasma is accelerated at the shocks (purple lines) that bound the outflow region (green region).

A much greater reconnection rate can be obtained under the scenario known as the Petschek model of reconnection (Petschek, 1964) which is illustrated in the right panel of Figure 2. In this model, the diffusion region is much smaller; unlike the Sweet Parker model, not all of the plasma has

to pass through the diffusion region to be accelerated. Plasma is instead accelerated at the shocks that bound the outflow region (green region). The reconnection rate in this model is:

$$R_P = \frac{\pi}{8 \log R_M} \quad (1.51)$$

(Harra & Mason, 2004). The reconnection rate resulting from a given magnetic Reynolds number in this model is much greater than that of the Sweet Parker model and is more able to explain the magnetospheric phenomena caused by reconnection.

1.2 Magnetospheric Physics

1.2.1 Coordinate systems

Several coordinate systems are used for the study of the magnetosphere (see Hapgood (1992)). One is called the Geocentric Solar Ecliptic (GSE) system. In this coordinate system, X points from the Earth towards the Sun, Z is parallel to Earth's ecliptic north pole and Y is perpendicular to both and makes up the right hand set. The origin of the coordinate system is at the centre of the Earth. A second Earth-based coordinate system exists called the Geocentric Solar Magnetospheric (GSM) system. It shares the X-axis with GSE; the Z GSM axis is the projection of the Earth's magnetic dipole axis on the YZ GSE plane; Y GSM is perpendicular to X GSM and Z GSM and makes up the right hand set. The coordinate system used in this thesis is GSM.

1.2.2 Solar Wind

The solar wind is plasma expelled near-radially from the Sun; it consists mostly of protons and electrons with a small amount of alpha particles (Phillips et al., 1995). The magnetic field originating at the Sun is frozen into the solar wind which thus drags those field lines with it. At great distances away from the Sun this field is called the IMF (Interplanetary Magnetic Field). The IMF is frozen into the solar wind and has footpoints that trace back to the Sun. The movement of the solar wind away from the Sun, in combination with the rotation of the Sun (and hence the movement of the position of the footpoints) results in the field lines of the IMF being spiral shaped, this is known as the Parker spiral which is illustrated in Figure 3. The angle of the IMF in the ecliptic plane at the Earth is $\sim 45^\circ$. The solar wind can be categorized into two types, slow and fast, with velocities between $300 - 450 \text{ km s}^{-1}$ and $600 - 900 \text{ km s}^{-1}$ respectively (Phillips et al., 1995). At 1 AU the solar wind is supersonic (Parker, 1958) and has a magnetic field strength and plasma density of $\sim 6 \text{ nT}$ and $\sim 8 \text{ cm}^{-3}$ respectively (Neagu et al., 2005).

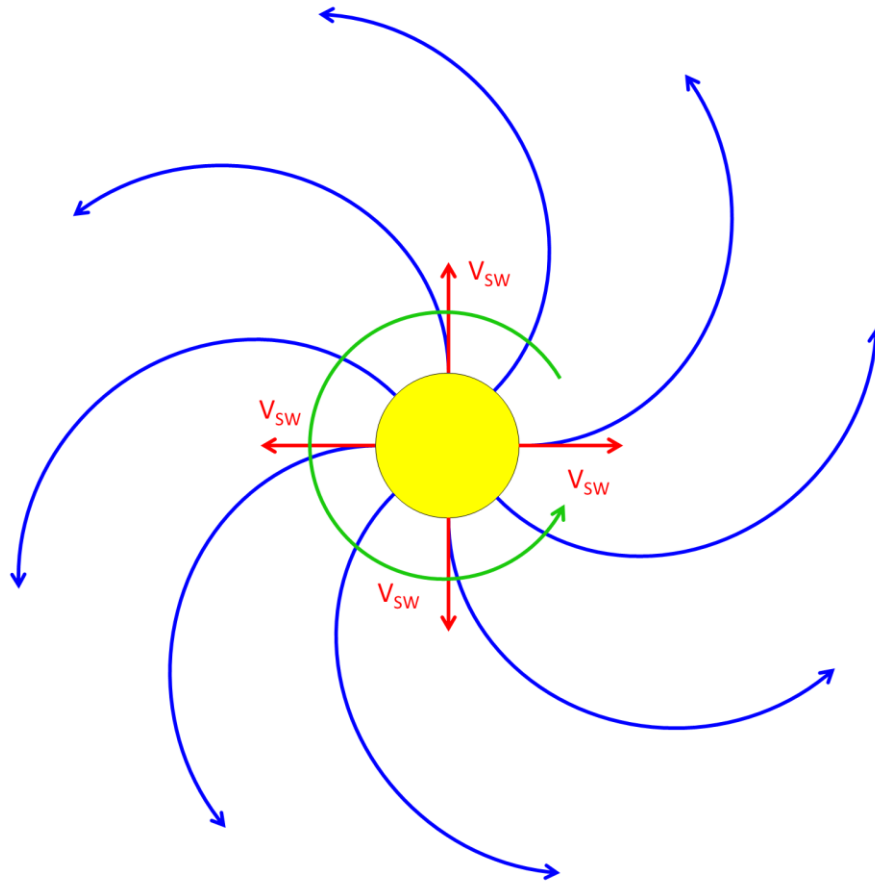


Figure 3: Parker spiral. The diagram shows a spinning Sun (in yellow with a green arrow showing the rotation), the Sun's magnetic field (the blue lines) and red arrows showing the direction of travel of the solar wind. The Sun's magnetic field is frozen into the solar wind and they move together; the footpoints of the Sun's magnetic field are on the surface of the Sun and move around the Sun as it rotates. The solar wind and the Sun's magnetic field are expelled radially; this, in combination with the spin of the Sun, results in field lines that are spiral shaped.

1.2.3 Magnetosphere

The magnetosphere is a cavity in the solar wind flow which confines, to a first approximation, the magnetic field of the Earth. The magnetosphere represents an obstacle to the solar wind, which is largely frozen out of the cavity. The magnetosphere also contains a number of plasma populations which are frozen into the magnetic field of terrestrial origin. The following

discusses some pertinent plasma regions arising in and around the magnetosphere and their properties.

1.2.3.1 Bow Shock and Magnetosheath

Since both the solar wind plasma and the plasma of the magnetosphere are frozen in to their respective magnetic fields, the two cannot mix and hence the magnetosphere presents an obstacle to the solar wind. The solar wind travels at supersonic, super-Alfvénic and super-magnetosonic speeds, thus faster than any pressure wave in the medium could, so any information about obstacles within the flow cannot be transmitted upstream fast enough to affect the plasma motion. In the case of the magnetosphere, a shock wave is formed upstream of the Earth (named the bow shock) which slows the solar wind to subsonic, sub-Alfvénic and sub-magnetosonic speeds; at these speeds a pressure wave is able to divert the solar wind around the magnetosphere. The region containing subsonic solar wind is known as the Magnetosheath. The slowing down of the solar wind converts kinetic energy to thermal energy which heats the plasma forming the magnetosheath. An additional effect of the slowing of the solar wind is an increase in plasma density; as mass flux is conserved, a reduction in velocity must be accompanied by an increase in plasma density. As the IMF is frozen into the plasma, the reduction in solar wind speed (and increase in plasma density) also leads to an increase in the magnetic field energy density and magnetic field strength. Hence the Magnetosheath has a greater plasma density and magnetic field strength than the interplanetary solar wind.

1.2.3.2 Shape and Surface of the Magnetosphere

Due to the frozen-in condition, the plasma of the solar wind and magnetosheath plasma cannot mix with the plasma of the magnetosphere. The pressure of the solar wind on the magnetosphere deforms the Earth's magnetic field from what would in a vacuum be approximately a dipole field, to the shape shown in Figure 4. The figure also shows the various plasma regions both inside and outside of the magnetosphere. From Figure 4, it can be seen that magnetosphere is compressed on the dayside and extended on the nightside. As the solar wind travels anti-sunward, it applies pressure to the magnetosphere along the Sun-Earth line, or X_{GSM} direction, hence the contraction and elongation of the magnetosphere are also along X. The magnetosphere is bounded by the magnetopause, which is the surface separating the magnetospheric plasma from the magnetosheath plasma. As the magnetic field is oriented in different directions either side of the magnetopause, Ampère's law implies a current must exist between the two, therefore the magnetopause surface is a current sheet. The regions above the magnetic poles, where the magnetosphere is funnel shaped, are called the polar cusps. The magnetic field strength at the cusps is low and the region is a point of entry for particles into the magnetosphere (Reiff et al.,1977).

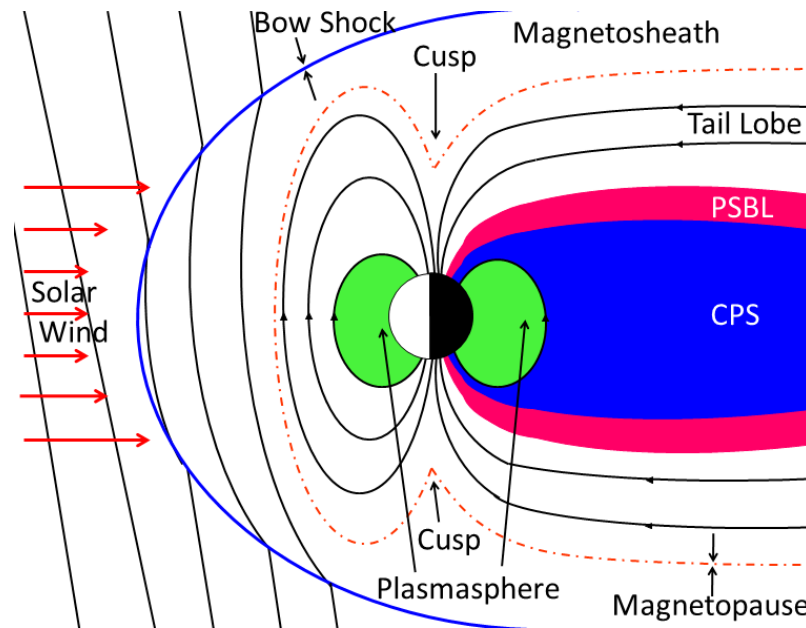


Figure 4: Diagram showing the magnetosphere. The solar wind is marked by the red arrows, magnetic field lines are marked by the black lines, the bow shock is the blue line, the magnetopause is the orange dashed line and the green region close to the Earth is the plasmasphere. The solar wind deforms the magnetosphere causing it to be compressed on the dayside and elongated on the nightside (the latter is called the magnetotail). Within the magnetotail is the plasma sheet which is made of two regions, the plasma sheet boundary layer (PSBL, pink region) and the central plasma sheet (CPS, blue region). Between the plasma sheet and the magnetopause is the tail lobe.

1.2.3.3 Inner Magnetosphere

The inner magnetosphere consists of several regions; the closest to the Earth is the ionosphere, which is created by the ionisation of the upper atmosphere. The ionosphere co-rotates with the Earth. At a greater distance from the Earth (at low and mid-latitudes) is a region called the plasmasphere, this region contains cool dense plasma (10^2 - 10^3 cm⁻³, 1 eV) originating from the ionosphere. The plasmasphere extends out to $\sim 4 R_E$ and, like the ionosphere, co-rotates with the Earth (e.g. Goldstein et al., 2003).

Between 2 - 6 R_E are the radiation belts (Van Allen et al., 1958), which consist of regions of energetic charged particles which are trapped along the dipolar field of the Earth. The belts are separated into the inner (1 - 3 R_E) and outer radiation belts (3 - 7 R_E), the former contains mainly protons and the latter, electrons (Van Allen et al., 1958, Ganushkina et al 2011). The inner radiation belt contains particles that originate from Earth's atmosphere that have been ionised by cosmic rays, it also contains energetic solar wind particles that accompany solar flares and coronal mass ejections. The outer radiation belt contains electrons from the plasma sheet that have been injected into the radiation belt during substorm dipolarisation events (Millian and Baker, 2012). The region between the two radiation belts is known as the slot region.

1.2.3.4 Magnetotail

As mentioned previously the dayside magnetosphere is compressed, but the opposite occurs on the nightside where the magnetosphere is able to expand into the wake in the solar wind flow; the elongated nightside region of the magnetosphere is called the magnetotail and is shown in Figure 4. The magnetotail has a magnetic gradient; the magnetic field strength is strongest at the poles and decreases tailward (Slavin et al., 1985).

The magnetotail is separated into three regions. The outermost region is the lobe, which is made up of open field lines which are connected at one end to the Earth and at the other end to the IMF. The lobe is separated into two halves, the northern and southern lobe, where the magnetic field is aligned close to the $+X_{GSM}$ and $-X_{GSM}$ directions respectively. In the lobe

(at $X_{\text{GSM}} \sim -50 R_{\text{E}}$) the magnetic field strength is ~ 15 nT and the plasma density is $\sim 0.01 \text{ cm}^{-3}$ (Zwickl et al., 1984; Slavin et al., 1985).

The centre-most region of the magnetotail, which is between the two lobes, is the plasma sheet. This region has a plasma density much greater than that of the lobe and the magnetic field strength is much less than the lobe. The region is made up of closed Earth field lines connected to the poles or (further downtail) IMF field lines. The magnetic field is oppositely directed in the northern and southern halves of the plasma sheet and hence (due to Ampère's law) a current exists in the plane between the two halves which is referred to as the current sheet. As the field is oppositely directed in the two halves, the magnetic field strength must drop to near zero at the centre of the current sheet, which occurs at a surface normally referred to as the neutral sheet. In the plasma sheet (at $X_{\text{GSM}} \sim -50 R_{\text{E}}$) the magnetic field strength is ~ 5 nT and the plasma density is $\sim 0.1 \text{ cm}^{-3}$ (Zwickl et al., 1984; Slavin et al., 1985).

The plasma sheet has a pressure gradient, the origin of which is explained as follows: After reconnection, the kinked field lines retreat towards the Earth due to magnetic tension. As they travel, they decrease in length and the plasma on the field line occupies less volume causing the density to increase, particles are also heated as the plasma is compressed. This results in a plasma pressure gradient where the innermost fields are the shortest field lines and hence have the greatest plasma density and temperature and hence pressure. This pressure gradient is present in X (the direction of the retreat of the field lines) and in Z (the most contracted field lines are at the lowest latitudes). As the pressure is constant perpendicular to the current

sheet and the plasma pressure increases towards the current sheet, the magnetic pressure decreases towards the current sheet.

The plasma sheet is subdivided into the central plasma sheet (CPS) and the plasma sheet boundary layer (PSBL, Eastman et al., 1984). The PSBL is the outer region of the plasma sheet and separates the lobe and the CPS. The PSBL is characterized by counter-streaming field aligned electrons. The CPS is defined as a region of ion $\beta > 0.3$, the lobe as a region of ion $\beta < 0.3$ and the PSBL as a region of ion $\beta < 0.3$ with field aligned electrons (Baumjohann et al., 1989). A similar statement can be made with the electron β ; in the plasma sheet the ion and electron densities are similar and the ion temperature is 7 times that of electron temperature (Baumjohann et al., 1988) hence according to equation 1.49 the electron β is a seventh of the ion β . Therefore the CPS is defined as a region of electron $\beta > 0.04$, the lobe as a region of electron $\beta < 0.04$ and the PSBL as a region of electron $\beta < 0.04$ with field aligned electrons.

1.2.3.5 Mantle

The lobe has a density and velocity gradient in the antisunward direction, which is associated with what is known as the plasma mantle. This is a layer of tailward travelling plasma of magnetosheath origin which is located inside the magnetosphere and is adjacent to the tail magnetopause (Rosenbauer et al., 1975). A diagram of the plasma mantle is shown in Figure 5 (taken from Pilipp and Morfill, 1978).

Particles may enter the magnetosphere via the dayside polar cusps along newly reconnected field lines. Subsequently, the particles move from the polar cusp and/or magnetopause into the nightside tail lobe regions under the influence of the convection electric field, the magnitude of which generally depends on the orientation of the IMF. In addition, particles flowing along the field lines of the cusp towards the Earth are mirrored resulting in a tailward velocity (Rosenbauer et al., 1975; Sckopke et al., 1976). Plasma may also enter by penetrating across magnetically open regions of the magnetopause along much of the length of the tail (Gosling et al., 1984).

As mentioned previously, the mantle particles are subject to the convection electric field; this gives the particles an $E \times B$ drift towards the current sheet. The combination of this with the tailward velocity of the particles results in the curved trajectories shown in Figure 5. Thus the mantle plasma fills the lobe at large downtail distance.

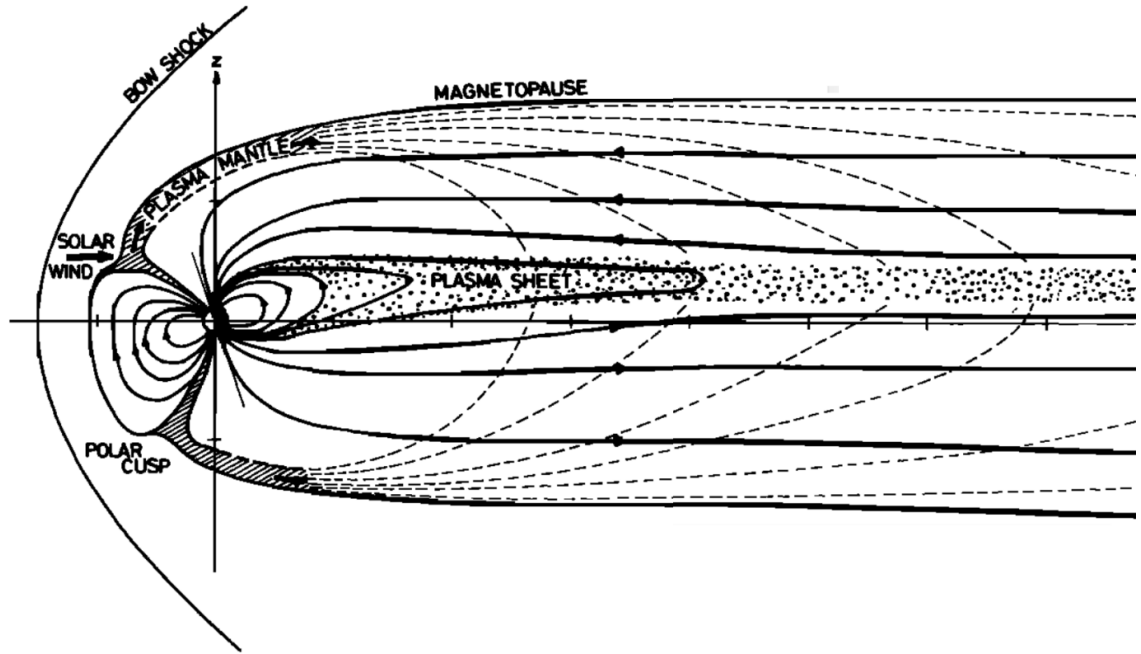


Figure 5: Diagram of the magnetosphere showing the layer of plasma just inside the magnetopause that is known as the plasma mantle. Further downtail the mantle increasingly fills the lobe with plasma of solar wind origin. The plot also shows the trajectory of the mantle particles (dashed lines) which is a combination of their tailward motion and the $E \times B$ drift of field lines to lower latitudes (taken from Pilipp and Morfill, 1978).

The filling of the mantle plasma into the lobe leads to a plasma density and velocity gradient in the lobe through the velocity filter effect (e.g., Shelley et al., 1976) which is explained with the aid of Figure 6. The diagram shows the northern tail lobe, three representative points of entry of magnetosheath particles into the magnetosphere (marked as the red, green and blue X's) and the trajectory of the particles entering at these points (coloured dotted lines). In the diagram, faster moving mantle particles will travel further downtail than slower particles (shown in the diagram as dotted lines) in the time it takes the associated field line to drift into the plasma sheet. In the diagram, at low Z values in the lobe, between the red and green entry points, only slow particles on the red trajectories are

detected as the faster ones travel further down tail before reaching the tail centre plane. Further downtail (between the green and blue entry points), slow particles on the green trajectories and mid-speed particles on the red trajectories are detected; thus compared to the previous region, the density and average velocity is greater. Tailward of the blue entry point, fast particles on the red trajectories, mid-speed particles on the green trajectories and slow particles on the blue trajectories are detected. This final region thus contains particles from entry points all 3 entry points and has slow, mid-speed and fast particles; hence this region has the highest density and average velocity compared to the others. Therefore, with increasing tailward distance, the density and average velocity of plasma in the tail lobes increases and hence the tail has a density and velocity gradient.

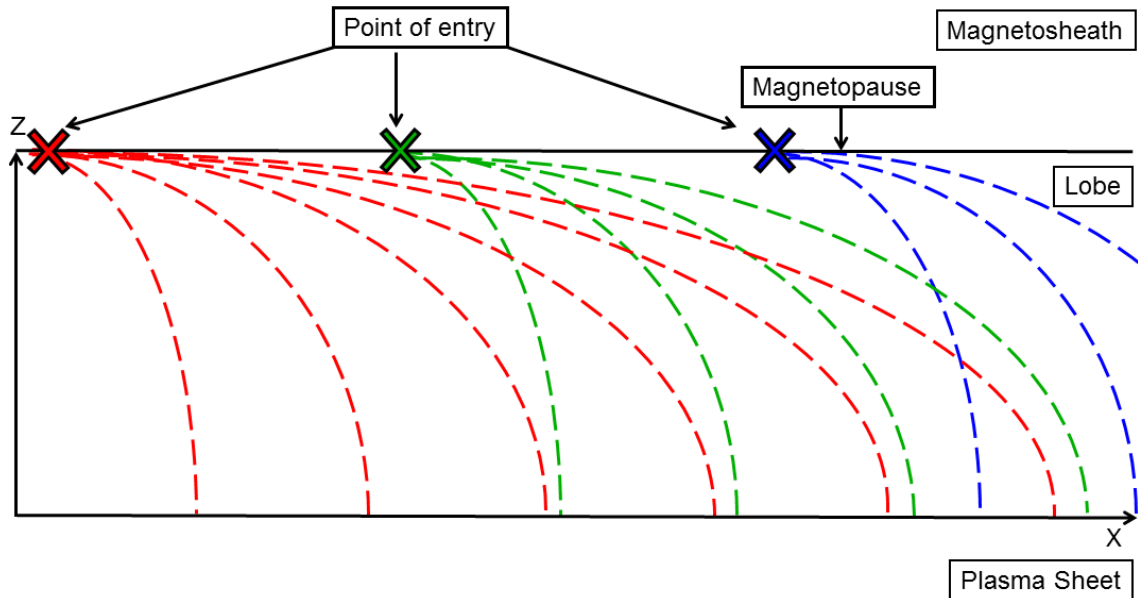


Figure 6: Diagram of velocity filter effect in the northern tail lobe showing how it leads to a density and average velocity gradient. The diagram shows three representative points of entry of particles into the magnetosphere (the red, green and blue X's) and the trajectory of said particles (the dotted lines). Faster moving particles travel further downtail before they arrive at the plasma sheet. At low Z values in the northern lobe, between the red and green entry points are slow particles on the red trajectories; between the green and blue entry points are mid-speed particles on the red trajectories and slow particles on the green trajectories; between the green and blue entry points are fast particles on the red trajectories, mid speed particles on the green trajectories and slow particles on the blue trajectories. Hence the density and average velocity of plasma within the tail lobe increases with downtail distance.

1.2.4 Dungey Cycle

As mentioned previously, the situation in which two frozen-in plasmas with oppositely directed field lines are separated by a thin current sheet can lead to the occurrence of magnetic reconnection. This can occur between the shocked IMF field in the magnetosheath and the magnetospheric field. It may also occur between the oppositely directed fields within the two halves of the tail. Reconnection at these two locations leads to a transport of magnetic flux and associated plasma around the magnetosphere in a cycle

known as the Dungey cycle (Dungey, 1961). This is illustrated in Figure 7 (the following bracketed numbers refer to the individual field lines shown in the diagram).

Initially (1) an IMF field line approaches the magnetosphere; if the fields are near anti-parallel, reconnection occurs (2) near the nose of the magnetosphere. This is referred to as dayside reconnection, which results in a field line (3) with one end on the Earth (as part of the magnetosphere) and the other end in the solar wind (as part of the IMF). As the solar wind continues to move anti-sunward, it carries the newly reconnected field line tailward. Once on the night side of the magnetosphere, the field lines are added to the magnetotail. These field lines sink into the lobes and are the north and south lobe fluxes and are oppositely directed to each other (4). This may lead to reconnection in this nightside region of the tail at an X-line which is typically located $-100 > X_{\text{GSM}} > -140 R_E$ downtail (Slavin et al., 1985). This X-line is often called the Distant Neutral Line (DNL).

Nightside reconnection converts field lines with one end in the IMF and one at the Earth into two separate field lines: one IMF field line with both ends in the solar wind and one magnetosphere field line with both ends on the Earth (5); the field lines are now of the same topology as they had prior to dayside reconnection. The IMF field lines have successfully traversed the obstacle of the magnetosphere and continue anti-sunward. After nightside reconnection, the newly reconnected closed magnetosphere field lines are highly kinked and due to magnetic tension and they travel Earthward (6). They then convect towards the dayside (7) ready to begin the process again.

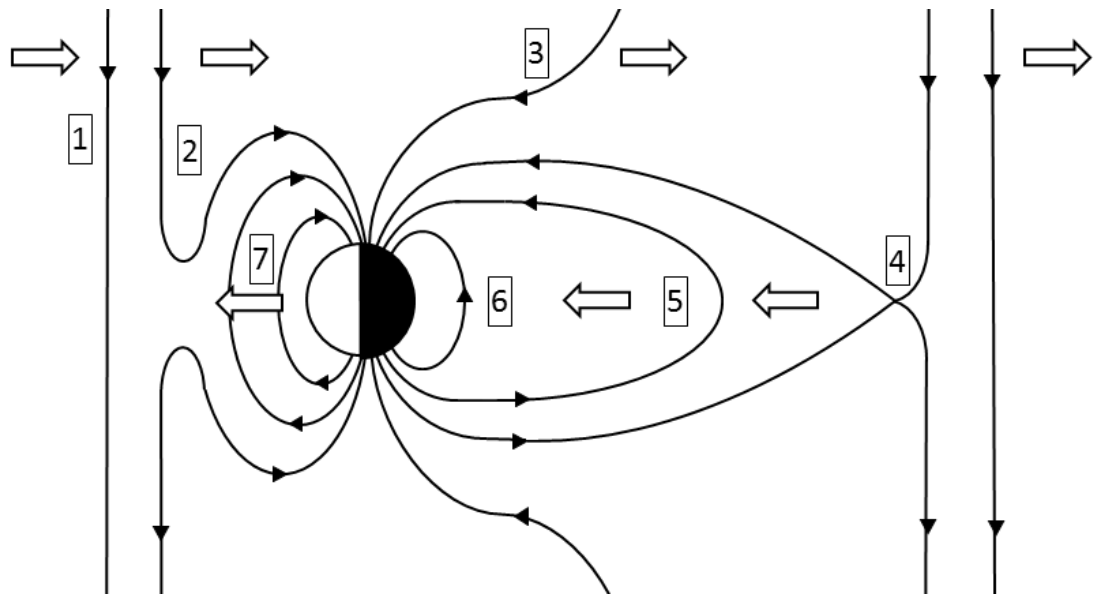


Figure 7: The Dungey Cycle. The diagram shows the interaction of the IMF field lines with the magnetosphere. 1) An IMF field line approaches the dayside of the magnetosphere. 2) Reconnection occurs between the IMF and magnetosphere if the fields are near anti-parallel. 3) The resulting field lines have one end on the Earth (as part of the magnetosphere) and the other end in the solar wind (as part of the IMF). The field lines are dragged anti-sunward by the solar wind and are added to the magnetotail. 4) The field line above the current sheet is anti-parallel to the field line below the current sheet and nightside reconnection occurs. This reverts the field lines to an IMF field line and a magnetosphere field line topology. 5 & 6) Magnetic tension causes the kinked magnetospheric field line to contract Earthwards. 7) The magnetosphere field line travels back to the dayside to begin the process again.

The field lines reconnected at the dayside (with one leg in the solar wind and one in the magnetosphere) are called ‘open’ field lines and hence particles can travel along these field lines allowing solar wind particles to enter the magnetosphere and magnetospheric plasma to escape into interplanetary space. These field lines fill the lobe region and for this reason have a low plasma density. The set of field lines created by nightside reconnection which have both ends connected to the magnetosphere are called ‘closed’ field lines. After reconnection, these field lines are highly kinked and under the influence of magnetic tension they travel Earthwards. The field lines are closed and the frozen-in

condition holds, such that particles cannot escape the field lines. The Earthward movement decreases their length which leads to an increase in plasma density; these field lines form the plasma sheet which has a high plasma density (relative to the lobe).

In the above example, the IMF has a negative B_Z and the field is anti-parallel to the field at the nose of the magnetosphere. At times when the IMF has a positive B_Z component, the field at the nose of the magnetosphere is not anti-parallel to the IMF and reconnection is much less likely to occur there. However, under these circumstances, the IMF is anti-parallel to the terrestrial field on the other parts of the magnetopause, such as poleward of the cusp regions and reconnection may then occur there instead.

1.2.5 **NENL model of Substorms**

A substorm is a process that occurs when there is an imbalance in the reconnection rates at the dayside and nightside; one model of the effect of this on the magnetosphere is the Near Earth Neutral Line model (e.g. Baker et al., 1996) which is explained with the aid of Figure 8.

The process is divided into three phases (McPherron, 1970): When the reconnection rate on the dayside is greater than at the nightside, there is an increase in the net amount of flux transported to the magnetotail. This is the growth phase of a substorm. When the amount of flux of the magnetotail reaches a threshold value, reconnection occurs at a new location in the tail called the near Earth Neutral Line (NENL) which is typically at $-20 > X_{GSM} > -30 R_E$ downtail (Nagai et al., 1997). This is the

beginning of expansion phase. Between the two reconnection sites (the DNL and NENL) magnetic field lines are closed leading to a set of concentric loops, together with the frozen-in plasma of the field lines. This is called a plasmoid.

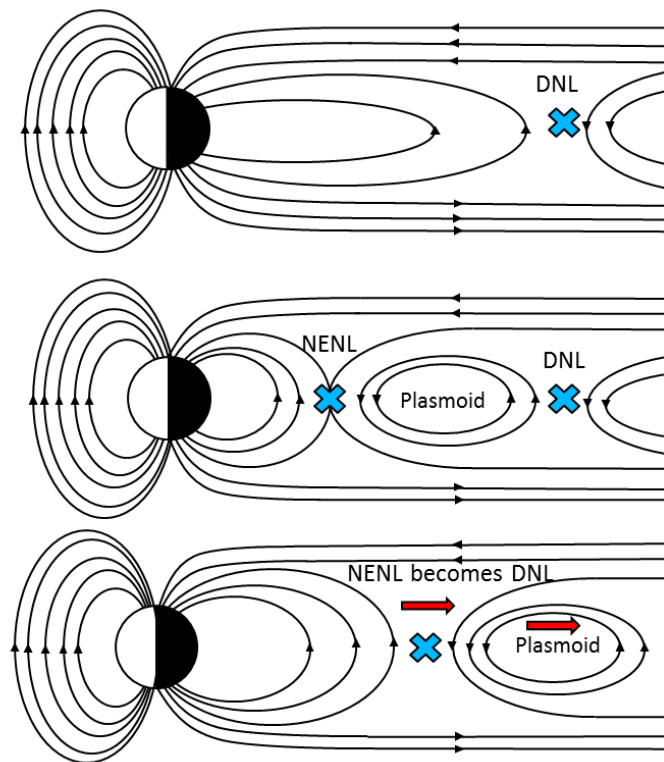


Figure 8: Picture of the magnetotail during the three phases of the NENL substorm model. The top panel shows the growth phase, the middle panel shows the expansion phase and the bottom panel shows the recovery phase.

If the reconnection rate of the NENL is greater than that at the DNL, then the plasmoid will be surrounded by flux that is open on the tailward side. The magnetic tension associated with these field lines will force the plasmoid downtail. Due to the subsequent decrease in pressure tailward of the NENL (caused by the removal of the plasmoid) and the increase in pressure Earthward of the NENL (caused by the addition of newly reconnected flux), the NENL may move downtail and become the new

DNL. This occurs during the recovery phase. The magnetosphere has then returned to the state it was in before the substorm and the cycle may happen again.

1.2.6 **Travelling Compression Regions**

Before reconnection commences, the steady state tail is in vertical pressure balance (i.e. in the direction normal to the current sheet). If a magnetic structure created by reconnection (e.g. a plasmoid) has a greater total pressure than that of the plasma sheet before reconnection, then the pressure of the magnetic structure is not balanced by the (smaller) pressure of the lobe. Assuming the magnetopause is a rigid boundary (Slavin et al., 1994), restoring pressure balance requires the expansion of the magnetic structure to reduce its pressure while also causing a compression of the lobe, thus increasing its magnetic pressure until global pressure balanced is restored. As the frozen-in condition is in effect, the expansion of the magnetic structure causes the magnetic field outside of the structure to drape around it.

The movement of this region of compressed lobe (caused by the movement of the magnetic structure below it) is called a Travelling Compression Region (TCR) (Slavin et al., 1992, 2003c, 2005; Owen et al., 2005). The compression of the lobe, in the direction perpendicular to the current sheet results in a peak in the magnetic field magnitude (and hence B_X as the tail field is directed mostly in X) and a bipolar signature in the magnetic component directed normal to the current sheet (nominally in Z) to be detected by a suitably positioned spacecraft as the magnetic structure passes (e.g., Slavin et al., 2003c).

TCRs have been observed travelling both Earthwards and tailwards; the direction of travel can be deduced from the sense of the bipolar signature, as shown in Figure 9. A bipolar signature consisting of a negative excursion followed by a positive excursion in B_Z has been shown to be Earthward travelling (Slavin et al., 2005); conversely, bipolar signatures consisting of a positive excursion followed by a negative excursion are tailward travelling.

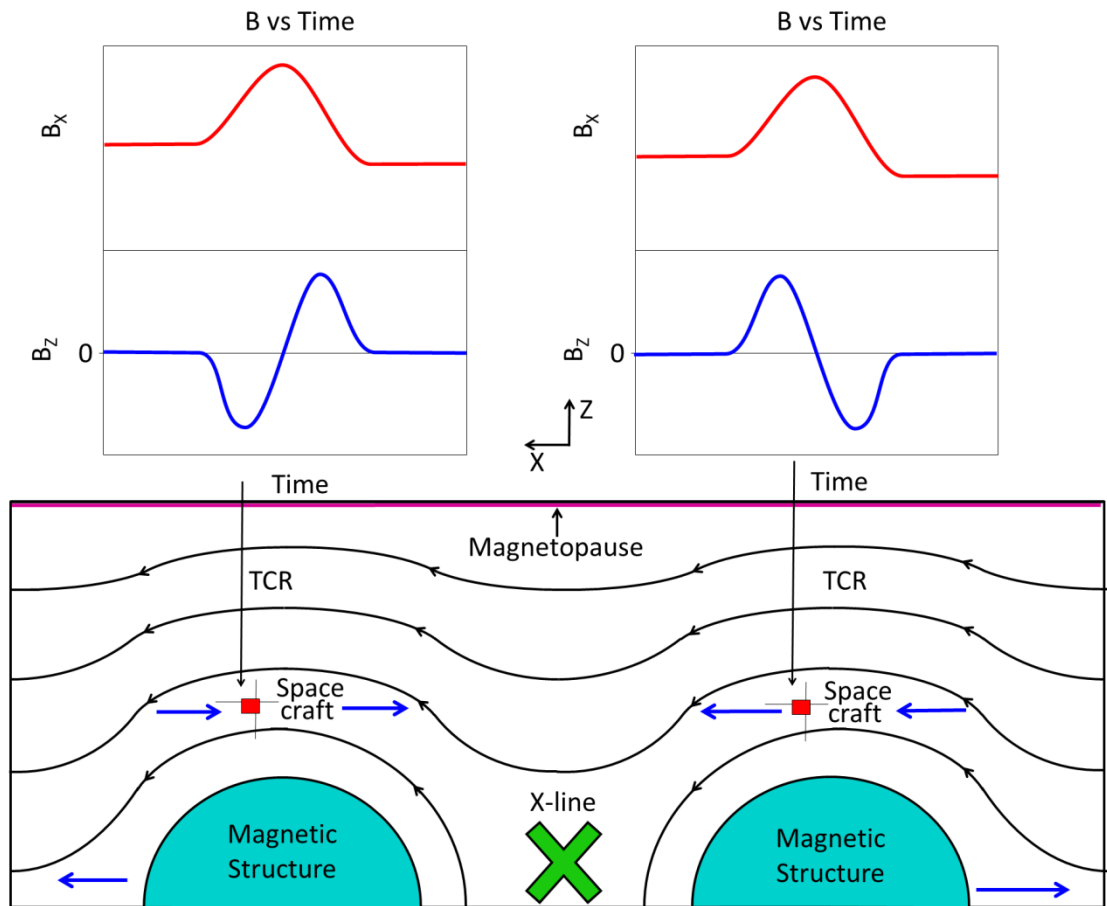


Figure 9: Diagram showing the magnetic signature of a TCR. The diagram shows a magnetic structure (turquoise) moving Earthward and tailward (left and right respectively) away from the X-line and the B_x (top panel, red trace) B_z (middle panel, blue trace) vs. time signature. The magnetic structure compresses the lobe field causing a TCR. Spacecraft (red square) are shown above the magnetic structures. The blue arrows show the motion of the spacecraft relative to the magnetic structure (although in absolute terms the spacecraft is stationary and the magnetic structure is moving). The diagram shows Earthward moving magnetic structures cause South-North bipolar signatures and tailward moving structures cause North-South bipolar signatures in B_z ; in both cases, B_x peaks.

1.3 Modes of Reconnection

1.3.1 Multiple X-line Reconnection (MXR)

The original model for magnetic structures formed by multiple reconnection sites was proposed by Lee and Fu (1985) in the context of the dayside magnetopause and assumes that reconnection occurs at two (or more) adjacent reconnection sites (hereafter referred to as X-lines). These will create a magnetic loop between them, nominally lying in the XZ GSM plane (in the case of magnetotail MXR). Hughes and Sibeck (1987) showed that, if there is a cross-tail magnetic field (originating from a B_Y component of the IMF), this mode of reconnection will create a helical magnetic structure, known as a flux rope (Elphic et al., 1986; Slavin et al., 2003a). One of the multiple X-lines within the tail will generally reconnect faster than the others (Schindler, 1974), and will thus begin to reconnect open lobe magnetic flux prior to other X lines. Lobe field lines reconnected at this 'dominant' X-line will subsequently envelope the set of flux ropes forming on either side. As illustrated in Figure 10, these hairpin-like field lines subsequently act to expel the plasma and the magnetic structures away from the dominant X-line (Schödel et al., 2001; Slavin et al., 2003a) along the current sheet; this occurs on either side of the X-line. All plasma, reconnected field lines and flux ropes located Earthward (tailward) of the dominant X line, travel in the Earthward (tailward) direction.

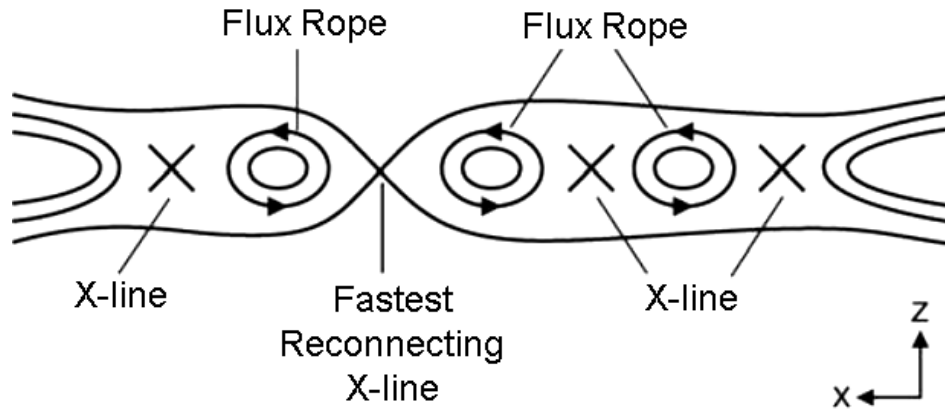


Figure 10: Diagram of the central region of the magnetotail showing multiple X-lines and the flux ropes that form between them. The newly reconfigured, kinked field lines that envelope the flux ropes act to expel them Earthward and tailward away from the fastest reconnecting X-line. Diagram adapted from Slavin et al. (2003a).

The simplest model of the structure of a magnetic flux rope is the force-free model (e.g. Lepping et al., 1990), which is the minimum energy configuration for helical magnetic fields. The model is force-free ($\mathbf{F} = \mathbf{J} \times \mathbf{B} = 0$) as the magnetic tension force acting radially inwards is balanced by the outward-directed magnetic pressure force, such that the structure will not evolve with time (Priest, 1990). Forces associated with the presence of plasma are ignored in this model. The current is parallel to \mathbf{B} everywhere, $\mathbf{J} = \alpha \mathbf{B}$, and ‘constant α ’ solutions for such structures are cylindrical, with the magnetic field largely azimuthal at the outer edge and becoming increasingly axial towards the centre, often resulting in a strong core field. The core field of plasma sheet flux ropes can be up to twice the intensity of the tail lobes (Slavin et al., 1995). The structure is invariant along the cylinder axis (hereafter referred to as the invariant axis), a diagram showing the helical force free flux rope is shown in Figure 11.

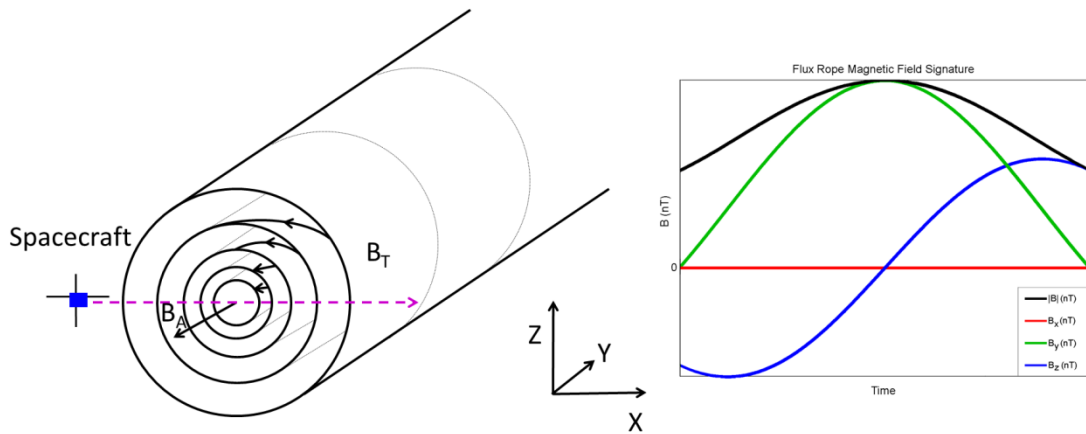


Figure 11: On the left is a diagram of a force free flux rope with an axis aligned with Y, travelling Earthward. The field of the flux rope is helical, it has a field which is tangential at the edge which becomes increasingly axial towards the centre. The field is greatest at the centre (represented by the close spacing of the field lines); diagram adapted from Henderson et al. (2006). On the right is the magnetic field signature obtained by a virtual spacecraft (the blue square in the diagram) travelling through the centre of the flux rope. The figure shows a plot of B_X (red), B_Y (green), B_Z (blue) and $|B|$ (black) vs. time. The B_X trace is constant and zero, the B_Y and $|B|$ traces peak and the B_Z trace shows a bipolar signature. The bipolar magnetic signature of the force free flux rope has excursions of similar magnitude and duration.

Figure 11 also shows the variation of the components of the magnetic field expected to be observed by a spacecraft passing through the centre of an idealised Earthward-travelling force-free flux rope. For a crossing through the centre of a flux rope, a spacecraft will detect a constant B_X of zero, a unipolar B_Y and $|B|$ signature and a bipolar B_Z signature. An off-centre crossing (i.e. a crossing with a non-zero impact parameter), is similar to the central crossing with the exception that B_X will also show a peak at closest approach. With increasing impact parameter, the magnitude and duration of the B_Y , B_Z and $|B|$ signatures will decrease. The bipolar B_Z signature will have a positive and negative excursion of similar magnitude.

Due to the compression in the lobe caused by the flux rope, a spacecraft in the lobe will detect a TCR (Slavin et al., 2003c). A spacecraft travelling through a flux-rope-generated TCR will detect a B_X and $|B|$ signature that peaks at closest approach, a B_Y signature that depends on the IMF induced B_Y in the tail lobe and a bipolar B_Z signature. The bipolar signature is expected to have excursions of similar magnitude and duration. During a TCR, the B_X component and $|B|$ will peak, before reducing to a level lower than the pre-encounter value. This is a result of reconnection driving a net loss of magnetic flux from the tail in association with the formation of the flux rope. Flux ropes have been directly observed and reported by a number of authors (e.g. Slavin et al., 1999; Walsh et al., 2007; Imber et al., 2011) and are 2-5 R_E in lateral extent (Slavin et al., 2003a).

Non-force-free magnetic structures have also been observed (e.g. Henderson et al., 2006) and more sophisticated models have been created to account for them (e.g. Mulligan and Russell, 2001). The implied imbalance of internal magnetic forces suggests such structures may be undergoing an evolution towards a force-free magnetic structure as this is the minimum energy configuration. Real flux ropes are expected to contain plasma; if a plasma gradient is present, this will contribute plasma pressure forces to the overall force balance. The presence of plasma in a flux rope will generally decrease the magnetic field strength below that of an ideal force free flux rope due to the diamagnetic effect. I am unaware of any studies of the characteristics of particle populations inside magnetotail flux ropes. Due to the concentricity of the field lines of a flux rope, the distribution of the plasma is expected to be spatially symmetrical about the axis, and thus also symmetric about the inflexion point of the bipolar

signature in observations from spacecraft passing through such structures. As the flux rope is formed in the central plasma sheet (CPS), it is expected to contain CPS-like plasma.

1.3.2 **MHD Model of Time Dependent Reconnection**

An MHD model of TDR has been developed (Semenov et al., 1983a, 1984; Biernat et al., 1987) based on Petscheck-type reconnection (Petscheck, 1964); this involves a pulse-like electric field occurring at a single X-line. During the pulse-like electric field, the ideal MHD approximation breaks down and magnetic flux reconfigures within the diffusion region; this disturbance of the system is transmitted through the plasma of the tail via shocks. Inflow particles are accelerated across the shocks; the shocks bound the outflow plasma in a teardrop-shaped region named the plasma outflow region (PO region). We refer to the structure comprised of the PO region and field lines as a flux bulge; the flux bulge and its associated magnetic signatures are shown in Figure 12 (adapted from Kiehas et al., 2009). The left and right upper panels show a flux bulge formed Earthward and tailward of the X-line respectively, this is also the direction in which they travel. The front and back ends of the flux bulge will be referred to as the leading and trailing ends.

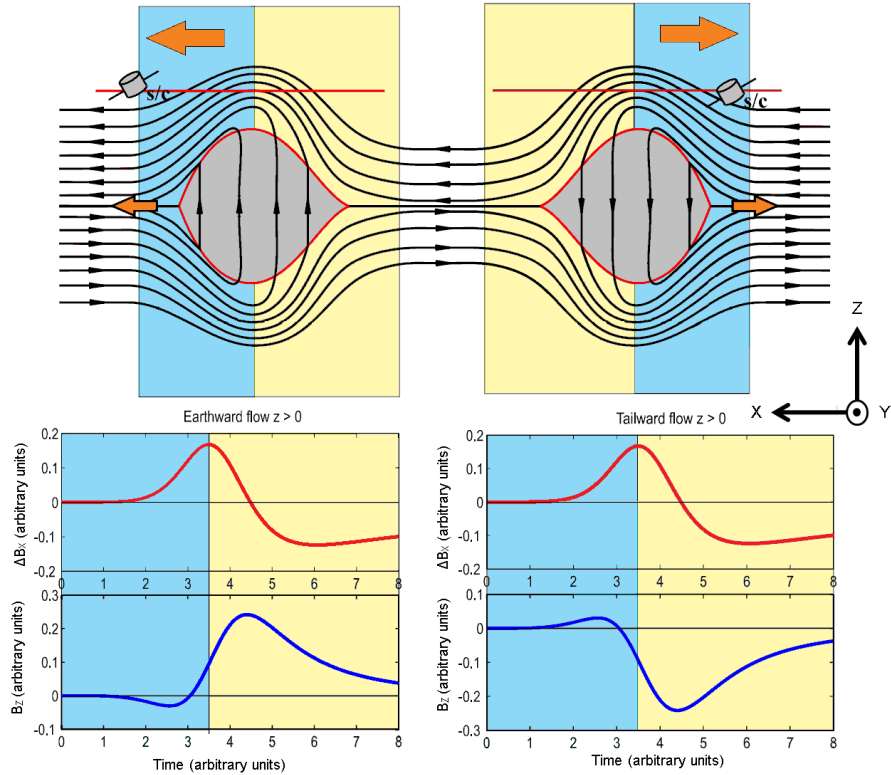


Figure 12: Diagram showing flux bulges (the product of the MHD model of TDR) and their associated magnetic field signature formed downstream of an X-line. The left and right upper panels show a diagram of two flux bulges, formed Earthward and tailward of the X-line respectively, their direction of travel is shown by the orange arrows. The magnetic field within the PO region (the grey shaded region) is aligned along Z. The bottom panels show the magnetic field signature of the associated TCR against time with ΔB_X in red and B_Z in blue as seen by a model spacecraft following the trajectories shown in the top panels. The yellow and blue areas in the diagram correspond to the yellow and blue areas in the magnetic plots. In this model the TCR bipolar signature in B_Z has a trailing excursion which is larger in magnitude and duration than the leading excursion. Figure from Kiehas et al. (2009).

After reconnection ceases, the shocks detach from the region where reconnection occurred and the flux bulges travel at the Alfvén velocity in opposite directions away from the X-line along the current sheet. As the shocks do not disappear when the electric field reduces to zero, the structure continues to grow in Z after reconnection ceases despite no additional flux being added to the structure (Kiehas et al., 2007). The PO

region of the structure is assumed to be a relatively thin boundary layer (thin in the direction perpendicular to the current sheet).

Before reconnection commences, all of the field lines are horizontal and thus the formation and growth of the PO region of limited extent causes the field lines to be displaced in the direction perpendicular to the current sheet, and hence gives rise to a TCR. The magnetic field outside of the PO region now drapes around it. The magnetic signature of the TCR in this MHD model of time-dependent reconnection is shown in the lower panels of Figure 12.

The panels show ΔB_X (red) and B_Z (blue) vs. time respectively of a virtual spacecraft crossing rapidly through the TCR (above the PO region). The B_X component peaks due to the compression of the lobe, the peak occurs in this component because the undisturbed lobe field is directed mostly in X. After the event, B_X reduces to a level lower than the initial value as the flux bulge causes a net removal of flux from the tail. The draped field lines outside of the PO region cause an asymmetric bipolar signature in B_Z . This has a trailing excursion which is both larger in magnitude and duration than the leading excursion in this model.

For trajectories lying closer to the current sheet, the spacecraft will encounter the heated PO region itself. Along these trajectories, whilst outside of the PO region, the spacecraft will detect part of the TCR signature. The negative excursion of the bipolar signature will be detected prior to entry into the PO region. Within the PO region (grey region in Figure 12), the spacecraft will detect no B_X and a peak in B_Z (Kiehas et al.,

2007). For a central crossing (a spacecraft travelling along the current sheet), the only signature detected is the peak in B_z . The heated plasma of the PO region reduces the magnetic field strength due to the diamagnetic effect (to below the lobe field strength). As the flux bulge is formed in the CPS, the PO region is expected to contain CPS-like plasma.

The expected change in the magnetic signature of the TCR of the flux bulge with distance from the current sheet and X-line was calculated by Kiehas et al. (2009) and are as follows. Figure 13 shows the change in the TCR magnetic signature expected in the lobe due to an Earthward moving flux bulge as a function of distance from the current sheet. The top panel shows ΔB_x and the bottom panel shows B_z at heights of $Z = 0.5, 0.75, 1.0$ (arbitrary units) in blue, green and red respectively. The plot shows with increasing distance from the current sheet, the signature decreases in magnitude. At the lowest value of Z , the positive and negative excursions of the B_z magnetic signature have different magnitudes relative to each other. With increasing Z , the relative difference between the two increases in B_z , conversely, the relative difference in the excursions of B_x decreases.

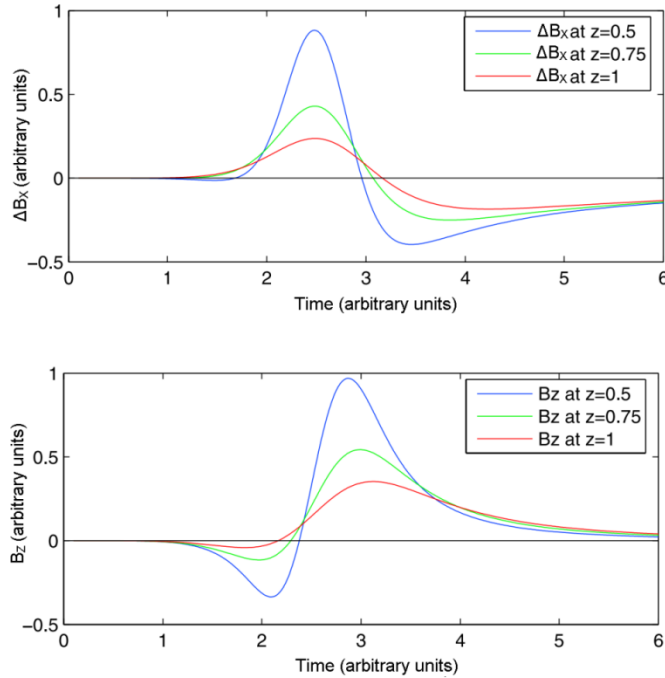


Figure 13: Diagram showing the variation in the TCR signature of an Earthward moving flux bulge as a function of distance from the current sheet; the top and bottom panels show the ΔB_x and B_z respectively. Each plot shows the magnetic signature at $X = 2$, at a height of $Z = 0.5, 0.75, 1.0$ (arbitrary units) in blue, green and red respectively. The plot shows with increasing distance from the current sheet, the signature decreases in magnitude. At the lowest value of Z , the positive and negative excursions of the B_z signature have different magnitudes relative to each other. With increasing Z , the relative difference between the two excursions increases in B_z but decreases in B_x . Figure from Kiehas et al. (2009).

Figure 14 shows the change in the TCR magnetic signature as a function of the distance the flux bulge has travelled from the X-line, which is equivalent also to the evolution of the flux bulge with time. The top and bottom panels shows ΔB_x and B_z for distances away from the X-line of $X = 1, 2, 3$ (arbitrary units) in blue, green and red respectively. With time, the PO region grows in Z leading to a magnetic signature of increasing magnitude in both B_x and B_z . At the earliest time, the positive and negative excursions of the B_z magnetic signatures have different

magnitudes relative to each other. With increasing time the relative difference between the excursions decreases for B_Z but increases for B_X .

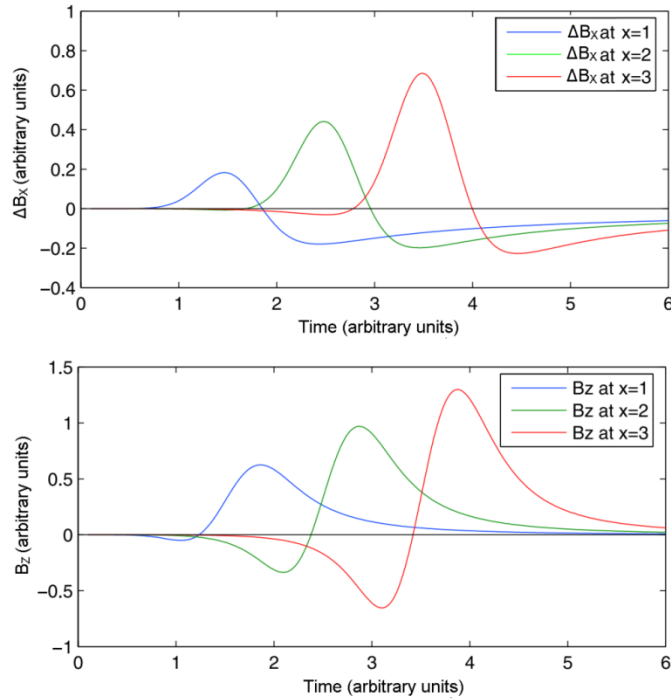


Figure 14: Diagram showing the change in the TCR signature of an Earthward moving flux bulge as a function of the distance the flux bulge travelled from the X-line, which is also the flux bulge evolution with time. The top and bottom panels show ΔB_X and B_Z respectively at $Z = 0.5$ for distances away from the X-line of $X = 1, 2, 3$ (arbitrary units). With time, the PO region grows in Z leading to a magnetic signature of increasing magnitude in both B_X and B_Z . At the earliest time, the positive and negative excursions of the B_Z signatures have different magnitudes relative to each other. With increasing time, the relative difference between the excursions decreases for B_Z but increases for B_X . Figure from Kiehas et al. (2009).

1.3.3 Cold Particle Model of Time Dependent

Reconnection

A second model for TDR was published by Owen & Cowley (1987a), from here onwards referred to as O&C87. This model considers the simplified situation of cold field-aligned particles and their interaction at the magnetotail current sheet with the hairpin-like field lines that are created by reconnection. In this model, the recoil speed of the reconnected field lines is controlled by both the velocity of the incoming particles and the balance between the magnetic stress of the field lines and the rate of change of momentum of the particles as they pass around, or are reflected from, the kink in the field. This means that the speed of recoil of the field lines from the X-line is independent of the reconnection rate at the X-line. In addition, the outflow particle speed depends on the same variables and is also independent of the reconnection rate.

In this model, an increase in reconnection rate leads to an increase in the amount of magnetic flux leaving the X-line, but it does not change the speed at which that flux retreats away from the X-line. Considerations of flux conservation imply that this extra flux must lead to a widening of the opening angle of the reconnected field wedge lying downstream of the X-line.

Conversely, a reduction of the reconnection rate leads to a thinning of this field wedge. Figure 15 (from O&C87) illustrates the effect of a step increase (middle panel) and decrease (bottom panel) in the reconnection rate in this model, which, in the case of the former, causes a bulge in the PO region (hatched region, defined as the region containing outflow

plasma). However, since this model considers only cold ($T = 0$ hence $P = nkT = 0$) inflow and outflow plasma populations, there is no outward displacement of reconnected field lines and no draping of external field lines around the structure. Thus the model does not naturally lead to the bipolar-type magnetic signatures nor indeed a compression observed in association with TCRs which are expected on both sides of the X-line. In this case B_z is unipolar and is positive Earthward of the X-line and negative tailward of the X-line. In addition, unlike the MHD model, the magnetic field direction within the PO region has both non-zero B_x and B_z components.

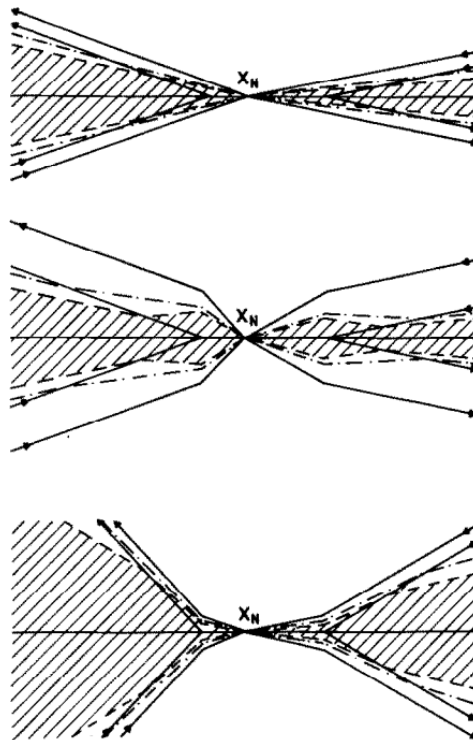


Figure 15: PO region (hatched region) and magnetic field lines resulting from the cold particle reconnection model. In the top panel, the reconnection rate is constant; in the middle panel, a step increase in the reconnection rate causes a thickening of the reconnection wedge, a bulge in the PO region close to the X-line (labelled X_N in the diagram) and a change in the angle of the field (solid arrowed lines). The bottom panel shows a step decrease in the reconnection rate and a thinning of both the reconnection wedge and the PO region and a change in the angle of the field. The field lines have both an X and Z component within the PO region and do not produce a TCR-like signature. Diagram from O&C87.

Chapter 2

Cluster Observations of a Transient

Signature in the Magnetotail:

Implications for the Mode of

Reconnection

2.1 Introduction

Travelling Compression Regions (TCRs) (Slavin et al., 1992, 2003c, 2005; Owen et al., 2005) are transient perturbations and compressions of the magnetotail lobe. The compression of the lobe in the direction perpendicular to the current sheet results in a peak in the magnetic field magnitude (and hence B_x GSM as the tail field is directed mostly in X GSM) and a bipolar signature in the magnetic component directed normal to the current sheet (nominally in Z GSM). Observations have shown that TCRs have a compression ratio ($\Delta B/B$) of $\sim 2-8\%$ (Slavin et al., 2005). TCRs have been observed travelling both Earthwards and tailwards; the direction of travel can be deduced from the sense of the bipolar signature. A bipolar signature consisting of a negative excursion followed by a

positive excursion in B_Z has been shown to be Earthward travelling (Slavin et al., 2003a); conversely, bipolar signatures consisting of a positive excursion followed by a negative excursion are tailward travelling.

Previous studies have suggested that TCRs are caused by magnetic structures created in the near-Earth magnetotail (Elphic et al., 1986; Moldwin and Hughes, 1994; Slavin et al., 2003a; Zong et al., 2004). Observations of Earthward travelling magnetic structures by Slavin et al. (2003a) identified 35 bipolar signatures, all of which were located between -10 and $-30 R_E$ (X_{GSM}). These structures are formed by reconnection (Elphic et al., 1986; Hughes and Sibeck, 1987) and are centred on the current sheet. However, it is still not clear whether these structures are a result of time-varying reconnection at a single reconnection site (e.g. Semenov et al., 1983a, 1984; Biernat et al., 1987) or reconnection occurring at multiple reconnection sites within the tail (e.g. Slavin et al., 2003a; Walsh et al., 2007).

This chapter examines a magnetic structure observed in the magnetotail by the Cluster spacecraft during a period when the relative position of the 4 spacecraft allowed the structure and its environs to be variously sampled. The observations are compared to the predictions of the signatures of the products of the two possible modes of reconnection to deduce which was most likely responsible for its formation. The structure of the chapter is as follows: Section 2.2 compares the expected observations resulting from the magnetic structure of the two modes of reconnection, Section 2.3 details the instruments providing data for this chapter, together with the orbit and configuration of the spacecraft, Section 2.4 presents the observations,

Section 2.5 is an analysis of the data, Section 2.6 provides an interpretation of the data and discusses the possible explanations and Section 2.7 notes the conclusions.

2.2 Comparison of the Reconnection Products

The following is a review of the differences between the signatures of the products of the two modes of magnetic reconnection occurring in the magnetotail; these will be used in an attempt to identify the mode of reconnection that created the magnetic structure. Note the term PO region refers to the region of plasma at the centre of either structure.

MXR creates flux ropes, magnetic structures comprised of helical magnetic field lines containing plasma. A spacecraft crossing through a flux rope will detect a peak in B_Y (the core field), a bipolar signature in B_Z with excursions of similar duration and magnitude and a plasma distribution which is symmetric about the centre of the bipolar signature. A central crossing will detect a constant $B_X \sim 0$ and an off centre crossing will detect a peak in B_X . The flux rope will cause a TCR; a spacecraft passing through this will detect a peak in B_X and a bipolar signature in B_Z (with excursions of similar duration and magnitude).

TDR creates flux bulges which have tear-drop shaped PO regions where the magnetic field is directed perpendicular to the current sheet. The flux bulge will cause a TCR; a spacecraft passing through this will detect a peak

in B_x and a bipolar signature in B_z with a leading excursion which is smaller in duration and magnitude than the trailing excursion. For crossings closer to the current sheet, the TCR signature will be detected outside of the PO region and a peak in B_z will be detected within it. The PO region is expected to be detected immediately after the negative excursion of the TCR bipolar signature. For a central crossing, the only signature detected is the peak in B_z in the PO region.

2.3 Instrumentation

The magnetic structure that is the subject of this chapter is observed by the Cluster spacecraft. Cluster is a mission of the European Space Agency (ESA) comprised of four spacecraft designed to study the Earth's magnetosphere (Escoubet et al., 2001). This mission has the advantage over single spacecraft missions of being able to distinguish between the change in intensity and the movement of a source of a field or parameter. Four spacecraft were chosen as this is the minimum number of spacecraft needed to make the above distinction in 3D.

The Cluster I satellites were launched in 1996, however the spacecraft were destroyed due to the launch failure of Ariane 501. The spacecraft were rebuilt (named Cluster II but referred to below simply as Cluster) and were launched in the year 2000. Cluster is in a polar orbit around the Earth, the spacecraft are in a near tetrahedral formation which is designed for studying three-dimensional plasma structures and for deriving vector quantities. Initially the spacecraft had an apogee and perigee of 19.6 and 4 R_E respectively, this allowed the spacecraft to sample the solar wind, bow

shock, magnetopause, the polar cusp and magnetotail. Over several years the apsides were rotated further below the ecliptic plane such that the spacecraft cross the ecliptic plane at a position much closer to the Earth. This allows the spacecraft to sample areas not reached by the initial orbit (the low latitude magnetopause, the near Earth plasma sheet, the auroral acceleration regions and the radiation belts). The spacecraft separation can be changed and ranges between 100 km and 18,000 km. As the Earth orbits the Sun, the magnetosphere moves relative to the plane of the orbit, allowing the spacecraft to sample different regions of the magnetosphere over the year. This chapter focuses on observations made in the magnetotail which Cluster passes through between July and October. Each spacecraft carries a payload of 11 instruments; this chapter makes use of three of these:

2.3.1 FGM

Data on the magnetic field vector at each spacecraft are collected by the Fluxgate Magnetometer (FGM) (Balogh et al., 2001), which is comprised of two tri-axial fluxgate magnetometers which are located on a boom. To reduce the effect of the spacecraft's magnetic field on the readings, the magnetometer furthest from the spacecraft (furthest down the boom) is designated the primary sensor. However either magnetometer can act as the primary sensor. The instrument provides 3-D magnetic field vectors at a frequency of up to 67 Hz; in this study, 5 Hz data is used.

2.3.2 PEACE

The electron moments and velocity distribution data were obtained from the Plasma Electron And Current Experiment (PEACE) instrument (Johnstone et al., 1997). PEACE measures the 3-D velocity distribution function of electrons in space plasma, for an energy range from ~ 0.6 eV to ~ 26.4 keV. During the observations, PEACE on all four spacecraft had a time resolution of 4 seconds. The PEACE instrument is a top hat analyser, a simplified schematic diagram of which is shown in Figure 16.

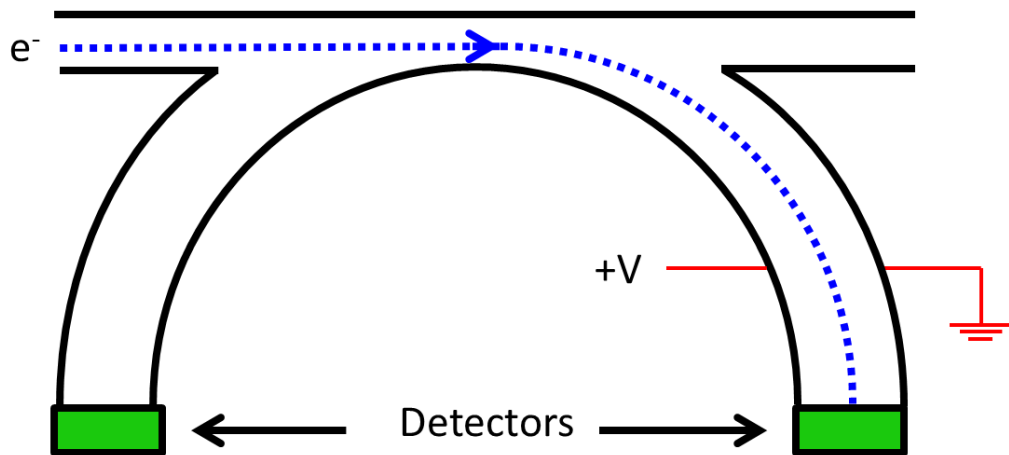


Figure 16: Diagram showing a top hat analyser. The path of an electron is the blue dotted line. The two semi-circles represent the two hemispheres. The voltage applied across the hemispheres causes the path of an electron to curve, electrons with a specific energy will have a path which takes them into the detector.

2.3.2.1 Top Hat Analyser

The top hat analyser consists of an inner hemisphere, an outer hemisphere and a top cap. Detectors are located at the bottom of the diagram, between the two hemispheres. The inner hemisphere is given a positive charge and the outer hemisphere is grounded. The charged plates will curve the

trajectory of electrons travelling between the plates. The voltage difference between the plates is set so only particles with a specific energy (and velocity) will have a path which leads them into the detector. Electrons below a certain energy (and speed) will be deflected too much and impact the positive inner plate. Electrons above a certain energy (and speed) will be deflected too little and impact the negative inner plate. The inner hemisphere voltage is set to select the energy of the electrons detected; to detect electrons of all energies, the voltage is set to detect the highest energy particles, the energy is then lowered and particles at the 2nd highest energy level are detected. The energy level is lowered continuously until the instrument has swept through all energy levels in the instruments energy range. Once completed, the energy level is raised to the highest value and the cycle begins again. The sensitivity is not great enough to detect single electrons. Thus to increase the number of electrons to a measurable amount, electrons are passed through micro-channel plates. These are glass plates with microscopic pores; electrons enter one of these pores which releases a secondary electron; both of these electrons enter other pores causing the release of even more electrons. The result of the chain reaction is an increase in the number of electrons to the point that they represent a detectable current.

2.3.2.2 Photoelectrons

A problem associated with electron analysers is contamination by photoelectrons. Ultraviolet radiation can cause photoelectrons to be released from the spacecraft through the photoelectric effect. This causes the spacecraft to become positively charged and have a positive potential. This

affects the readings in two ways: firstly the positive potential accelerates electrons entering the analyser, thus artificially increasing their energy; secondly, it causes an artificial increase in the electron count from the detection of photoelectrons (which do not have enough energy to escape the positive potential) and electrons whose initial path would not lead them into the detector but the positive potential curves their path which leads them into the detector. The spacecraft potential depends on the balance between the flux of photoelectrons being emitted by the spacecraft and the flux of electrons accelerated towards the spacecraft by the potential. In higher density regions, more electrons are available and more are attracted to the spacecraft, which reduces the spacecraft potential leading to a smaller artificial increase in electron count due to spacecraft potential. Hence the spacecraft potential is lowest in the higher density regions. The opposite is true in low density regions, hence contamination of PEACE data due to photoelectrons occurs to a greater extent in the low density regions. Cluster was built with a mechanism for reducing the spacecraft potential called the Active Spacecraft POtential Control system (ASPOC, Torkar et al., 2001), this releases positive ions at a rate set to reduce the spacecraft potential.

2.3.2.3 Data Products

PEACE can return several of data products, one is a 3D distribution. PEACE has a 180° field of view which is perpendicular to the spin plane, this, in combination with the spin of the spacecraft, results in 4π steradian coverage. A second data product can be found by combining PEACE data with the magnetic field direction (from FGM), which allows the onboard

determination of the pitch angle distribution of the electrons. The 180° field of view of PEACE is split into several angular bins. At any one time, a field line will not be directed both into and out of an angular bin of a PEACE sensor, which is required for a 180° pitch angle distribution. To obtain 180° coverage of a field line, each sensor takes measurements once when the field line is directed into one of the angular bins and once half a spin later when the sensor is on the other side of the spacecraft and the field line is directed out of one of the angular bins of the same sensor, hence pitch angle distributions can only be obtained once every spin.

PEACE can return a third data product by combining the velocity distribution obtained from the 3D distribution and the kinetic theory equations (1.33, 1.35, 1.34); this is referred to as taking moments of the velocity distribution. By taking the 0th, 1st and 2nd moment, PEACE can return the number density, bulk velocity and thermal pressure respectively.

2.3.2.4 Units

The raw data obtained by PEACE is the count rate, which is the number of particles detected per second (counts per second) in each energy-angle bin; this can be expressed in a more physical unit of measure called differential energy flux (DEF). Instead of representing the number of particles detected per second, DEF indicates the equivalent amount of energy entering the detector in a given interval of time, space, angle and energy (the latter states that only particles with a particular energy are counted). The unit used for differential energy flux is kiloelectron volts per centimetre squared, per second, per steradian, per kiloelectron volt, which

in symbol form is $\text{keV s}^{-1} \text{cm}^{-2} \text{sr}^{-1} \text{keV}^{-1}$, hence this is the same information as count rate, expressed as a different unit. This unit allows for a comparison between different instruments as it removes the dependence of count rate on the factors related to the instrument such as aperture size, detector area, efficiency etc..

2.3.3 CIS

The ion moments and velocity distribution data are obtained from the Cluster Ion Spectrometer (CIS) instrument (Reme et al., 2001), which consists of two different sensors, the Hot Ion Analyser (HIA) and the time-of-flight ion COmposition DIstribution Function Analyser (CODIF). CODIF is designed to distinguish between particles of different masses (H^+ , He^+ , He^{2+} and O^+). Both instruments are top hat analysers; HIA has an energy/charge ratio in the range of $\sim 5 \text{ eV/q} - 32 \text{ keV/q}$ and CODIF has an energy/charge ratio in the range of $\sim 15 \text{ eV/q} - 38 \text{ keV/q}$.

Both HIA and CODIF are top hat analyser and work in the same basic way as PEACE. However, in order for CODIF to distinguish between ions of different species, the ions are passed through a thin carbon foil which creates a cloud of secondary electrons which are detected at a secondary detector. The detection of the electrons triggers a timer which measures the time required for the ion to move from the foil to the primary detector (time of flight). From the time of flight and the geometry of the analyser, the charge per mass can be found, the charge per mass of an ion can be used to identify the ion.

Like PEACE, CIS can produce 3D distributions, pitch angle distributions and moments. CIS data is not available from either HIA or CODIF on C2 nor from HIA on C4. Observations for C1 and C3 in this chapter were made by HIA and observations of C4 by CODIF. During the observations presented here, HIA on C1 and C3 had a resolution of 4 seconds and CODIF on C4 had a time resolution of 8 seconds. The data presented here have been corrected for known instrumental effects.

All of the plasma moments data presented in this chapter are derived from CIS data, except for those from C2 (for which CIS data is unavailable), PEACE moments are used in its place. The FGM, CIS and PEACE data were all obtained from the Cluster Active Archive except for the C4 CODIF data which was supplied directly by the CIS team after instrumental artifacts had been removed.

2.3.4 Cluster location and separation

In order to obtain the most complete picture of the disturbance causing the TCR (dubbed here the “magnetic structure”), events for which the spacecraft separations are close to the expected size of the magnetic structure itself are sought. This provides measurements of the passing structure from the multiple Cluster spacecraft which are then likely to have a good spread of impact parameters. In the case of Earthward-moving structures, these are typically reported as being 2-5 R_E in diameter (e.g., Slavin et al., 2003a). Cluster separations best fulfill this requirement during the 2006 and 2007 tail seasons (July-November each year), during which the typical separations between spacecraft were of the order of 10,000 km.

The Cluster data was searched during the aforementioned times and a list of observed bipolar signatures was compiled, which is included in the appendix (Section 6.1); the most intriguing event is the studied in this chapter. This chapter presents the results of a case study of observations made between 04:40-04:45 UT on 07 October 2006, at which time the individual spacecraft clearly sampled different parts of a passing magnetic structure. The spacecraft were located within the magnetotail, with C3 at (-13.97, 5.11, -1.92) R_E at 04:42 UT. The positions of the spacecraft relative to C3 are illustrated in Figure 17. The three panels show the relative spacecraft locations in the XY, XZ and YZ planes. The four spacecraft were in a near regular tetrahedral formation with C3 ~ 6,000 km south of the other spacecraft, while C1, C2 and C4 were within 3,000 km of each other in Z.

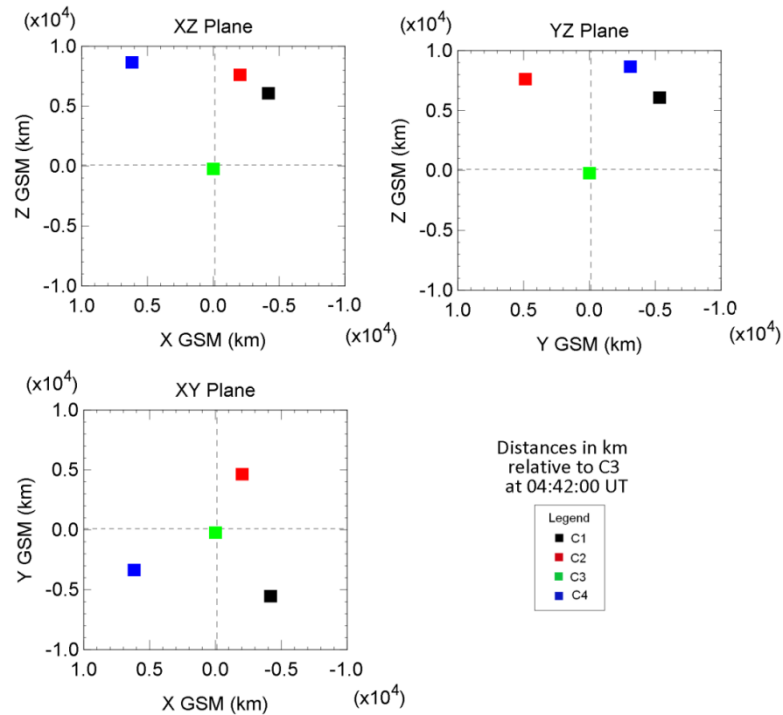


Figure 17. Spacecraft position in GSM, relative to C3 at 04:42:00 UT on 07 October 2006. The top left panel shows the XZ plane, the top right shows the YZ plane and the bottom left shows the XY plane. C1 is represented by the black square, C2 is red, C3 is green and C4 is blue. The spacecraft were in the magnetotail in an approximate tetrahedral formation with C3 lower than the other spacecraft in Z by $\sim 6,000$ km. C1, C2 and C4 were within 3,000 km of each other in Z.

2.4 Observations

Figure 18 shows the magnetic field and the electron data recorded between 04:15 – 05:15 UT on 07 October 2006. The top 4 panels each show the B_X (red trace), B_Y (green trace) and B_Z (blue trace) components of the magnetic field, together with the field magnitude (black trace), for each of the 4 spacecraft. The lower 4 panels show spectrograms of direction-averaged electron differential energy flux (DEF) over the PEACE energy range versus time at each spacecraft. Initially, all four spacecraft were located in a region of strong and steady magnetic field (directed in positive

B_x) with low particle DEF. This region is identified as the lobe. At $\sim 04:38$ UT, C3 entered the central plasma sheet (CPS); the region is characterised by a relatively weak and more variable magnetic field and relatively enhanced plasma DEF, especially evident at higher energies.

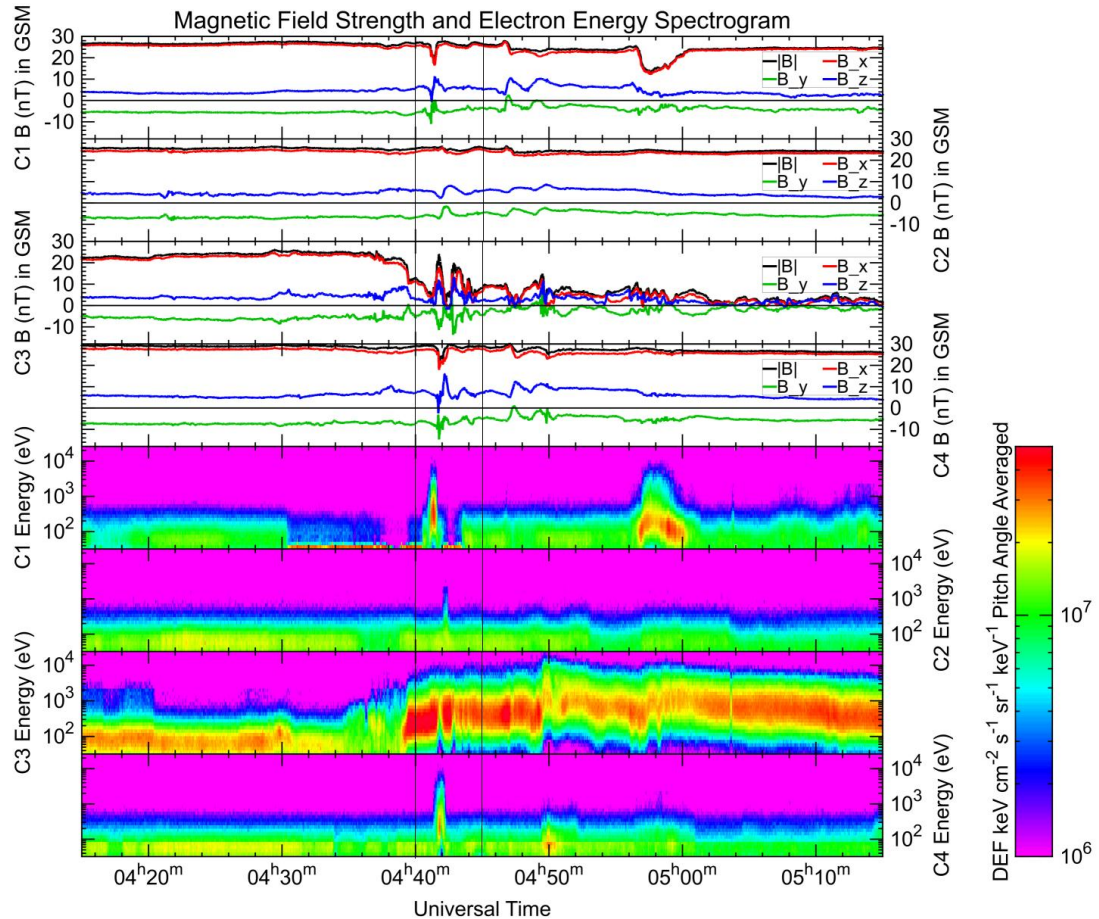


Figure 18: Panels 1, 2, 3, 4 shows the magnetic field strength for C1, C2, C3, C4 respectively (B_x is in red, B_y is in green B_z is in blue and $|B|$ is in black). Panels 5, 6, 7, 8 show the (pitch angle averaged) electron energy spectrogram of C1, C2, C3, C4 respectively. Between 04:40-04:50 UT, C1, C2 and C4 encountered a set of bipolar signatures in B_z , the largest of which was detected between 04:40-04:45 UT, marked by the two dark vertical lines. Coinciding with the bipolar signature, C1, C2 and C4 detected an increase in electron DEF. Between the marked times, C1, C2 and C4 were in a region of a large steady B_x and low electron DEF which indicates that they were in the lobe. C3 was in a region of low, varying B_x with a high electron DEF which indicates that it is in the central plasma sheet.

Between 04:40 - 04:50 UT, C1, C2 and C4 detected a set of bipolar signatures in B_z . The first, largest and most significant bipolar signature is observed between 04:40 - 04:45 UT, a time marked by the vertical lines in Figure 18; the following considers this event in more detail and on a spacecraft-by-spacecraft basis. This is presented in the order C2, C4, C1 and C3, which reflects the order of decreasing impact parameter (deduced from the observations presented below).

Over a longer period of time (not shown), the plasma sheet appears to be ‘flapping’ (e.g. Sergeev et al., 2008; Zhang et al., 2002; Runov et al., 2005; Forsyth et al., 2009). This is the oscillatory motion of the plasma sheet in the direction perpendicular to the current sheet. However, as the period of the oscillation (~30 mins) is much greater than the time scale of the signature of interest (~5 mins), it seems unlikely that the latter may arise as a manifestation of the former and hence the possibility is ruled out.

Figure 19 shows the data from C2 for the period 04:40 - 04:45 UT. Panel 1 shows the magnetic field strength and GSM components (B_X , B_Y , B_Z and $|B|$ are in red, green, blue and black respectively). Panel 2 and 3 respectively show an electron energy spectrogram (pitch-angle-averaged) and an electron pitch angle spectrogram (energy-averaged) of the observed DEF (in units of $\text{keV}/(\text{cm}^2 \text{ s sr keV})$). Panels 4-7 show electron density, electron temperature, electron β and electron perpendicular velocity respectively. The particle perpendicular velocity is the velocity of the particles in the direction perpendicular to the magnetic field and is represented by the symbol V_{\perp} , this can be used as a proxy for the velocity of the magnetic structure, the link between the two is as follows: In regions in which ideal MHD is a valid approximation, magnetic field lines are frozen into the plasma and hence they convect together. Particles may drift freely parallel to the field lines but not perpendicular and hence any perpendicular particle motion is indicative of the movement of the magnetic field lines; this can provide information on the convection of any underlying magnetic structure. The perpendicular particle velocity is defined as $\mathbf{V}_{\perp} = \hat{\mathbf{b}} \times \mathbf{V} \times \hat{\mathbf{b}}$, where $\hat{\mathbf{b}}$ is the unit magnetic field and \mathbf{V} is the particle velocity.

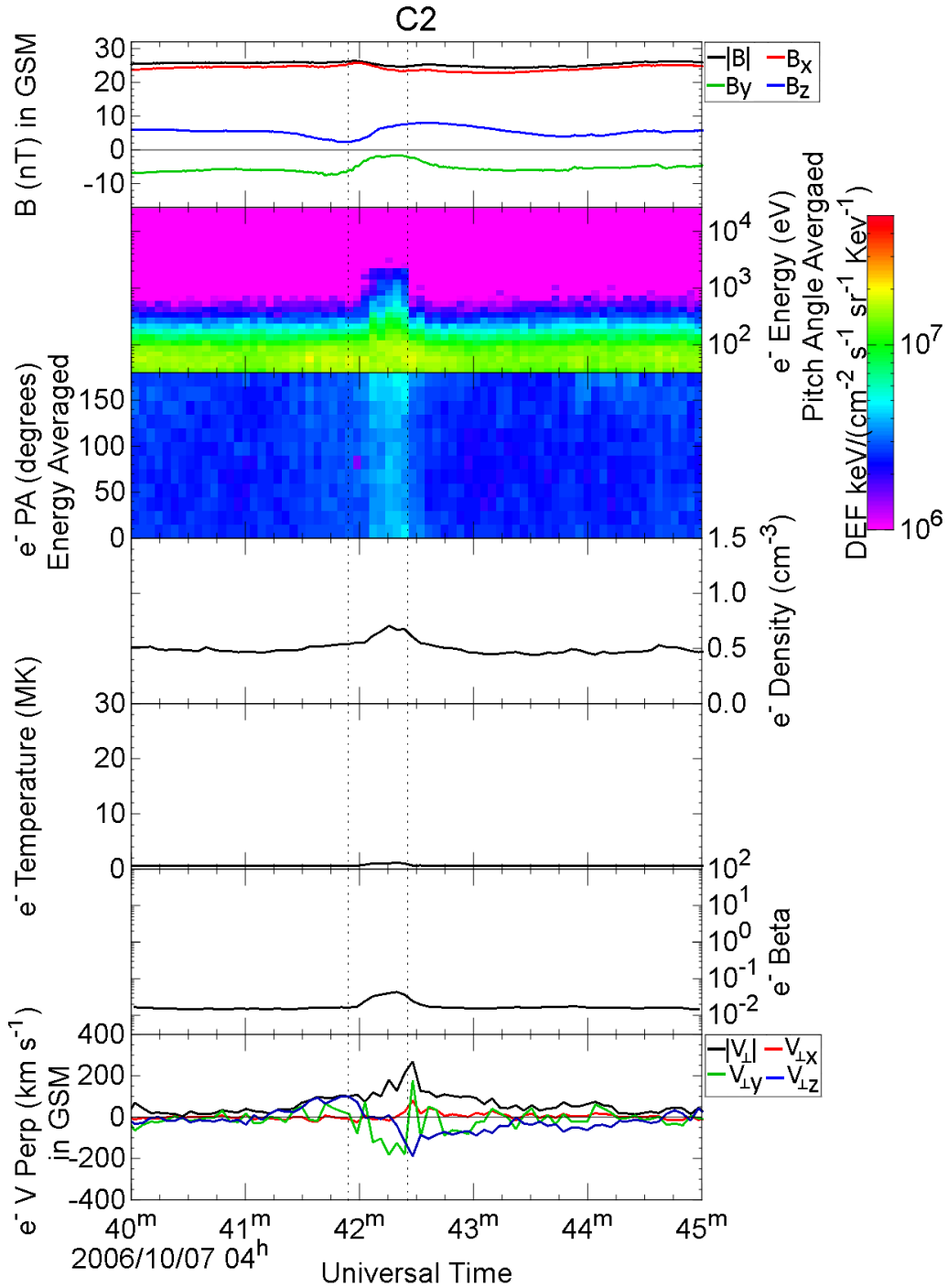


Figure 19. C2 observations. From top to bottom the panels shows the magnetic field strength (B_x is red, B_y is green, B_z is blue and $|B|$ is black), an electron energy spectrogram (pitch angle averaged), electron pitch angle spectrogram (energy averaged), electron density, electron temperature, electron β and electron perpendicular velocity. Between 04:41-04:43 UT, the data shows little change in B_x and $|B|$, a peak in B_y and a bipolar signature in B_z . Simultaneously, an increase can be seen in the electron DEE, density and temperature.

Across most of the time period, electron $\beta < 0.04$ which indicates that the spacecraft is in the lobe. At $\sim 04:42$ UT, the observations indicate that C2 observed a clear negative-positive bipolar signature in the B_Z component, with a peak-to-peak amplitude of ~ 6 nT. The dotted vertical lines mark the turning points of this bipolar signature. Simultaneously, the B_Y component changed from ~ -7 nT to ~ -2 nT, while B_X and $|B|$ show much smaller variations. The duration of the bipolar signature (measured from peak to peak) is ~ 31 seconds. Each of the magnetic field traces in Figure 19 show a generally smooth profile to the variations.

During the bipolar magnetic signature, there is also a slight increase in the electron DEF at energies under 3 keV at all pitch angles; the increase in DEF is also reflected in the concurrent increase in the electron density, temperature and β . The electron β increases to ~ 0.04 , this combined with the observation of field-aligned electrons indicate that the spacecraft is in the outer CPS/PSBL at the time. Moderate flows are seen in the perpendicular velocity; $V_{\perp X}$ shows only a small peak and $V_{\perp Z}$ shows a north-south bipolar signature.

Figure 20 shows the data from C4. Panel 1 shows the magnetic field strength and GSM components (B_X , B_Y , B_Z and $|B|$ are in red, green blue and black respectively). Panels 2-5 respectively show a proton energy spectrogram (pitch angle averaged), a proton pitch angle spectrogram (energy averaged), an electron energy spectrogram (pitch angle averaged) and an electron pitch angle spectrogram (energy averaged) of differential energy flux (in units of $\text{keV}/(\text{cm}^2 \text{ s sr keV})$). Panels 6-9 show proton density, proton temperature, proton β and proton perpendicular velocity.

This spacecraft begins in the lobe (inferred from proton β of < 0.3); at $\sim 04:42$ UT it detects a negative-positive bipolar signature in B_z . The peak-to-peak amplitude is ~ 18 nT. The first half of the bipolar signature shows more variability than the second. Coinciding with the bipolar signature, B_y peaks while B_x and $|B|$ show significant dips of ~ 9 nT and ~ 5 nT respectively. The duration of the bipolar signature (again measured from peak to peak) is ~ 29 seconds.

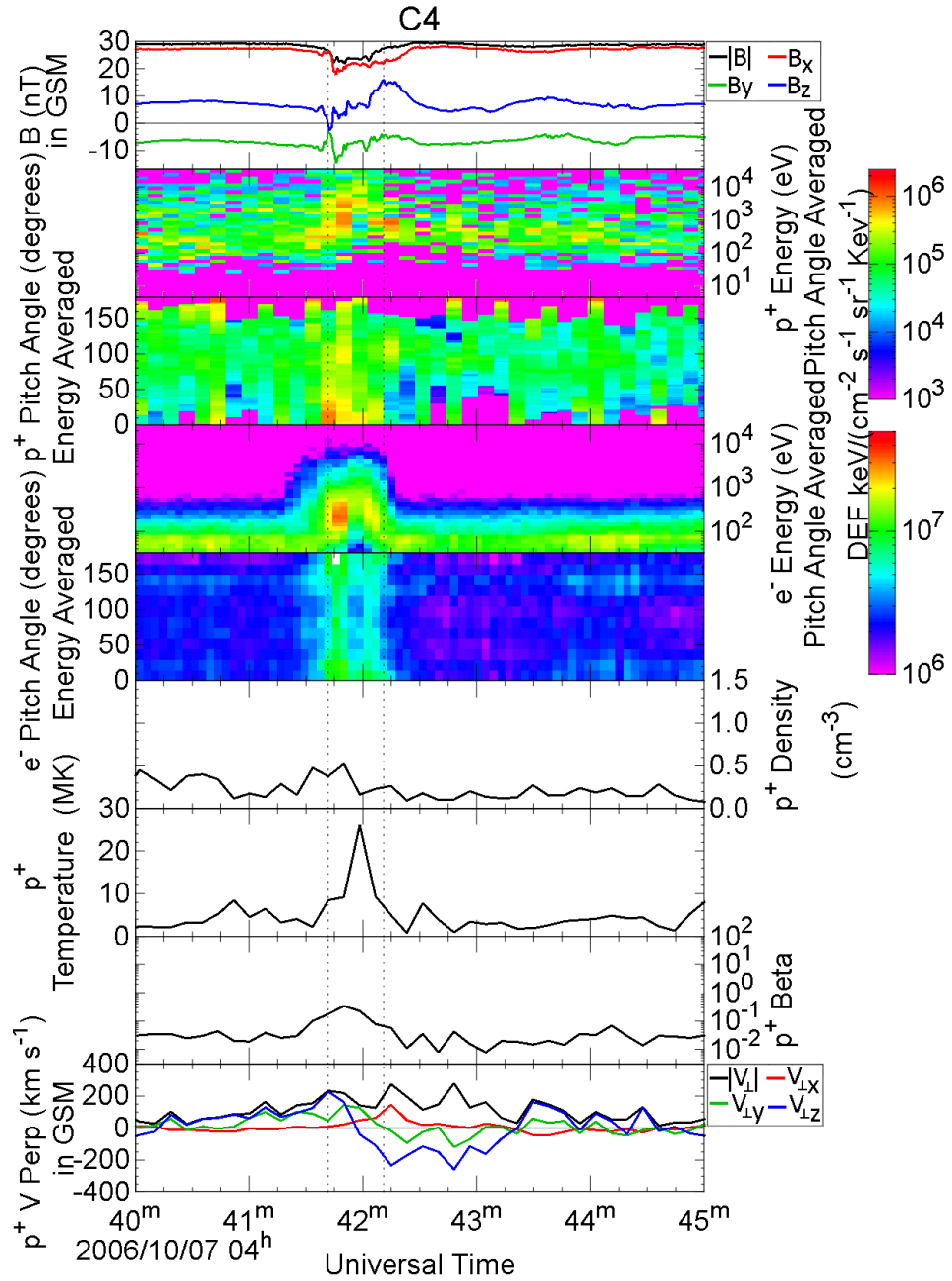


Figure 20: C4 observations. From top to bottom the panels show magnetic field strength (B_X is red, B_Y is green, B_Z is blue and $|B|$ is black), proton energy spectrogram (pitch angle averaged), proton pitch angle spectrogram (energy averaged), electron energy spectrogram (pitch angle averaged), electron pitch angle spectrogram (energy averaged), proton density, proton temperature, proton β and proton perpendicular velocity. Between 04:41-04:43 UT, C4 detected a dip in B_X and $|B|$, a peak in B_Y and a bipolar signature in B_Z . The spectrograms show two increases in DEF at the turning points of the bipolar signature; the increase in electron DEF was larger at the negative excursion than at the positive excursion. The increase in proton DEF was centred on a pitch angle of 0° .

The proton energy and pitch angle spectrograms show two increases in DEF which coincide with the turning points of the bipolar signature. They are centred on a pitch angle of 0° ; the increase during the negative excursion has a greater pitch angle range and energy range compared to that observed during the positive excursion. The electron DEF also shows two increases at the turning points of the bipolar signature, the increase in DEF during the negative excursion is greater than that observed during the positive excursion. The pitch angle spectrogram shows the increase in electron DEF is greater for the 0° and 180° pitch angle electrons compared to the 90° pitch angle electrons. The changes to the particle distributions also result in accompanying increases in both the density and temperature; the density peaks during the negative excursion of the bipolar signature while the temperature peak coincides with the centre of the bipolar signature. During the bipolar signature, proton $\beta \sim 0.3$ and the electrons are field aligned indicating that the spacecraft is in the outer CPS/PSBL at this time. The proton perpendicular velocity shows a north-south bipolar signature in $V_{\perp Z}$ and a peak in $V_{\perp X}$ of $\sim 150 \text{ km s}^{-1}$.

Figure 21 displays the data from C1 in the same format as Figure 20, except showing ion data in place of proton data. Initially, C1 is in the lobe (inferred from ion β of < 0.3); at $\sim 04:40:30$ UT it moves into a region of higher density lobe. At $\sim 04:41:20$ UT C1 detected a negative-positive bipolar signature in B_Z with a peak-to-peak variation of ~ 11 nT. The B_Y component shows some variability and decreased from a background value of ~ -6 nT to ~ 0 nT during two dips which closely coincide with the turning points of the bipolar signature. The B_X component and $|B|$ show a reduction of ~ 11 nT, with the minimum closely coinciding in time with the positive excursion of the bipolar B_Z signature. The duration of the bipolar signature (measured from peak to peak) is ~ 19 seconds.

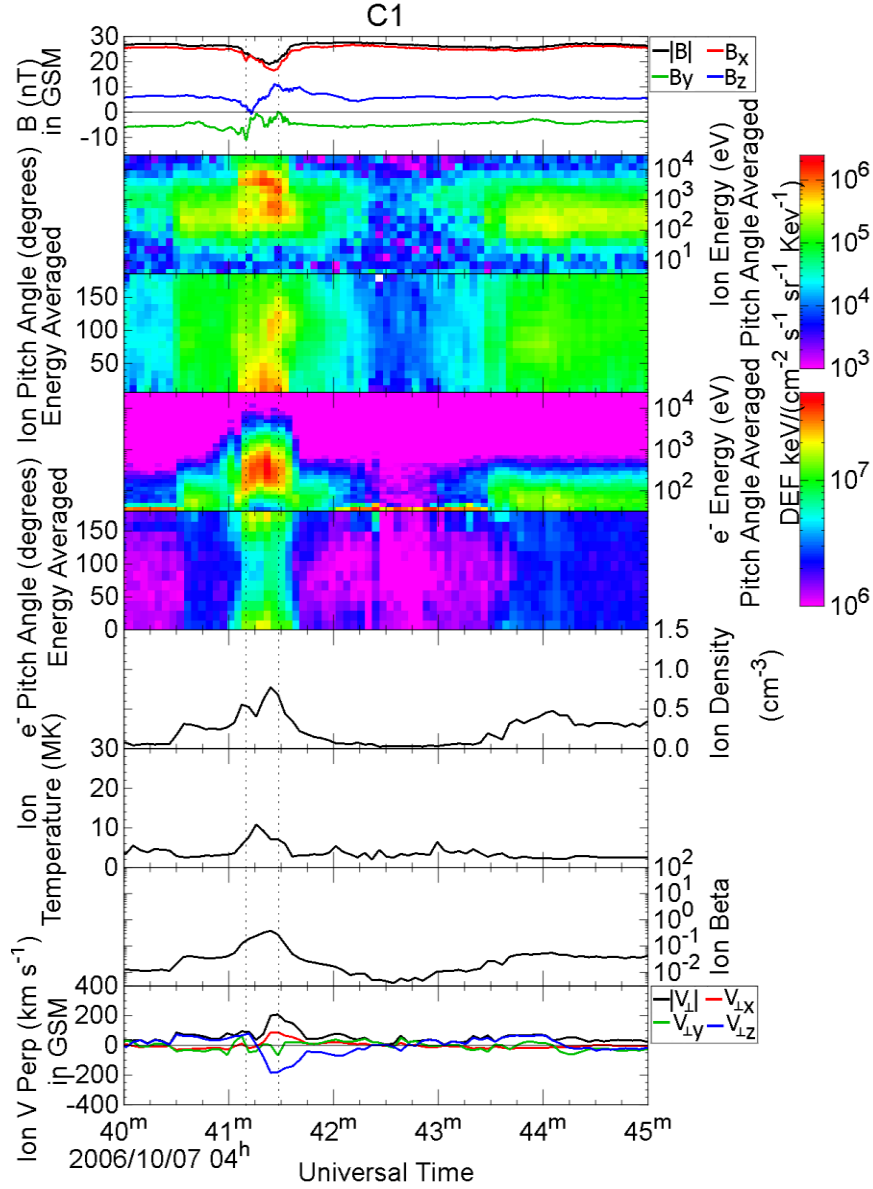


Figure 21: C1 observations. From top to bottom the panels show magnetic field strength (B_X is red, B_Y is green, B_Z is blue and $|B|$ is black), ion energy spectrogram (pitch angle averaged), ion pitch angle spectrogram (energy averaged), electron energy spectrogram (pitch angle averaged), electron pitch angle spectrogram (energy averaged), ion density, ion temperature, ion β and ion perpendicular velocity. Between 04:41-04:43 UT, C1 detects a dip in B_X , two dips in B_Y and a bipolar signature in B_Z . The ion DEF increases at 0° and between 1,500 eV-32,000 eV; simultaneously, two increases are seen between 200-1,500 eV centred on 90° and 110° . An increase in electron DEF (100-10,000 eV) can be seen at all pitch angles, which was greatest at 0° and 180° .

In Figure 21, the magnetic variations are accompanied by changes in the particle distributions. At the turning points of the bipolar signature were two separate increases in ion DEF at energies between 200 - 1,500 eV, which are centred on pitch angles of $\sim 90^\circ$ and $\sim 110^\circ$ respectively. The increase at the positive excursion of the bipolar signature covers a wider pitch angle range and has a larger ion DEF and duration compared to the increase at the negative excursion. Simultaneously, another increase in ion DEF, centred on 0° , can be seen at higher energies (between 1,500 - 32,000 eV); this increase is centred on the centre of the bipolar signature. During the bipolar signature, there was an increase in electron DEF (100 - 10,000 eV) at all pitch angles, which was greatest for the field-aligned/anti-field aligned directions; the electron enhancements were also centred on the centre of the bipolar signature. Large electron DEFs were observed at low energies (< 50 eV) between 04:40:00 - 04:40:30 UT and 04:42:00 - 04:43:30 UT. However, these represent photoelectrons of spacecraft origin and are not an inherent feature of the magnetic structure.

During the bipolar signature, ion β reaches 0.4 and the electrons are field aligned indicating that the spacecraft is in the outer CPS/PSBL at this time. The ion density shows two separate peaks near the turning points of the bipolar signature. The second peak (which coincides with the positive excursion) was larger than the first, much like the increases in ion DEF. The ion temperature shows a peak caused by the higher energy ions seen in the spectrogram. The ion perpendicular velocity shows only moderate flows, with a north-south bipolar signature in $V_{\perp Z}$ and a peak in $V_{\perp X}$ at $\sim 100 \text{ km s}^{-1}$.

Figure 22 contains the data from C3 in the same format as Figure 21. The C3 data shows a significantly different set of variations from those described above for the other 3 spacecraft. The spacecraft were in a region which is characterised by a relatively weak (~ 10 nT) and more variable magnetic field. Moreover, this spacecraft observes relatively high DEFs of ions (peaked near 1 keV) and electrons (peaked at a few hundred eV) and a high ion β (> 1) throughout the majority of this period, leading to generally higher densities and temperatures than those observed at the other spacecraft. These observations suggest that C3 was immersed in the CPS. Moreover at 04:42:30 UT, B_x was close to zero, which suggests that the spacecraft was close to the neutral sheet at this time.

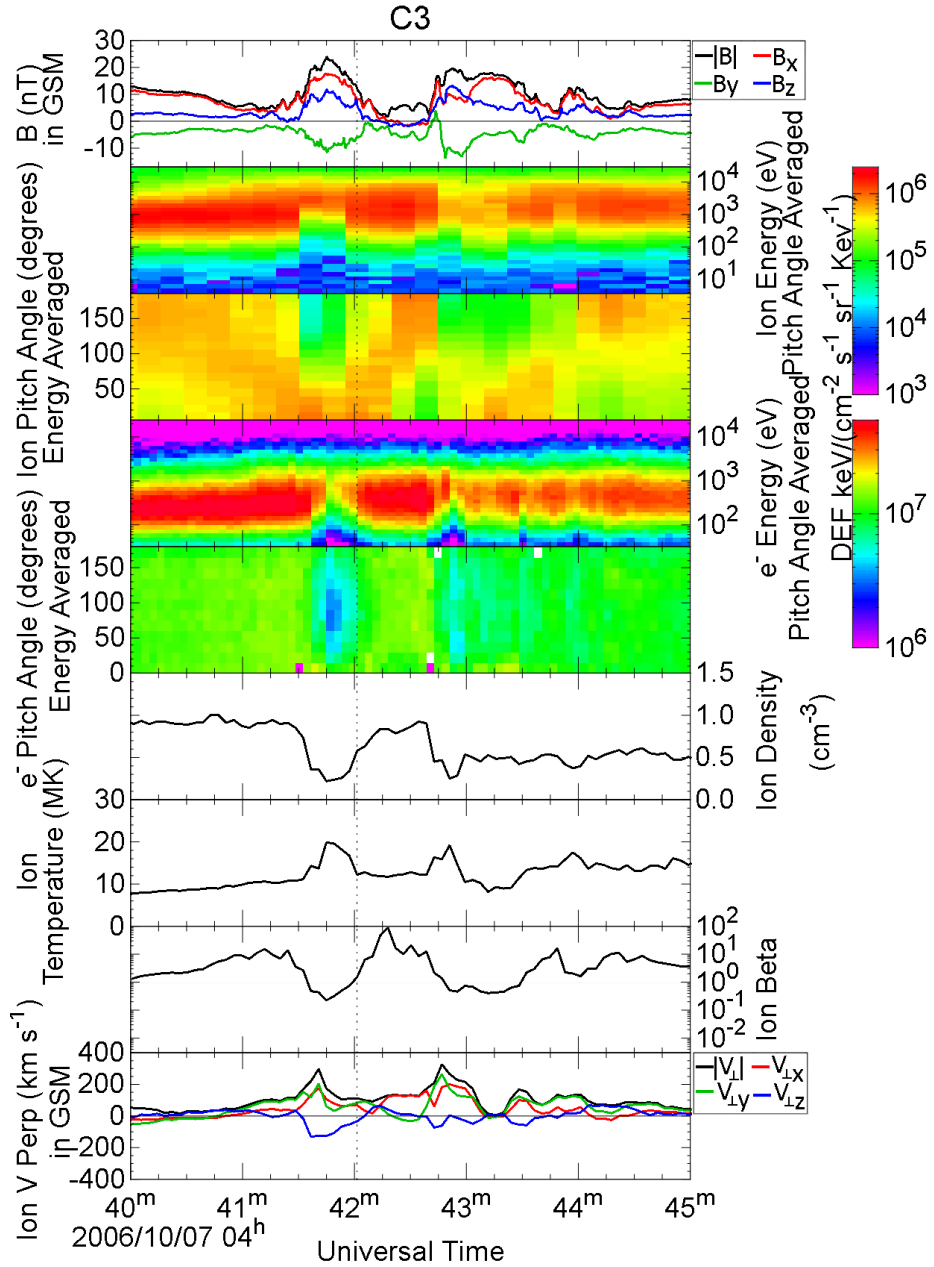


Figure 22: C3 observations. From top to bottom the panels show magnetic field strength (B_x is red, B_y is green, B_z is blue and $|B|$ is black), ion energy spectrogram (pitch angle averaged), ion pitch angle spectrogram (energy averaged), electron energy spectrogram (pitch angle averaged), electron pitch angle spectrogram (energy averaged), ion density, ion temperature, ion β and ion perpendicular velocity. Across the time period, the magnetic field strength, temperature and perpendicular velocity exhibit a series of temporary increases, in conjunction with decreases in the particle DEF and density. The decreases in electron DEF are centred on 90° . Centred on 04:42:15 UT and 04:44:00 UT, the ion pitch angle spectrogram shows two rotations from 0° to 180° .

Considering now the departures from this background, note that there is no stand-out bipolar B_Z signature in the C3 data during this period. Instead, a series of peaks at 04:41:45 UT, 04:43:15 UT and 04:44:00 UT, are observed in all 3 magnetic field components, which appear to vary closely in concert. At the times of the magnetic maxima, there was a reduction of the ion and electron DEF, ion density, ion β and an increase in ion temperature and ion perpendicular velocity. The reduction in electron DEF was predominantly in the direction perpendicular to the field, this, combined with $\beta \sim 0.3$ indicates that the spacecraft is in the outer CPS/PSBL at these times. The ion pitch angle spectrogram (panel 3) shows two clear migrations between 0° and 180° centred on 04:42:15 and 04:44:00 UT. For both rotations, while the pitch angle distribution is peaked at 0° , B_X is the greatest component and while peaked at 180° , B_X has reduced and B_Y has increased. In both cases the variation in the directionality of the peak flux is not a full 180° rotation in real space. After the magnetic variation ceased, the ion and electron DEFs and densities are reduced to below the pre-event levels.

2.5 Analysis

2.5.1 Orientation of Magnetic Structure

The following attempts to identify a co-ordinate system which may be aligned with any 'quasi-invariant' axis of the structure responsible for the observations at each spacecraft which were described in the last section. To establish this co-ordinate system (which may also determine the orientation of the structure) the minimum variance analysis (MVA) (Sonnerup and Cahill, 1967; Sonnerup and Scheible, 1998) was applied to the magnetic field data from each spacecraft.

Minimum variance analysis performed on any vector dataset returns three eigenvectors (corresponding to the directions of the maximum, intermediate and minimum variance) and their associated eigenvalues (which are related to the size of the variation of the data components along the corresponding axis). The ratios of the intermediate/minimum and maximum/intermediate eigenvalues can be used as a measure of confidence in the determined axes (greater ratios indicate a greater confidence). A ratio of 10 is often used as the lowest acceptable accuracy (e.g. Paschmann et al., 1998). An eigenvalue ratio of 1 indicates that the associated eigenvectors are degenerate and that the uncertainty in their direction is thus 360° .

The results of MVA are somewhat subjective, and must be calculated and used with care. They are sensitive to the time interval across which the analysis is applied. For the event studied here, the greatest eigenvalue ratios tended to come from time limits imposed at the turning points of a

bipolar signature as this is the region of greatest rate of change of magnetic field and direction. The turning points of the 3 bipolar signatures observed by C1, C2 and C4 also provide well-defined points seen in the all three magnetic signatures which facilitate comparisons between them.

As the C3 observations do not include an obvious bipolar signature and hence do not immediately match those of the other spacecraft, C3 data was not used in MVA calculations; the observations of C2 were also disregarded as this spacecraft passed outside of the structure. C1 and C4 both pass through the structure and hence the MVA calculations were based on the observations of these two spacecraft. The MVA axes were calculated using the time limits defined by the turning points of the bipolar signatures, the average of the MVA C1 and C4 axes was then taken. The MVA axes of C1 were within 33° of the equivalent C4 axes. The resulting MVA axes are as follows (in the format X, Y, Z in GSM): the vector of the minimum variance axis is (0.886, -0.335, 0.321), intermediate variance axis is (0.379, 0.897, -0.228), maximum variance axis is (-0.205, 0.288, 0.935). For comparison, the minimum, intermediate, maximum variance directions are loosely aligned ($<32^\circ$) with X, Y, Z GSM respectively.

2.5.2 Velocity Calculation

Figure 10, Figure 11 and Figure 12 show the bipolar signature is the largest magnetic variation (and hence occurs in the maximum variance axis) and is perpendicular to the current sheet plane in both models. As mentioned previously, the flux rope and flux bulge both travel in the current sheet plane; hence the magnetic structure must be travelling in the plane

perpendicular to the maximum variance axis (the minimum-intermediate plane).

During the passage of the magnetic structure, a peak in perpendicular particle velocity would indicate the velocity of the magnetic structure. Although $V_{\perp Y}$ and $V_{\perp Z}$ do vary greatly during the bipolar signature, the signatures are not peaks and hence the variations in these components are caused by additional factors. However $V_{\perp X}$ does show a peak and can therefore be partly representative of the velocity of the structure. The $V_{\perp X}$ peaks of C1, C2 and C4 range from 80-150 km s⁻¹. The velocities are expected to be the same as they are of the same structure; the difference in the peak values could be due to several factors including the low data resolution (1 vector per 4 and 8 seconds for C1 and C4 respectively), the time of the $V_{\perp X}$ peak relative to the centre of the bipolar signature and the peak in density, the location of the spacecraft during the encounter etc.. The velocity will instead be determined using the position and encounter times of the structure with the spacecraft.

In order to deduce the speed of the magnetic structure, it was assumed that the magnetic structure was travelling at a constant speed and the distance between the spacecraft does not significantly change over the time periods of interest; the assumptions combined with the encounter times and locations of the spacecraft were used to calculate the speed of the magnetic structure. The ratio of the time difference between the encounters of the magnetic structure with C1 & C2 and C1 & C4 is expected to be the same as the ratio of the distances between the spacecraft in the direction of travel. To calculate the direction of travel (which, as mentioned previously, is in

the minimum-intermediate plane), the ratio of the distance between the spacecraft was calculated for all angles in the minimum-intermediate plane. The angle at which the distance ratio was closest to the time ratio was taken as the direction of travel. This was found to be 10° anti-clockwise of the intermediate axis. The direction of travel agrees with the observed order in which the magnetic structure encounters the spacecraft (C1, C4, C2).

Using the direction of travel, the spacecraft locations and the encounter times, the magnetic structure was found to be moving at $(99, 154, -31) |186| \text{ km s}^{-1} \text{ GSM}$ (which is in the format $(V_x, V_y, V_z) |V|$). Using this velocity, the locations of the spacecraft and the encounter times of the spacecraft with the magnetic structure, an estimate was calculated for the encounter time of the magnetic structure and C3 which was estimated to be 04:42:01 UT. To align the coordinate system with the direction of travel of the magnetic structure, the coordinate system was rotated by 10° anti-clockwise about the maximum axis (to cause a rotation in the minimum-intermediate plane); the direction of travel is now parallel to the intermediate variance direction. The resulting MVA axes are as follows (in the format X, Y, Z in GSM): the vector of the minimum variance axis is $(0.801, -0.483, 0.354)$, intermediate variance axis is $(0.531, 0.830, -0.170)$, maximum variance axis is $(-0.205, 0.288, 0.935)$. From here onwards, reference to the MVA axes refers to the rotated axes.

2.5.3 Configuration in MVA derived co-ordinate system

Figure 23 shows the spacecraft positions in the MVA co-ordinate system at 04:42:00 UT, a time close to that at which all three bipolar signatures were observed. The panels of the plot show the ‘minimum’-‘maximum’ plane in the top left, the ‘intermediate’-‘maximum’ plane in the top right and the ‘minimum’-‘intermediate’ plane in the bottom left. The spacecraft are coloured black, red, green and blue for C1, C2, C3 and C4 respectively.

As mentioned previously, the maximum variance axis is perpendicular to the current sheet and hence the position of the spacecraft in this axis can hence be used as a proxy for the relative height of the spacecraft above the current sheet and thus the crossing height, or impact parameter, of the spacecraft through magnetic structure. The order in impact parameter deduced from the MVA coordinate system (from smallest to largest) is C3, C4, C1, C2. This agrees with the observations which show that C3 is in the CPS and that C2 observes a TCR indicating they have the lowest and highest impact parameter respectively. In addition the observations show the enhancement in the electron DEF is greater at C1 than at C4, which is expected since C1 has a lower impact parameter than C4.

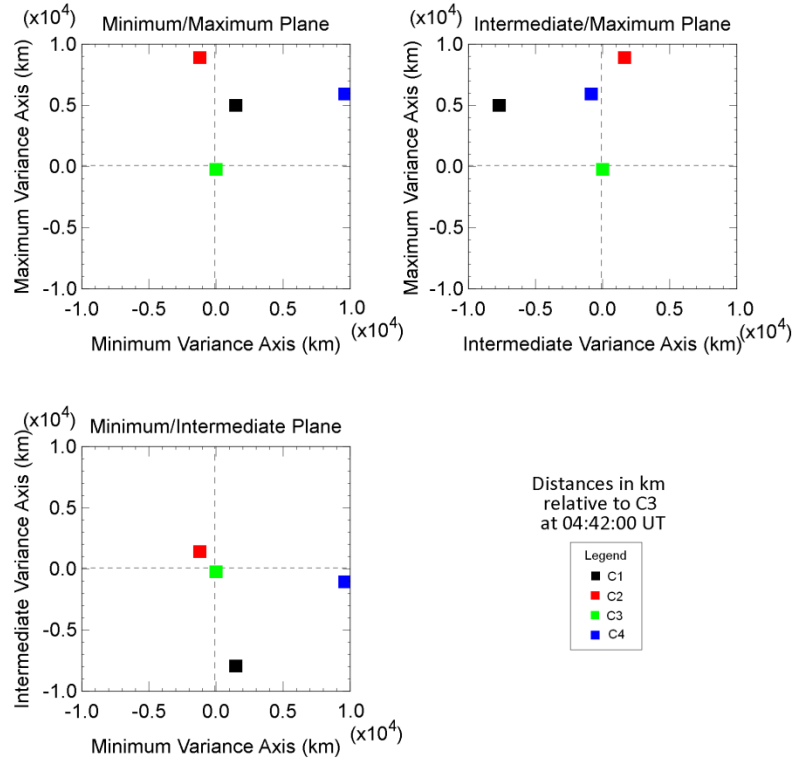


Figure 23: Configuration of the spacecraft in the MVA co-ordinate system. C1, C2, C3 and C4 are in black, red, green and blue respectively. The panels show the ‘minimum’-‘maximum’ plane in the top left, the ‘intermediate’-‘maximum’ plane in the top right and the ‘minimum’-‘intermediate’ plane in the bottom left. The direction of travel of the magnetic structure is along the intermediate variance direction; the plot shows the magnetic structure is expected to encounter the spacecraft in the order C1, C4, C2 which agrees with the observed times. The axis of impact parameter is parallel to the maximum axis. The order of the spacecraft in this axis is (from smallest to largest) C3, C1, C4, C2 which agrees with the observations.

Conflicting with this, the observations also suggest C1 is at a higher impact parameter than C4. For example, initially C1 observes a lower density than C4; lower density regions are expected at the higher impact parameters. In addition, C4 has a larger (in peak-to-peak magnitude) bipolar signature compared to C1 which is expected at lower impact parameter crossings, however this can be explained by the different plasma distributions. Coinciding with the both excursions of the C1 bipolar signature is an increase in electron DEF, at C4, this occurs mostly at the negative

excursion. This leads to a greater diamagnetic reduction and lower peak of the positive excursion of C1 compared to that of C4 (electron data was compared, ion data could not be directly compared because the C1 plots contain ion data whereas the C4 plots contain proton data). As the observations are somewhat inconclusive, the ordering calculated from the MVA coordinate system is used.

2.5.4 Observations in MVA derived co-ordinate system

Figure 24 shows the observations plotted in the MVA co-ordinate system. From top to bottom, the first two panels are of magnetic field strength and perpendicular velocity of C2, followed by the same for C4, C1 and C3 respectively. In each plot, the component in the minimum, intermediate and maximum variance direction is in red, green and blue respectively and the magnitude is in black. The perpendicular velocity of C1 and C3 is derived from the ions, C4 from the protons and C2 from the electrons. The plot includes dotted lines marking the turning points of the bipolar signature and the magnetic structure's estimated encounter time with C3.

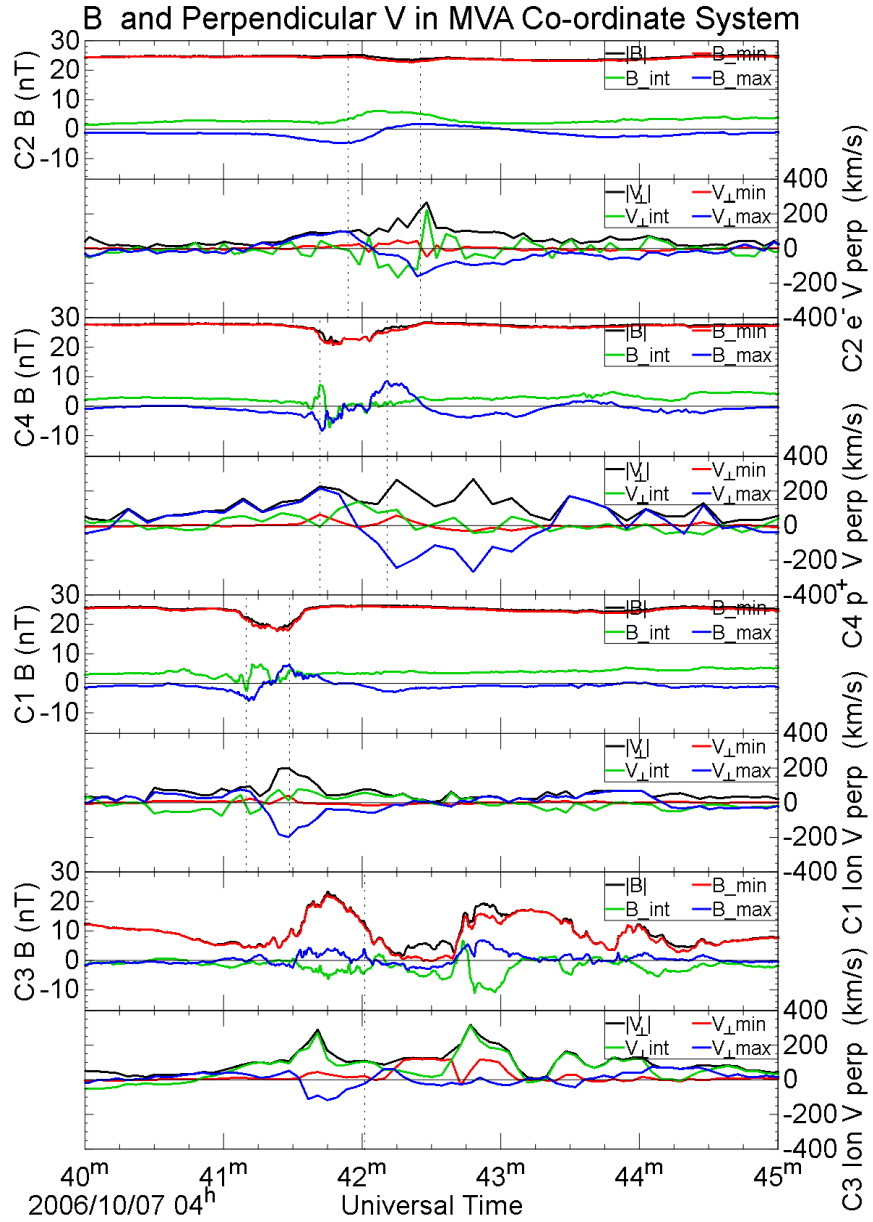


Figure 24 Observations in the MVA co-ordinate system. The panels show, from top to bottom, the magnetic field strength and perpendicular velocity of C2, C4, C1 and C3. The magnitude is in black, the minimum, intermediate and maximum components are in red, green and blue respectively. The dotted lines mark the turning points of the bipolar signature in all plots except C3 where it represents the estimated encounter time of the magnetic structure with C3. Between 04:41-04:43 UT, C1, C2 and C4 observe bipolar signatures in B_{MAX} which are centred on 0. In C3 the variations occur mostly in B_{MIN} .

Figure 24 also includes observations of the perpendicular velocity. The data displayed in Figure 24 are from the same data sources as Figure 19 - Figure 22. Figure 24 shows the magnetic bipolar signatures of C1, C2 and C4 in this co-ordinate system are centred on zero indicating that the choice of maximum variance axis is accurate and perpendicular to the current sheet. The variations in C3 due to the reduction of the diamagnetic effect are mostly contained in B_{MIN} in this coordinate system. The estimated encounter time (04:42:01 UT) of the magnetic structure with C3 falls halfway between the first magnetic maximum (which coincides with PSBL-like plasma) and the magnetic minimum (between the first two magnetic maxima, which coincides with CPS-like plasma). As both models predict a structure containing CPS-like plasma, the CPS plasma observed at the C3 magnetic minimum is assumed to be the PO region associated with the magnetic structure.

The plasma density at the C3 was enhanced for ~ 40 seconds during the magnetic minimum. Using this time and the velocity calculated previously, the magnetic structure is found to be $\sim 1.19 R_E$ in size. As C3 is close to the neutral sheet whilst inside the magnetic structure, the minimum size of the magnetic structure (in the direction perpendicular to the current sheet) can be estimated by calculating the distance between the spacecraft close to its centre (C3) and the spacecraft with the highest impact parameter that crosses through the magnetic structure (C4). The minimum size, from centre to edge, in the maximum variance direction is $\sim 0.97 R_E$. As C2 is outside of the magnetic structure, the distance between it and C3 can be used as a maximum size, this is $\sim 1.43 R_E$. Assuming that the structure is symmetrical north and south of the current sheet an estimate for the total

size can be found; from the outer edge on one side of the current sheet to the outer edge on the other side of the current sheet, the structure has a minimum of ~ 1.94 and a maximum of $\sim 2.86 R_E$.

The observed perpendicular velocity of the plasma at the centre of the magnetic structure (at the C3 magnetic minimum) is directed mostly in X (see Figure 22). This differs from the calculated overall velocity which is travelling mostly in Y. This can partly be explained by the direction of the field at the C3 magnetic minimum, which is mostly in Y; movement in that direction is parallel to the field and hence does not contribute to the convective velocity of the structure.

As mentioned previously, two rotations can be seen in the pitch angle. During the first rotation, the magnitude of the magnetic field strength is low and hence small changes in the magnitude of the individual components lead to large changes in the magnetic field direction. Hence the rotation in pitch angle is more likely due to the changes in the magnetic field direction. In contrast the second rotation has a much greater magnetic field magnitude. Hence this is more likely a true reversal of the pitch angle of the particles which is an indication of the presence of an X-line.

One could argue that a bipolar signature can be seen in C3 centred on 04:42:40 UT, comprising of the magnetic minimum and the second magnetic maximum. A greater plasma DEF coincides with the negative excursion compared to the positive excursion, and this observation is also apparent at C4 indicating that the two signatures may align at this point.

However, as the positive excursion of the possible bipolar signature of C3 coincides with an increase in magnetic field strength of all components, this is partly caused by a reduction in the diamagnetic effect caused by the concurrent reduction in plasma density. In addition the distribution of the plasma does not match that of C1, nor does it match the expected distribution of the plasma of the flux rope or flux bulge: In the case of the flux rope, the distribution of the plasma is expected to be symmetric about the inflexion point of the bipolar signature; in the case of the flux bulge, a CPS-like density coincides with the positive excursion of the bipolar signature. Neither is seen at C3, which shows an asymmetric distribution of the plasma and a PSBL-like plasma at the positive excursion of the bipolar signature.

2.6 Discussion

2.6.1 Interpretation of observations

Presented above was data recorded by the Cluster spacecraft on the 7th October 2006 between 04:40:00 and 04:45:00 UT, when the 4 spacecraft were located in the magnetotail. Prior to the arrival of the magnetic structure, C1, C2 and C4 detect an ion $\beta < 0.3$, an electron $\beta < 0.04$ and no field aligned electrons; this indicates that the spacecraft were in the lobe at that time.

Between 04:40 and 04:45 UT, C1, C2 and C4 each detected a bipolar signature in conjunction with an increase in plasma DEF, density, temperature and velocity, which are interpreted here as being due to the

motion of a magnetic structure past the spacecraft. The bipolar signature at C2 is smooth and relatively small in peak-to-peak magnitude when compared to that observed at C1 and C4. The particle DEF, density, temperature and velocity increases seen during the bipolar signature are also smaller for C2 compared to C1 and C4. However, the increase in density and temperature does not lead to a significant reduction in the magnetic field strength during the bipolar signature. The magnetic signature at C2 is consistent with a TCR signature (Slavin et al., 1992), formed by the draping and compression of the overlying magnetic field lines of the lobe around the structure.

The magnetic signature at C2 magnetic suggests that the draping signature is stronger in B_Y than in B_Z , which may indicate that either the magnetic structure does not extend uniformly in both a duskward and dawnward direction relative to C2 and the spacecraft passes over the dusk “end” of the magnetic structure, or that the plasma sheet bulge was larger in diameter to the dawnward side of the spacecraft (e.g. Slavin et al., 1993; 1999).

Further south of C2 were C1 and C4 which appear to have passed through the magnetic structure itself. During the bipolar signature, ion β at C1 reaches ~ 0.4 and at C4 reaches ~ 0.3 , both coincide with field aligned electrons; this indicates that both spacecraft detected outer CPS/PSBL-like plasma at this time.

Flux ropes and flux bulges are created both Earthwards and tailward of the (dominant) X-line and propagate away from the neutral line on each side.

The direction of travel can be deduced from their observed velocities and by the nature of their bipolar signatures. The magnetic signatures reported here and observed by C1, C2 and C4 exhibited a negative B_Z excursion followed by a positive B_Z excursion, which is consistent with an Earthward travelling magnetic structure. In addition, the perpendicular velocities of C1 (ion), C2 (electron) and C4 (proton) show a $+V_{\perp X}$ peak coinciding with the bipolar signature, which also indicates Earthward travel.

C3 generally observes much larger values of ion β , often $\gg 0.3$, indicating that it remains mostly in the CPS for most of the period under consideration. For two brief periods either side of the magnetic minimum, ion β falls to ~ 0.3 and the spacecraft observes field aligned electrons and hence moves to the outer CPS/PSBL. During the magnetic minimum, C3 observed an ion $\beta > 10$, indicating that it was deep in the CPS and B_X fell to 0 indicating that it was at the neutral sheet.

As mentioned before, over a longer time period the plasma sheet is flapping; the possibility that this is the cause of the bipolar signature was ruled out earlier and the perpendicular velocity in the MVA co-ordinate system reinforces this. The drop-outs of plasma sheet plasma in the C3 observations could be due to an oscillation of the plasma sheet in the maximum variance direction; movement of the plasma sheet away from the spacecraft would cause it to exit the plasma sheet (the spacecraft would observe an increased B due to the reduced diamagnetic effect). If this was the case, the change in plasma sheet direction of travel from south to north (reversal in V_{MAX}) would coincide with the peaks in B , but this is not seen in the observations.

In common with the other spacecraft, C3 generally recorded a positive B_x component of the magnetic field indicating that it mostly remained located north of the neutral sheet. The lowest B_x value in the magnetotail is expected to be at the neutral sheet, which, assuming the magnetic structure is centred on the neutral sheet, corresponds to an impact parameter of zero. Note that C3 observed a B_x value that is close to zero during the magnetic minimum which indicates that this spacecraft was located close to the neutral sheet at this time. Hence C3 underwent the centre-most crossing of the magnetic structure and would be expected to have observed the largest bipolar signature.

Instead of the expected bipolar signature, C3 observed a series of peaks in magnetic field strength and temperature and a corresponding set of dips is seen in density and DEF. This can be explained as a drop-out of the CPS plasma at the spacecraft location. Within these drop-outs, the observations are consistent with the PSBL, as indicated by a high magnetic field strength, low density and temperature and drop-outs of the perpendicular electron DEF. This situation is caused by X-lines; once all of the CPS field lines are reconnected, the lower density PSBL field lines are reconnected next; this would cause a spacecraft to observe a CPS-like density followed by a PSBL-like density (this would be expected to occur in both modes of reconnection). The occurrence of reconnection is evident through the observation of parallel and anti-parallel streaming electrons seen at all spacecraft. The rotation of the ion pitch angles at the second drop-out may indicate that reconnection is occurring during the observation; since active X-lines expel plasma away from them on both sides, a spacecraft passing

an active X-line would detect a reversal in the pitch angle of the particles which is observed. The first drop-out is also close to a rotation in pitch angle although this is thought to be due to the change in direction of the magnetic field; the first drop-out is hence due to an X-line that is no longer active (dormant X-line).

Estimates of the expected encounter time of C3 return a result of 04:42:01 UT, which coincides with the boundary between the first drop-out in the CPS (dormant X-line) and the C3 magnetic minimum. Both models predict a structure with CPS-like plasma, therefore CPS-like plasma of the C3 magnetic minimum is assumed to be the PO region of the magnetic structure. Figure 25 shows a diagram of the magnetic structure, plasma sheet and trajectories of the spacecraft deduced from the data. The observations and the predictions of the two modes of reconnection are now compared.

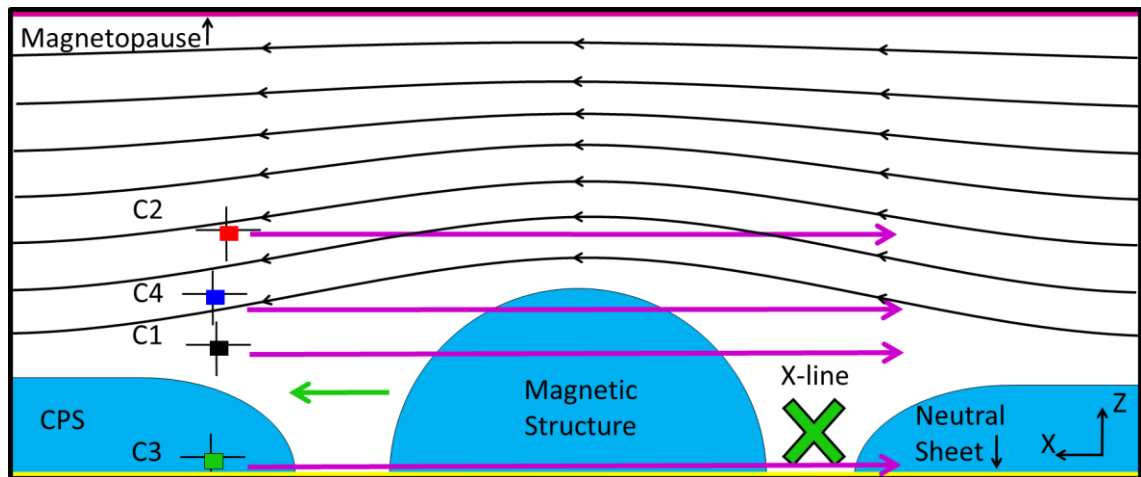


Figure 25: Diagram of magnetic structure, plasma sheet and spacecraft trajectories deduced from the data. C2 passes outside of the structure, C1 and C4 pass through the structure and C3 observes two plasma sheet drop-outs and an X-line.

2.6.2 Multiple-X-line Reconnection Interpretation

A model of a flux rope which contains CPS-like plasma is able to readily explain the TCR signature seen at C2 and the bipolar signatures and plasma appearance at C1 and C4. However a flux rope, identifiable by a symmetrical bipolar signature with a symmetrical plasma distribution, is not seen in the C3 data. A possible explanation for this could be that the flux rope is early in its development cycle and does not yet have the structure that can be recognised as an observation of a quasi-force free flux rope. However, further consideration needs to be given to how such an ‘early’ flux rope would drive well developed signatures at the other spacecraft. Alternately, situations where X-lines are not parallel or are of greatly unequal lengths or do not have uniform reconnection rates along their length, may produce flux ropes with unusual edge effects, such that signatures matching the above description may not be observed at each of the four spacecraft in this case.

In MXR, if two X-lines have reconnected all of the CPS field lines and they begin reconnecting PSBL field lines, this leads to a situation of a CPS with two regions of PSBL-like plasma, between which is a region of CPS-like plasma; this is consistent with the C3 observations. The TCR is caused by the increase in the pressure of the plasma between the X-lines due to the plasma outflow from the X-lines. The pressure of the different regions of the tail, in the direction perpendicular to the current sheet, must be balanced; if the pressure of the plasma between the X-lines increases, the region will expand to reduce its pressure and to re-establish pressure balance; hence this expansion causes the compression in the lobe and hence the TCR observed at C2. In addition, MXR leads to one TCR from two X-lines which is also consistent with the observations.

2.6.3 Time Dependent Reconnection Interpretation

A model of a flux bulge which contains plasma-sheet-like plasma is able to readily explain the TCR signature seen at C2 and the bipolar signatures and plasma appearance at C1 and C4. However the observations do not exhibit the predicted asymmetric bipolar signature with a CPS-like plasma density occurring concurrently with the positive excursion. To create the two drop-outs in the plasma sheet downstream from a single X-line, the reconnection rate would have to vary causing two bursts of reconnection. If the X-line had reconnected all of the CPS field lines, it would begin reconnecting PSBL field lines. If reconnection then slowed or ceased and then increased again at the same location, there would be no CPS field lines left and hence one would not expect to observe a CPS-like density between the two drop-outs seen in the observations.

2.7 Conclusions

Multi-point observations of a TCR and the magnetic structure causing it have been presented, using data from the four Cluster spacecraft which each encounter the structure with different impact parameters. The estimated velocity of the structure, calculated from the timing of distinct signatures, is $(99, 154, -31) |186| \text{ km s}^{-1}$ in GSM. The structure has an estimated size of $\sim 1.19 R_E$ measured in the direction of travel and a size between of 1.94 and $2.86 R_E$ measured in the direction perpendicular to the current sheet, assuming it is symmetrical about the current sheet. C2 passed outside of the structure and observed a TCR. C1 and C4 passed through the structure at high impact parameters and C3 passed through the centre. C3 observed a region of CPS-like plasma between two plasma sheet drop-outs (the former is thought to be the PO region of the structure).

The plasma sheet drop-outs are due to the passage of two X-lines passed the spacecraft locations; concurrent with the second drop-out, the spacecraft observes a rotation in the pitch angle of the ions from 0° to 180° which is consistent with the expected signature of a reconnecting X-line. The occurrence of magnetic reconnection is also indicated by the observation of parallel/anti parallel electron fluxes. The TCR is caused by the increase in pressure and expansion of the plasma between the X-lines in the direction perpendicular to the current sheet. Although the observations do not fit in their entirety with the predictions of either the flux rope or the flux bulge models, the observation of two plasma sheet drop-outs (interpreted as X-lines, one active, one dormant) with CPS-like plasma

between them and only one TCR is evidence in favour of the multiple X-line reconnection model.

Chapter 3

Modelling the Effects of Time-Varying Reconnection Leading to the Formation of Travelling Compression Regions in the Magnetotail

3.1 Introduction

As discussed in previous chapters, TCRs (Slavin et al., 1984, 2003c) are moving compressions in the lobe caused by a magnetic structure passing below. The magnetic structure is created by magnetic reconnection; magnetic reconnection occurs in the magnetotail at the Near Earth Neutral Line (NENL) and at the Distant Neutral Line (DNL). Reconnection is thought to occur through one of two modes. The first is multiple-X-line reconnection (e.g. Lee and Fu, 1985); in this model, magnetic helices containing plasma known as flux ropes (Elphic et al., 1986; Slavin et al., 2003a) form between multiple X-lines.

The second mode is Time-Dependent Reconnection (TDR); this involves a time-varying reconnection rate controlled by a time-varying reconnection electric field and can occur at a single X-line. As detailed in Chapter 1, TDR has been modeled in using both MHD and single particle physics; the details of both models are compared below.

3.1.1 **Comparison of the two existing models**

The differences between the structures created by the two TDR models discussed in depth in Chapter 1 are now briefly stated. The MHD model of TDR (Semenov et al., 1983a, 1984; Biernat et al., 1987) results in a structure called a flux bulge which contains a tear-drop shaped PO region. The model assumes the structure is thin (perpendicular to the current sheet) and that within the PO region, the magnetic field is directed solely in Z . The lobe field above the PO region is displaced causing a compression in the lobe and hence a TCR. The TCR generated by the flux bulge in this model has a bipolar signature which has a leading excursion which is smaller in duration and magnitude than the trailing excursion. With increasing distance above the current sheet, the magnitude of the magnetic signature decreases in absolute terms. With increasing Z , the relative difference between the two excursions increases in B_Z but decreases in B_X . The structure evolves with time; with increasing time (which is analogous to increasing distance of the structure away from the X-line), the structure grows in Z and the magnitude of the signature in B_X and B_Z increases. With increasing time, the relative difference between the excursions decreases for B_Z but increases for B_X .

The cold particle model of TDR (O&C87) tracks the position and velocity of the individual particles. The model does not assume the field within the PO region is perpendicular to the current sheet and hence has a component of the magnetic field in X. The inflow and outflow of the plasma in this model is cold, there are no changes in pressure perpendicular to the current sheet as a result of reconnection, no expansion of the PO region and hence no TCR is generated with this model.

Thus, there are both significant differences and limitations to each of the above models in representing the observed structure of the tail during reconnection. The goal of this study is to understand and reconcile these differences and to provide an improved model of this process in the magnetotail. As the model will build substantially on the model of O&C87, Section 3.2 reviews in more detail the relevant aspects of that model, before describing the adaptations to it in Section 3.3. Section 3.4 presents representative results from this model and discusses these in detail in Section 3.5. Section 3.6 presents our overall conclusions.

3.2 Cold Particle Model of Time-Dependent Reconnection

3.2.1 Marginal Firehose Stability Equation

The cold particle model described in Chapter 1 is based on the principle of stress balance on a reconnected field line, which was originally derived by

Rich et al. (1972). In the tail, parallel to the current sheet, the magnetic tension is balanced by either the pressure anisotropy or pressure gradients. In areas where the pressure gradients are small, the magnetic tension is balanced solely by the plasma pressure anisotropy; here stress balance requires that the plasma outside of the current sheet satisfies the Marginal Firehose Stability condition:

$$P_{\parallel} - P_{\perp} = \frac{B^2}{\mu_0} \quad (3.1)$$

where B is the magnetic field strength outside the current sheet and P_{\parallel} and P_{\perp} are the components of the plasma pressure tensor parallel and perpendicular to the magnetic field direction respectively. In the context of the magnetotail, where the major component to the field lies parallel to the current sheet, equation 3.1 represents the stress balance condition parallel to the current sheet (referred to as the horizontal stress balance). In the direction perpendicular to the current sheet the pressure balance (referred to as the vertical pressure balance) is:

$$\frac{B^2}{2\mu_0} + P_{\perp} = \text{Constant} \quad (3.2)$$

which expresses the conservation of total (magnetic plus thermal) pressure in that direction. Returning to the horizontal stress balance (equation 3.1), the plasma pressure in principle includes contributions from both dynamic ($P_{\text{RAM}} = nmV^2$) and thermal ($P_{\text{T}} = nkT$) terms and thus may more properly be represented by the stress tensor M . The frozen-in flux condition ensures that there is no net particle motion perpendicular to the magnetic field (except perhaps briefly when particles are interacting with an active X-line). Hence the perpendicular contribution to the dynamic pressure for particles

can be considered negligible. For this reason Cowley (1980) and Owen & Cowley (1987b) argued that the general stress balance conditions should be:

$$M_{\parallel} - P_{\perp} = \frac{B^2}{\mu_0} \quad (3.3)$$

O&C87 used this condition under the simplifying assumptions that the reconnected field wedge had only a small opening angle ($\cos \theta \sim 1$, referred to below as the small angle approximation) such that the magnetic field is directed mostly in X (as is the case in the tail), hence the parallel particle velocity and magnetic tension force are also assumed to be directed in X. They further assumed a cold particle population with no thermal pressure ($nkT = 0$). The parallel dynamic pressure is then caused only by the reversal of the X-component of velocity (and hence momentum) of the particles of mass flux $nmV_{\parallel in}$; the particles arrive with speed $V_{\parallel in}$, travel around the kink of the reconnected field line, and leave with speed $V_{\parallel out}$. The stress balance is hence a balance between the parallel dynamic plasma pressure and the magnetic tension.

The O&C87 model calculations are performed in the Field Line Rest Frame (FLRF) of the recoiling reconnected magnetic field. This is also known as the deHoffman-Teller frame (deHoffman and Teller, 1950), which is the frame in which the uniform electric field in the system is transformed away ($E^* = 0$). In this frame there is no $E \times B$ drift and the net particle guiding centre motion remains wholly field-aligned. In the absence of the electric field, there is no gain in energy of individual particles and their speed remains constant throughout their interaction with the field kink at the current sheet. Hence in this cold particle model, $V_{\parallel in}' = V_{\parallel out}' = V_o'$ (V' denotes a speed in the FLRF and V denotes a speed in Earth's Rest Frame).

Combining $P_{\perp} = 0$ with the stress balance equation 3.3 leads to the expression for stress balance in this model:

$$2n_{in}m(V_o')^2 = \frac{B^2}{\mu_o} \quad (3.4)$$

Rearranging equation 3.4 and introducing the Alfvèn velocity ($V_A^2 = \frac{B^2}{n_{in}m\mu_o}$) of the undisturbed field region, the velocity of the inflow and outflow particles in the FLRF becomes:

$$V_o' = \frac{V_A}{\sqrt{2}} \quad (3.5)$$

In order to maintain stress balance, the reconnected field lines must recoil from the X-line in such a way that, in the FLRF, the plasma enters and leaves the current sheet with the speed given by equation 3.5. Although the speed of the particles doesn't change (in the FLRF), the particles reverse direction as they travel around the kink of the hairpin-like reconnected field lines.

3.2.2 Frames of Reference

The relationship between the Field Line Rest Frame (FLRF) and Earth's Rest frame (ERF) can be determined by knowledge of the plasma flow on the field line in the ERF; this is illustrated in the diagram of velocity space in Figure 26. The figure shows the configuration in velocity space for a reconnected field line threading a 1-D current sheet and the associated particle motions. The ERF is marked with the velocity axes (V_x, V_z). The FLRF is marked with the velocity axes (V_x', V_z') and is shifted from the

ERF by a velocity V_F (the recoil speed of the field line) which is directed along the V_X axis.

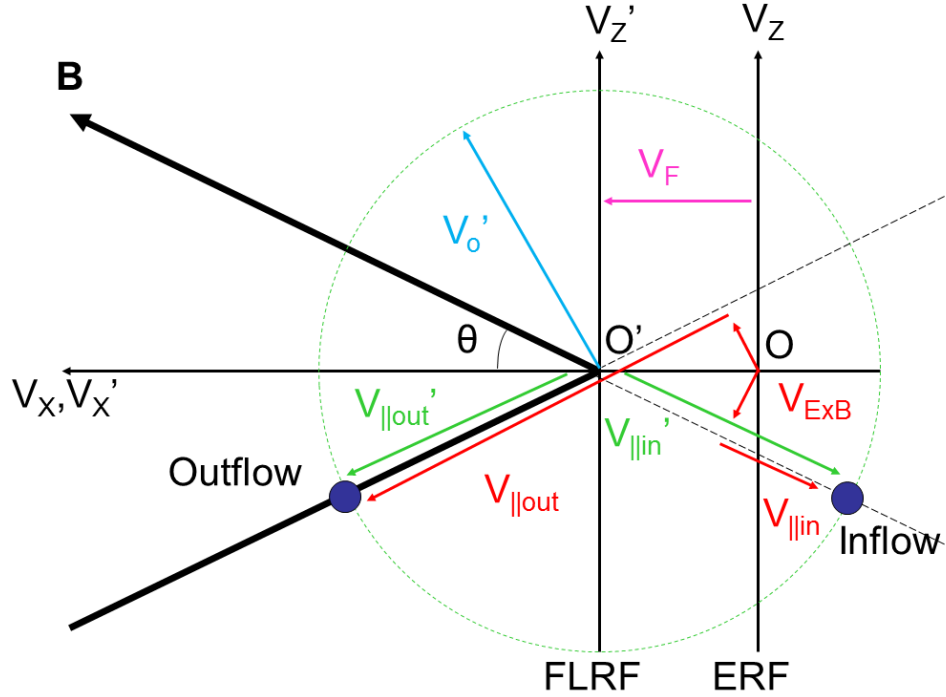


Figure 26: Diagram in velocity space of a particle (blue circle) travelling along the hairpin-like field line (thick black line marked ‘B’) in two different frames of reference. The ERF has velocity axes marked (V_X , V_Z) and the FLRF has axes marked ($V_{X'}$, $V_{Z'}$). The FLRF and the magnetic field line are both moving relative to the ERF at the field line velocity V_F (pink arrow). The direction of travel of the particles reverses and thus the inflow and outflow are on opposite sides of the FLRF Z' -axis. Both the inflow and outflow have speed V_o' in the FLRF and hence are both located on the dotted circle of radius of V_o' (blue arrow) which is centred at the origin of the FLRF. For the velocities in the ERF (in red), the particle inflow velocity consists of a field aligned velocity $V_{\parallel in}$ and an $E \times B$ drift at speed $V_{E \times B}$, (an analogous statement can be made for the outflow). Comparing the velocity in X in both frames of reference (assuming the small angle approximation is in effect), the diagram shows that $V_{\parallel in'} \approx V_{\parallel in} + V_F$ and $V_{\parallel out} \approx V_{\parallel out'} + V_F$.

The structure of the hairpin-like field line is represented by the solid dark line marked ‘B’, which for convenience of explanation has its apex at the origin O' of the FLRF. The positions in velocity space of the inflow and

outflow cold particle beams are represented by the blue circles. For a given magnetic field strength and external plasma density, the requirements for stress balance in the FLRF will determine the necessary inflow and outflow speed $V_{\parallel in}'$ and $V_{\parallel out}'$, represented by the green arrows. The direction of the magnetic field on the $-V_X'$ side of the plot (dotted lines) is extrapolated from the $+V_X'$ side and since the inflow particles are field-aligned, their position in velocity space must lie on these lines.

Since there is no change of speed of the particles during their field line kink in the FLRF, the inflow and outflow speed in the FLRF are equal. The velocity is expected to be reversed (in X about the Z' axis) upon traversing the hairpin-like field line, hence the outflow is expected on the opposite side of the Z' axis compared to the inflow. In this model, the outflow (like the inflow) remains field aligned and hence it must be on the thick black line marked 'B' (or the dotted line which is the extrapolation of the field line on the $-V_X'$ side of the plot); the branch it falls on depends on whether the particle is reflected or transmitted (the figure shows the former). As mentioned previously, the inflow and outflow speed in the FLRF are both V_o' , hence, in the figure both are located on the dotted blue circle of radius V_o' which is centered at O' (the origin of the FLRF).

The inflow and outflow velocity of the particles in the ERF (a frame in which the electric field is non-zero) is comprised of an $E \times B$ drift perpendicular to the field direction at speed $V_{E \times B}$ and a field aligned motion at speed $V_{\parallel in}$ and $V_{\parallel out}$ respectively, marked with red arrows. Knowledge of this field aligned speed, together with the requirements for stress balance (e.g. equation 3.5) allows us in this geometry to determine the value of V_F .

From the geometry of the figure, using the small angle approximation, it is evident that the relationships between the speeds are:

$$V'_{\parallel in} \approx V_{\parallel in} + V_F \quad (3.6)$$

$$V_{\parallel out} \approx V'_{\parallel out} + V_F \quad (3.7)$$

The incoming and outgoing velocities in the FLRF can be written in terms of the Alfvén velocity using equation 3.5:

$$V'_{\parallel in} = V'_{\parallel out} = V_o = \frac{1}{\sqrt{2}} V_A \quad (3.8)$$

By rearranging equation 3.6, the field line velocity can be found; by equating above equations through V_F , the particle outflow velocity in the ERF for the cold particle model can be found:

$$V_F \approx \frac{1}{\sqrt{2}} V_A - V_{\parallel in} \quad (3.9)$$

$$V_{\parallel out} \approx V'_{\parallel out} + V_F = V'_{\parallel in} + (V'_{\parallel in} - V_{\parallel in}) = 2V'_{\parallel in} - V_{\parallel in} \quad (3.10)$$

$$V_{\parallel out} \approx \frac{2}{\sqrt{2}} V_A - V_{\parallel in} = V_A \sqrt{2} - V_{\parallel in} \quad (3.11)$$

Note that V_A and $V_{\parallel in}$ are observable quantities for a spacecraft located outside the region of reconnected field lines.

3.2.3 Separatrix Height

In order to understand the implications of the stress balance conditions on the structure of the tail, it is necessary calculate the spatial extent taken up by the wedge of reconnected flux, in the direction perpendicular to the

current sheet, as a function of distance from the X-line. The structure of the field lines and separatrix are depicted in the top panel of Figure 27, which shows a cut through the reconnected field wedge in the X-Z plane.

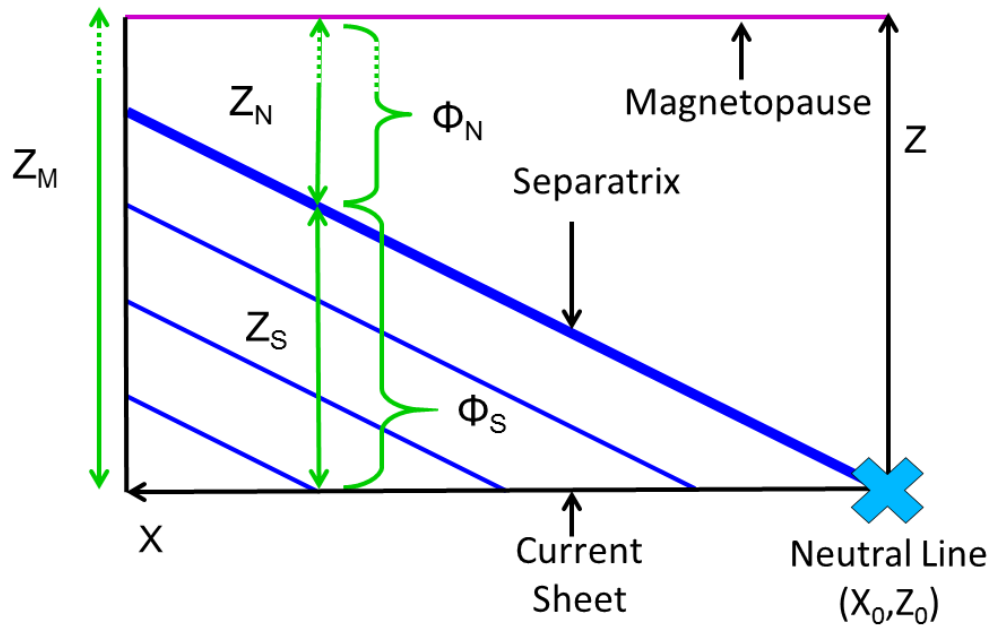


Figure 27: The structure of the reconnected field wedge in the cold particle model. The diagram contains reconnected field lines (thin blue lines), a separatrix (thick blue line) and an X-line (bottom right corner). The flux between a point on the current sheet and the separatrix (both at X) is equal to the total amount of flux reconnected since the field line at X left the X-line; this can be used to find Z_S .

The top and bottom boundary of the plot represent the magnetopause and the current sheet respectively. The X-line (which is at X_0, Z_0) is located in the bottom right corner of the plot. The thin blue lines represent reconnected field lines contracting in an Earthward direction (+X direction) away from the X-line. The separatrix is represented by the thick blue line and represents the field line currently being reconnected and thus maps directly back to the X-line position (or in the case of reconnection having ceased, the separatrix would be co-located with the most recently reconnected (outermost) field line as it recedes from the X-line). The

arbitrary location of an observer is defined as X , at which point the distance from the current sheet to the separatrix is Z_S and the amount flux along this distance as Φ_S , all of which is shown in Figure 27.

Above the separatrix, at distance X , is a region of non-reconnected flux between the separatrix and the magnetopause. The amount of flux in this region is defined as Φ_N and its vertical extent as Z_N . Across the northern tail lobe (from current sheet to magnetopause), the amount of flux is defined as Φ_M (not marked) and the vertical extent as Z_M .

Due to the conservation of magnetic flux, it is expected that the total magnetic flux (per unit length in Y), Φ_S , threading through the surface (along Z) between a point on the current sheet (X, Z_0) and a point on the separatrix at a height Z_S above (X, Z_0), is equal to the flux threading through the surface (along X) between the same point on the current sheet (X, Z_0) and a (different) point along the separatrix (X_0, Z_0 , at the X-line). This is also equal to the flux reconnected at the X-line in the time Δt since the field line currently threading the current sheet that is at X , was itself reconnected. Thus equating the values will allow us to calculate, Z_S . For a steady reconnection rate, associated with a constant electric field E_Y , the total (reconnected) flux through the current sheet between the X-line (at X_0) and X is:

$$\Phi_S\{X, t\} = B_Z(X - X_0) = E_Y \frac{(X - X_0)}{V_F} = E_Y \Delta t \quad (3.12)$$

where B_Z is the (constant) magnetic field threading the current sheet between the X-line and the observing point, E_Y is the electric field in Y that

is representative of the reconnection rate and V_F is the field line velocity consistent with stress balance. To clarify the use of different types of brackets, curly brackets denote dependence and curved brackets denote multiplication. For a time varying electric field $E_Y\{t\}$, the value of B_Z and thus Φ_S between X_0 and X will also be non-uniform and time dependent. Thus:

$$\Phi_S\{X,t\} = \int_{t_{F0}}^t E_Y\{t\}dt \quad (3.13)$$

where t is the current time and t_{F0} is the time the field line currently at X was reconnected which is:

$$t_{F0} = t - \frac{X-X_0}{V_F} \quad (3.14)$$

A similar consideration for the flux through the vertical surface between the current sheet and the separatrix at position X leads to:

$$\Phi_S\{X,t\} = B_X Z_S\{X,t\} \quad (3.15)$$

The above equation assumes B_X is constant in Z . Combining equations 3.13 and 3.15 leads to an equation for Z_S :

$$Z_S\{X,t\} = \frac{1}{B_X} \int_{t_{F0}}^t E_Y\{t\}dt \quad (3.16)$$

The distance Z_S can then be found for any position on the current sheet downstream from the neutral line at any time t , given that the time variation of the reconnection rate is known.

As the tail is expected to be in pressure balance perpendicular to the current sheet, the B_X profile in Z at any X is constant. Note also that an increased reconnection rate (E_Y) leads to an increase in Z_S at a given point and thus

an increase in the opening angle between the reconnected field wedge and the current sheet and an increase in B_z in this model.

3.2.4 **Height of PO boundary**

Using the information of the height of the separatrix, the height of the PO region can also be found. This region contains particles flowing away from the current sheet after participating in the balancing of the magnetic tension at the current sheet and is depicted in Figure 28 where it is represented by shaded red area, the red circles represent individual particles. The PO region is bounded by the surface termed the PO boundary (red dashed line); it cuts across the field lines and is a surface that connects the particles that have travelled the furthest along each field line. The distance from the current sheet to the PO boundary is defined as Z_p and the flux threading this region as Φ_p .

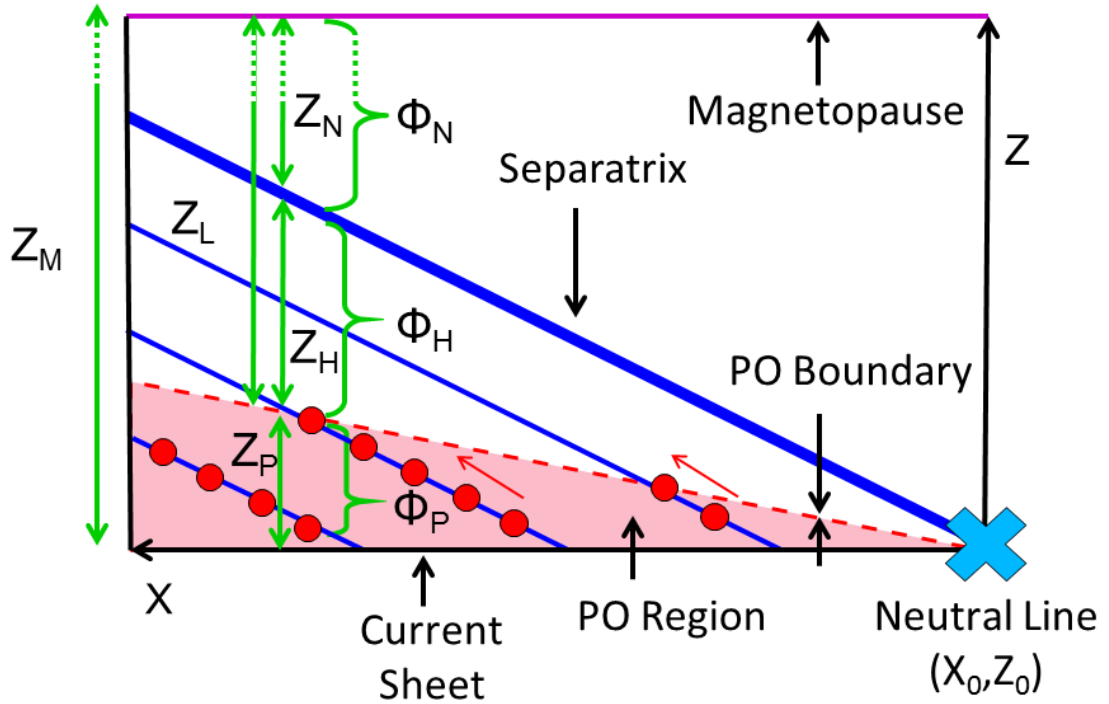


Figure 28: The structure of the reconnected field wedge in the cold particle model. The diagram shows the reconnected field lines and the PO region (the red shaded area) occupied by outflow particles (red circles) streaming away from the current sheet after pitch angle scattering (see text). The dashed red line bounding the region is called the PO boundary and its distance from the current sheet is Z_P . The distance between the PO boundary and the separatrix, Z_H , can be found from Φ_H , the amount of flux reconnected since the particle at the PO boundary (Z_P) at X left the X-line; the subtraction of Z_H from Z_S can be used to find Z_P .

Figure 28 shows that the region between the PO boundary and the separatrix contains reconnected flux but not outflow particles and hence has only inflow particles. The vertical extent of this region is defined as Z_H and the amount of flux as Φ_H .

The height of the PO boundary can again be found using the conservation of flux. It requires first finding the distance between the PO boundary and the separatrix Z_H ; in the time it took for a particle at the PO boundary to

have travelled from the X-line (at X_0) to X , a quantity Φ_H of flux is reconnected:

$$\Phi_H\{X,t\} = \int_{t_{P0}}^t E_Y\{t\}dt \quad (3.17)$$

where t_{P0} is the time at which that particle left the X-line which is:

$$t_{P0} = t - \frac{X-X_0}{V_{||out}} \quad (3.18)$$

This flux will lie between the particle in question and the separatrix and thus can be contained within the extent Z_H ; assuming B_X is constant in Z , this is equal to:

$$\Phi_H\{X,t\} = B_X Z_H\{X,t\} \quad (3.19)$$

Combining equations 3.17 and 3.19 leads to an equation for Z_H :

$$Z_H\{X,t\} = \frac{1}{B_X} \int_{t_{P0}}^t E_Y\{t\}dt \quad (3.20)$$

A comparison of Figure 27 and Figure 28 shows the relationship between Φ_S , Φ_P and Φ_H ; substituting equation 3.13 for Φ_S and 3.19 for Φ_H returns:

$$\Phi_P = \Phi_S - \Phi_H = \int_{t_{F0}}^t E_Y\{t\}dt - \int_{t_{P0}}^t E_Y\{t\}dt = \int_{t_{F0}}^{t_{P0}} E_Y\{t\}dt \quad (3.21)$$

Using the same method and equations 3.16 and 3.20 returns Z_P :

$$Z_P = Z_S - Z_H = \frac{1}{B_X} \int_{t_{F0}}^t E_Y\{t\}dt - \frac{1}{B_X} \int_{t_{P0}}^t E_Y\{t\}dt = \frac{1}{B_X} \int_{t_{F0}}^{t_{P0}} E_Y\{t\}dt \quad (3.22)$$

where t_{F0} is the time the field line at X was reconnected, t_{P0} is the time the particle at the PO boundary (Z_P) at X was accelerated at the X-line. Figure 28 thus shows that after reconnection has started, at some point downstream from the neutral line, X , the tail can be divided into 3 regions:

the PO region (vertical extent Z_P), the reconnected region which contains only inflow plasma (vertical extent Z_H) and the non-reconnected region (vertical extent Z_N). The latter two regions can be grouped together due their shared features, both contain lobe field with no outflow and hence are grouped together as the lobe. The lobe (vertical extent Z_L) extends from the PO boundary to the magnetopause. The sum of all of the regions is the distance from the current sheet to the magnetopause (which is the size of the northern tail); as shown in Figure 27 and Figure 28, the relationship of the size and flux of the regions and the northern tail is:

$$Z_M = Z_N + Z_H + Z_P = Z_L + Z_P \quad (3.23)$$

$$\Phi_M = \Phi_N + \Phi_H + \Phi_P = \Phi_L + \Phi_P \quad (3.24)$$

By rearranging the above, rewriting Φ_M in terms of magnetic field strength and using equation 3.21 the lobe flux lobe and size at X becomes:

$$\Phi_L = \Phi_M - \Phi_P = B_X Z_M - \int_{t_{F0}}^{t_{P0}} E_Y\{t\} dt \quad (3.25)$$

$$Z_L = Z_M - Z_P = Z_M - \frac{1}{B_X} \int_{t_{F0}}^{t_{P0}} E_Y\{t\} dt \quad (3.26)$$

where t_{F0} is the time the field line at X left the X-line and t_{p0} is the time the particle at the X left the X-line and B_X magnetic field strength of the lobe. The above are equations which allow the calculation of the size and flux of the lobe and PO region.

Note that a methodology has been set out, following the previous work of Owen and Cowley (1987a,b), for determining current sheet stress balance and its implication for the field and plasma structure of the reconnected field wedge downstream from an active neutral line, appropriate for a cold particle inflow and outflow around a 1-D current sheet. In the following sections, the effects and implications for the structure of the reconnecting plasma sheet are examined, under the condition that the cold particle approximation is relaxed somewhat.

3.3 A New Hot Particle Model of Time-Dependent Reconnection

3.3.1 Horizontal Stress balance

Having reviewed the algorithm used by O&C87, the cold single particle model is now modified. A feature not present in the cold particle model is the TCR; to cause the PO region to expand and compress the lobe, the model will be revised to allow the outflowing particles to carry some perpendicular plasma pressure. The addition of perpendicular plasma pressure is accomplished in the revised model by allowing pitch angle scattering of the field-aligned particles (endowing them with perpendicular velocity) as they cross the current sheet. Note that for simplicity, the particles are all assumed to be scattered by the same common pitch angle, α , but are spread uniformly in gyrophase, such that they form a single ring

distribution in velocity space. Note also that this provides a net perpendicular pressure, associated with the gyration motion with a common perpendicular velocity, but does not contribute, in itself, to a non-zero parallel pressure. Rather the effect of parallel inflow and outflow can be described in the parallel stress tensor, as in the cold particle case. The motion of particles in velocity space under this new set of assumptions is depicted in Figure 29.

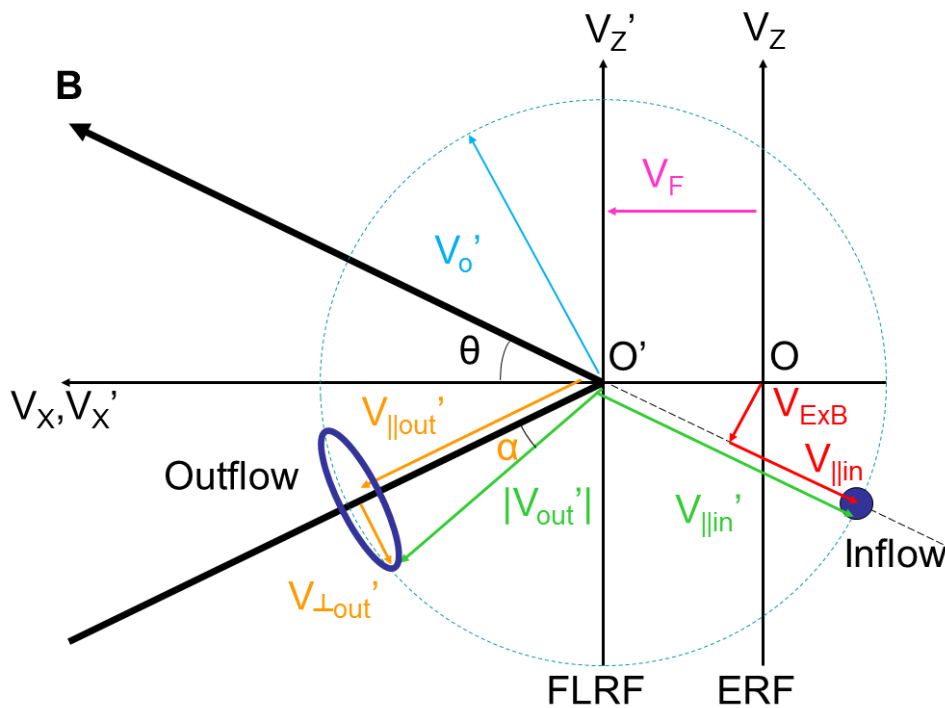


Figure 29: Diagram in velocity space of a particle travelling along the hairpin-like field line in two different frames of reference. The cold inflow field aligned particles (blue circle marked ‘inflow’) are travelling at $V_{\parallel in}'$ in the FLRF (as shown by the green arrow). The pitch angle scattering of the particles at the current sheet causes them to leave with both a parallel and perpendicular velocity component, $V_{\parallel out}'$ and $V_{\perp out}'$ respectively (orange arrows); although $V_{\parallel in}' > V_{\parallel out}'$, the total outflow speed $|V_{out}'|$ is unchanged and thus equal to $V_{\parallel in}'$. Note both the inflow speed and total outflow speed (green arrows) are both located on a sphere of radius V_0' and centred on the origin of the FLRF. However the outflow forms a ring distribution around the field direction (blue ring marked ‘outflow’). The distance in velocity space, V_F , between the two frames is then determined by the requirements of stress balance between the changes in particle momentum and the field tension (see text).

With reference to Figure 29, the inflow is represented as before by the blue circle marked ‘inflow’ to the right of the figure. In the ERF, the inflow velocity consists of 2 components, an $E \times B$ drift ($V_{E \times B}$) and a velocity parallel to the field ($V_{\parallel in}$), both represented by the red arrows in the figure. In the FLRF, the inflow is travelling at a speed of $V_{\parallel in}'$ along the field and is separated from the origin by the green arrow marked $V_{\parallel in}'$. Since the FLRF is defined as the frame in which the electric field is transformed away, the motion of particles in this frame involves no change in speed, hence the inflow and total outflow speeds are equal (and are represented in the figure by the green arrows).

As mentioned in Chapter 1, in the FLRF both the inflow and total outflow speeds are equal to V_o' (equation 3.5) and are thus located on the sphere represented in the (V_x, V_z) plane by the dotted circle of radius V_o' , centred on the origin of the FLRF axes. However due to the pitch angle scattering, the outflow particles now have velocity components both parallel and perpendicular to the magnetic field, $V_{\parallel out}'$ and $V_{\perp out}'$ respectively (represented by the orange arrows in Figure 29). As the particles have a speed of V_o' and are scattered by a pitch angle of α , the equation of the component velocities are:

$$V_{\parallel out}' = V_o' \cos \alpha \quad ; \quad V_{\perp out}' = V_o' \sin \alpha \quad (3.27)$$

Thus the outflow forms a ring on the surface of the sphere around the field direction as represented in the figure by the blue ring marked ‘outflow’. Note that all of the inflow velocity was in the parallel direction prior to scattering, but after scattering the velocity has components in the parallel and perpendicular directions such that $V_{\parallel in}' > V_{\parallel out}'$. The distance in

velocity space between the ERF and FLRF is such that it, combined with the inflow and outflow velocities (in the ERF), satisfy the stress balance condition in the FLRF.

As noted above, the scattering at the current sheet is assumed to result in outflow particles with a pitch angle of α . As the particles are initially field aligned, the final outgoing pitch angle is equal to the scattering angle and the two terms are interchangeable. The total dynamic (ram) pressure perpendicular to the field in the FLRF remains zero since the particles have no net perpendicular motion. However, the spread of the perpendicular speeds in a given direction associated with the particles in the ring distribution but at different gyrophase angles leads to an effective temperature, which in turn gives rise to the equivalent of a thermal pressure in that direction. This is given by:

$$P_{\perp} = \frac{1}{2} n_{out} m (V'_{\perp out})^2 \quad (3.28)$$

as derived in the appendix (section 6.2). Including perpendicular pressure into equation 3.3, the stress balance equation becomes:

$$M_{\parallel} - P_{\perp} = n_{in} m V'_{\parallel in}{}^2 + n_{out} m V'_{\parallel out}{}^2 - \frac{1}{2} n_{out} m V'_{\perp out}{}^2 = \frac{B^2}{\mu_0} \quad (3.29)$$

As before, the angle between the reconnected field line and the current sheet is assumed to be small and hence all of the terms of this stress balance equation can be considered for simplicity, to have components only in the X-direction. From the geometry shown in Figure 29, the inflow is field aligned (i.e. the inflow pitch angle is 0°), hence, in the FLRF, $V'_{\parallel in} = V_o'$. The velocity of the outflow is as stated in equation 3.27 and its substitution into equation 3.29 results in:

$$n_{in}mV_o'^2 + n_{out}mV_o'^2 \cos^2 \alpha - \frac{1}{2}n_{out}mV_o'^2 \sin^2 \alpha = \frac{B^2}{\mu_o} \quad (3.30)$$

The conservation of particle flux implies:

$$n_{in}V'_{\parallel in} = n_{out}V'_{\parallel out}$$

$$n_{in}V_o' = n_{out}V_o' \cos \alpha$$

$$n_{out} = \frac{n_{in}}{\cos \alpha} \quad (3.31)$$

The above shows the density of the outflow is greater than the inflow if $\alpha \neq 0^\circ$, this is due to the difference in field aligned speed between the inflow and outflow. To conserve the mass flux, the reduced field aligned outflow speed is offset by an increase in outflow density. Substituting for outflow density, equation 3.30 becomes:

$$n_{in}mV_o'^2 + \frac{n_{in}mV_o'^2 \cos^2 \alpha}{\cos \alpha} - \frac{1}{2} \frac{n_{in}mV_o'^2 \sin^2 \alpha}{\cos \alpha} = \frac{B^2}{\mu_o}$$

$$V_o'^2 \left[(1 + \cos \alpha) - \frac{1}{2} \frac{\sin^2 \alpha}{\cos \alpha} \right] = \frac{B^2}{n_{in}m\mu_o} = V_A^2 \quad (3.32)$$

here V_A is the Alfvén speed of the lobe. Rearranging (see appendix, section 6.3) the equation gives:

$$V_o' = V_A \left[\frac{2\cos \alpha}{(3\cos \alpha - 1)(\cos \alpha + 1)} \right]^{\frac{1}{2}} \quad (3.33)$$

As in the cold particle model, the recoil speed (in the ERF) of the reconnected field lines (V_F) and the ERF parallel outflow speed ($V_{\parallel out}$) of particles, can be determined using the geometry of Figure 29. The recoil speed of the reconnected field lines in the ERF, found by combining equations 3.6, 3.7, 3.27 and 3.33, is:

$$V_F \approx V'_{\parallel in} - V_{\parallel in} = V'_o - V_{\parallel in} = V_A \left[\frac{2\cos\alpha}{(3\cos\alpha-1)(\cos\alpha+1)} \right]^{\frac{1}{2}} - V_{\parallel in} \quad (3.34)$$

By combining equations 3.7 and equation 3.34, the ERF parallel outflow velocity is:

$$\begin{aligned} V_{\parallel out} &\approx V'_{\parallel out} + V_F = V'_{\parallel out} + (V'_{\parallel in} - V_{\parallel in}) \\ &\approx V'_o \cos\alpha + (V'_o - V_{\parallel in}) = V'_o (\cos\alpha + 1) - V_{\parallel in} \\ &\approx V_A \left[\frac{2\cos\alpha}{(3\cos\alpha-1)(\cos\alpha+1)} \right]^{\frac{1}{2}} (\cos\alpha + 1) - V_{\parallel in} \\ &\approx V_A \left[\frac{2\cos\alpha (\cos\alpha+1)}{(3\cos\alpha-1)} \right]^{\frac{1}{2}} - V_{\parallel in} \end{aligned} \quad (3.35)$$

where, $V_{\parallel in}$ is the velocity of any field aligned flow of the undisturbed inflow plasma measured in the ERF. If $\alpha = 0^\circ$, the cold solution is returned.

Figure 30 is a graphic representation of equation 3.33 and 3.34, showing the dependence on scattering pitch angle, α , of the values of V'_o , $V'_{\parallel out}$ and $V_{\perp out}$ required to achieve stress balance in our model current sheet. The plot contains two axes, one for FLRF pitch angle and one for ERF pitch angle. The latter can be found by comparing the outflow velocity in the ERF to the perpendicular velocity (which doesn't change between frames). The velocities are given in units of V_A , with V'_o , $V'_{\parallel out}$ and $V_{\perp out}$ represented by the red, green and blue lines respectively. The particles enter with a field aligned velocity of $V_{\parallel in}$ and speed V'_o , and after pitch angle scattering, leave with velocity components $V'_{\parallel out}$ and $V_{\perp out}$ with an unchanged speed of V'_o . Note that in the case of $\alpha = 0^\circ$, the result from the cold single particle model is recovered, $V'_o = \frac{V_A}{\sqrt{2}}$. In this 'hot' particle

model ($\alpha > 0^\circ$), as outflow pitch angle increases, a greater V_o' and $V_{\parallel in}'$ is needed to achieve stress balance. Conversely $V_{\parallel out}'$ reduces with increasing pitch angle up to $\sim 58^\circ$ in the FLRF and $\sim 32^\circ$ in the ERF, after which it increases. All three tend rapidly to infinity at $\sim 71^\circ$ in the FLRF and $\sim 36^\circ$ in the ERF and hence stress balance is not possible above this pitch angle for initially field aligned particles. As mentioned previously, the scattering angle is synonymous to the outflow pitch angle in this case as inflow particles are field aligned.

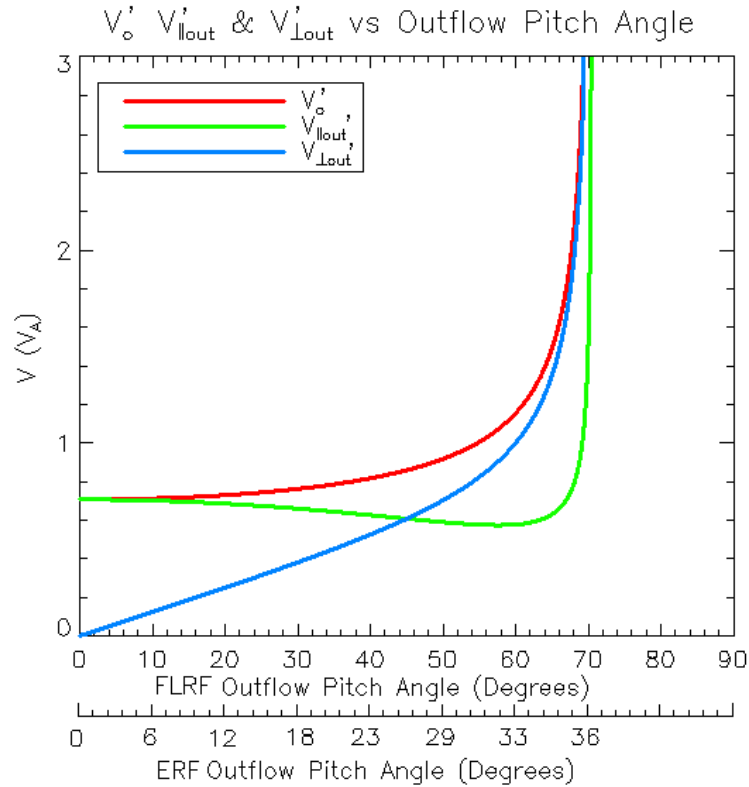


Figure 30: Plot showing pitch angle vs. velocity in the field line rest frame (in units of V_A). The velocities V_o' , $V_{\parallel out}'$ and $V_{\perp out}'$ are represented by the red, green and blue lines respectively. The particles enter with a field aligned velocity of $V_{\parallel in}'$ and speed V_o' and after pitch angle scattering, leave with velocity components $V_{\parallel out}'$ and $V_{\perp out}'$ and speed V_o' . With increasing pitch angle, the V_o' required for stress balance increases. Conversely $V_{\parallel out}'$ decreases until $\sim 58^\circ$ in the FLRF and $\sim 32^\circ$ in the ERF, after which it increases. All three tend to infinity at $\sim 71^\circ$ in the FLRF and $\sim 36^\circ$ in the ERF and hence stress balance is not possible above this pitch angle for initially field-aligned particles.

3.3.2 Vertical Pressure Balance

In addition to the modifications to V_F and to $V_{\parallel\text{out}}$, the new model also has consequences for the pressure balance conditions in the direction perpendicular to the current sheet. In this new model, reconnected field lines are occupied by both cold field-aligned inflow particles and outflow particles with a non-zero pitch angle. The former population has no effective perpendicular plasma pressure ($P_{\perp} = 0$) and makes no contribution to the total pressure balance with the exterior lobes. However, the outflow particles have gained an effective perpendicular plasma pressure ($P_{\perp} \neq 0$) due to the gyration component of motion gained through pitch angle scattering.

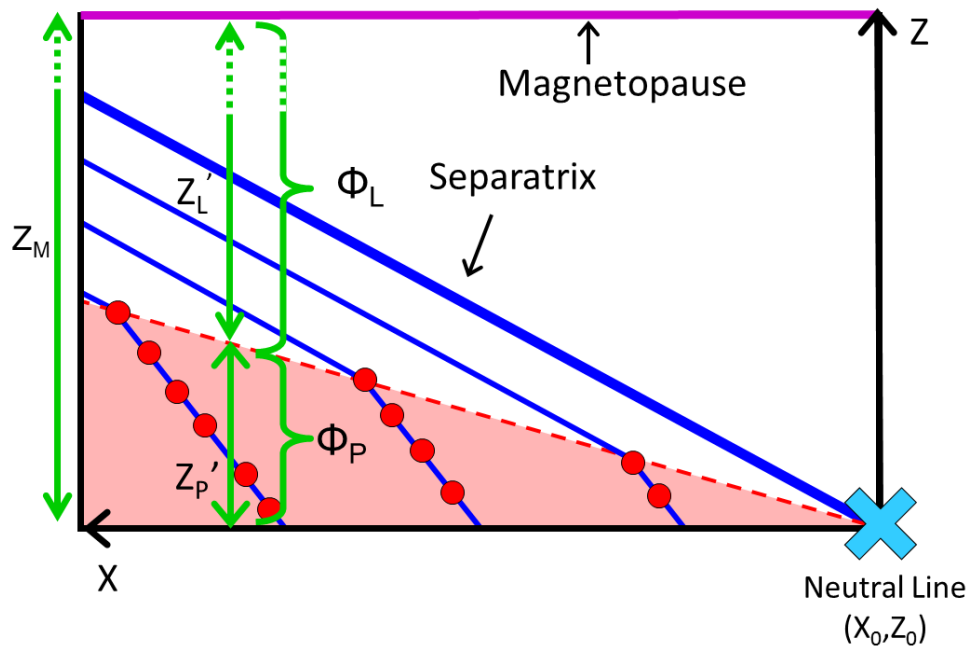


Figure 31: Schematic of the configuration of the field and plasma structures downstream from a neutral line resulting in the hot particle model, in a similar format to Figure 28. Prior to reconnection, the tail is in vertical pressure balance. However without reconfiguration, the addition of perpendicular plasma pressure to the outflow would mean the PO region has a greater total pressure than the lobe. To re-establish pressure balance the PO region (shaded pink) expands (from size Z_P to Z_P') and the lobe contracts (from Z_L to Z_L'). The expansion is expected to cause a kink in the field line at the PO boundary, however (see appendix, section 6.4) this is dynamically of little importance to the overall horizontal stress balance.

Figure 31 shows a schematic of the new configuration of field and plasma due to the presence of hot plasma at a given observation point (X) downstream from the neutral line; the figure is in the same format as Figure 28. Prior to reconnection, the tail (which is all lobe in this model) is in vertical pressure balance which only involves magnetic pressure; during and after reconnection, at X values where Z_p is non-zero, both the lobe and PO region have the same magnetic pressure but the PO region has a perpendicular plasma pressure in addition. Unless the configuration is now altered from that in the cold case, the PO region would have a greater total pressure than the lobe and thus vertical pressure balance would no longer be in effect. The way in which the distinct regions in the model must evolve in order to restore vertical pressure balance in the new model is now examined.

Assuming the magnetopause is a 'hard' and inflexible boundary (following the arguments of Slavin et al., 1994), any changes in the pressure or size of the lobe or PO region will not change the overall size of the northern tail Z_M . Re-establishing vertical pressure balance requires the expansion of the PO region (from Z_p to Z_p') and thus contraction of the lobe (from Z_L to Z_L'); this will decrease the pressure of the former and increase the pressure of the latter region such that they come back into vertical pressure balance (the primed values now refers to post expansion values and unprimed values refer to pre-expansion). As seen in Figure 31 the expansion is expected to cause a kink in the field line at the PO boundary, however (see appendix, section 6.4) this is dynamically of little importance to the overall horizontal stress balance.

The sizes of the contracted lobe and expanded PO region at any point downstream can be calculated from the principles of magnetic flux conservation used in the cold particle model and the assumption that the system maintains a total pressure balance perpendicular to the current sheet. The vertical pressure balance equation of the tail post expansion of the PO region is:

$$\frac{B_L'^2}{2\mu_0} = \frac{B_P'^2}{2\mu_0} + \frac{1}{2} n'_{out} m V_{\perp}^2 \quad (3.36)$$

where B_L' and B_P' are the post expansion magnetic field strength of the lobe and PO region respectively and n'_{out} is the post-expansion outflow density. The equations of the pre and post expansion outflow density (per unit X per unit Y) are:

$$n_{out} = \frac{N}{Z_P} ; \quad n'_{out} = \frac{N}{Z_P'} \quad (3.37)$$

where N is the number of particles per unit X per unit Y. The expansion does not change the number of particles in the PO region, by equating the two above equations through N, a relationship between the pre and post expansion outflow densities can be found:

$$n'_{out} Z_P' = n_{out} Z_P \quad ; \quad n'_{out} = \frac{Z_P}{Z_P'} n_{out} \quad (3.38)$$

Hence the relationship between the pre and post expansion pressure is:

$$P'_{\perp} = \frac{1}{2} n'_{out} m V_{\perp}^2{}_{out} = \frac{1}{2} \left(\frac{Z_P}{Z_P'} n_{out} \right) m V_{\perp}^2{}_{out} = \frac{Z_P}{Z_P'} P_{\perp} \quad (3.39)$$

The expansion of the PO region does not change the amount of magnetic flux it contains, nor the amount of magnetic flux in the lobe and hence

$\Phi_P' = \Phi_P$ and $\Phi_L' = \Phi_L$, the apostrophes have been dropped for these quantities. Rewriting equation 3.36 in terms of flux and pre expansion outflow pressure, the equation becomes:

$$\frac{\Phi_L^2}{Z_L'^2 2\mu_0} = \frac{\Phi_P^2}{Z_P'^2 2\mu_0} + \frac{Z_P}{Z_P'} P_{\perp} \quad (3.40)$$

Multiply the above by $Z_L'^2 Z_P'^2 2\mu_0$

$$\Phi_L^2 Z_P'^2 = \Phi_P^2 Z_L'^2 + Z_L'^2 Z_P Z_P' P_{\perp} 2\mu_0$$

$$0 = -\Phi_L^2 Z_P'^2 + \Phi_P^2 Z_L'^2 + Z_L'^2 Z_P Z_P' P_{\perp} 2\mu_0$$

Substitution of equation: $Z_L'^2 = (Z_M - Z_P')^2 = (Z_M^2 - 2Z_M Z_P' + Z_P'^2)$

$$0 = -\Phi_L^2 Z_P'^2 + \Phi_P^2 (Z_M^2 - 2Z_M Z_P' + Z_P'^2) + \dots$$

$$\dots (Z_M^2 - 2Z_M Z_P' + Z_P'^2) Z_P Z_P' P_{\perp} 2\mu_0$$

$$0 = -\Phi_L^2 Z_P'^2 + (\Phi_P^2 Z_M^2 - \Phi_P^2 2Z_M Z_P' + \Phi_P^2 Z_P'^2) + \dots$$

$$\dots (Z_M^2 Z_P Z_P' P_{\perp} 2\mu_0 - Z_M Z_P Z_P'^2 P_{\perp} 4\mu_0 + Z_P Z_P'^3 P_{\perp} 2\mu_0)$$

$$0 = (Z_P P_{\perp} 2\mu_0) Z_P'^3 + (\Phi_P^2 - \Phi_L^2 - Z_M Z_P P_{\perp} 4\mu_0) Z_P'^2 + \dots$$

$$\dots (Z_M^2 Z_P P_{\perp} 2\mu_0 - \Phi_P^2 2Z_M) Z_P' + \Phi_P^2 Z_M^2 \quad (3.41)$$

where Z_p (the pre expansion size of the PO region) can be found from equation 3.21, Φ_p and Φ_L from equations 3.21 and 3.25 respectively and P_\perp from the combination of equations, 3.27, 3.28, 3.31 and 3.33. The above is a cubic equation and is solved in the appendix (section 6.5); a value for Z_p is calculated for each value of X , given a specific profile for the reconnection rate and a specific value for the outflow pitch angle α .

3.3.3 Magnetic Signature

Having calculated the size of the flux bulge, the next step is to calculate the magnetic field components (B_x , B_z) in the model tail. The value of B_x in both the lobe and the PO region is calculated using the size and flux of the lobe and PO region given by equations 3.21, 3.22, 3.25 and 3.26. Calculating B_z requires Gauss' law for magnetism (equation 1.42) applied to this geometry:

$$\nabla \cdot B = \frac{dB_x}{dx} + \frac{dB_z}{dz} = 0 \quad (3.42)$$

$$\frac{dB_z}{dz} = -\frac{dB_x}{dx} \quad (3.43)$$

In combination with Gauss' law, calculating B_z requires a boundary condition, a location where the angle of the field is known; for the lobe, the magnetopause (at Z_M) is used; the magnetic field strength in Z at this point is defined as $B_{ZM} = 0$ (as the field here is horizontal). The integration of Gauss' law between the magnetopause and Z returns:

$$\int_{B_z}^{B_{ZM}} dB_z = - \int_Z^{Z_M} \frac{dB_x}{dx} dz \quad (3.44)$$

$$\text{Left Hand Side: } \int_{B_Z}^{B_{ZM}} dB_Z = [B_Z]_{B_Z}^{B_{ZM}} = B_{ZM} - B_Z \quad (3.45)$$

$$\text{Right Hand Side: } - \int_Z^{Z_M} \frac{dB_X}{dx} dz = - \frac{dB_X}{dx} [Z]_Z^{Z_M} = - \frac{dB_X}{dx} (Z_M - Z) \quad (3.46)$$

As the tail is in vertical pressure balance, both B_X and $\frac{dB_X}{dx}$ do not depend on Z (although they do depend on X and t). Substituting in the boundary condition at the magnetopause into the above reveals that B_Z is:

$$B_{ZM} - B_Z = - \frac{dB_X}{dx} (Z_M - Z) \quad (3.47)$$

$$B_Z\{X, Z, t\} = \frac{dB_X}{dx} \{X, t\} (Z_M - Z) \quad (3.48)$$

A similar procedure can be used for the finding the magnetic field strength in the PO region. The boundary conditions for this region are those at the current sheet (Z_0). The integration of Gauss' law between the observer and the current sheet returns:

$$\int_{B_{Z_0}}^{B_Z} dB_Z = - \int_{Z_0}^Z \frac{dB_X}{dx} dz \quad (3.49)$$

$$\text{Left Hand Side: } \int_{B_{Z_0}}^{B_Z} dB_Z = [B_Z]_{B_{Z_0}}^{B_Z} = B_Z - B_{Z_0} \quad (3.50)$$

$$\text{Right Hand Side: } - \int_{Z_0}^Z \frac{dB_X}{dx} dz = - \frac{dB_X}{dx} [Z]_{Z_0}^Z = - \frac{dB_X}{dx} (Z - Z_0) \quad (3.51)$$

Setting the current sheet position to $Z_0 = 0$, consistent with the assumed geometry returns:

$$B_Z - B_{Z_0} = - \frac{dB_X}{dx} Z \quad (3.52)$$

The second term on the left, B_Z at the current sheet (B_{Z0}) is fixed by the stress balance at the time of the reorientation of the field (caused by the electric field at the X-line):

$$B_{Z0} = E_Y \left\{ t - \frac{X-X_0}{V_F} \right\} \frac{1}{V_F} \quad (3.53)$$

where $E_Y \left\{ t - \frac{X-X_0}{V_F} \right\}$ is the electric field present at the X-line when the field line at X was reconnected. Thus the total B_Z in the PO region at a height Z above the current sheet is:

$$B_Z\{X, Z, t\} = -\frac{dB_X}{dx}\{X, t\}Z + E_Y \left\{ t - \frac{X-X_0}{V_F} \right\} \frac{1}{V_F} \quad (3.54)$$

3.4 Results

3.4.1 Model Specifications

The specifications of the model are now described. For simplicity, any pre-existing plasma sheet formed by processes other than that described here was omitted from the model. A condition of the stress balance equation is a location of negligible pressure gradient; as this is the case at the DNL and not at the NENL, reconnection in this model is assumed to occur at the DNL. Using values from O&C87, at the DNL, the density is 0.1 cm^{-3} and the velocity is 150 km s^{-1} . The DNL is placed at $X_{\text{GSM}} \sim -120 R_E$; as the study only involves the nightside of the magnetosphere, all mentioned positions in X_{GSM} refer to downtail position and hence the minus sign is neglected. At the DNL, the tail radius is $\sim 30 R_E$ (Slavin et al., 1983); the tail radius is used as the distance between the current sheet and the magnetopause, Z_M .

For simplicity only one species of particles was used in the model, the choice of species was based on the origin of the lobe plasma. Mantle plasma within the tail lobes originates from the magnetosheath (Rosenbauer. et al., 1975), which originates in the solar wind; solar wind plasma is mostly made up of protons and electrons. As protons have a larger effect on stress balance than electrons due to their larger mass, proton dynamics only are considered in the model. The profile of the reconnection electric field, $E_Y\{t\}$, is set to:

$$E_Y\{t\} = E_o \sin^2\left(\frac{\pi t}{t_R}\right) \quad \text{for } 0 < t < t_R \quad (3.55)$$

$$E_Y\{t\} = 0 \quad \text{otherwise}$$

This was chosen to allow a comparison with the results of Kiehas et al. (2009) who used the above parameters as it appropriately represents the pulse-like nature of the reconnection. The reconnection electric field is also the reconnection rate which hence has the same profile. The electric field maximum, E_o , is based on the value from Ivanova et al. (2009) who fitted an observed TCR with a TCR predicted from the MHD model of time dependent reconnection. They concluded that the flux bulge was created by a 180 second electric field pulse which peaked at $E_o = 1.1\text{mV/m}$.

3.4.2 **Outgoing velocity**

Having defined the setup values, the model was then run. It was used to plot the ERF outgoing velocity against FLRF pitch angle; this is shown in Figure 32. The plot shows that as the FLRF pitch angle increases, the ERF

outgoing velocity $V_{\parallel\text{out}}$ also increases and tends to infinity at $\alpha \sim 71^\circ$ as expected. Using the ERF outflow velocity and the perpendicular velocity (which is the same in both frames of reference), it is possible to calculate the pitch angle of a particle in the ERF. The ERF pitch angle is shown on a second axis below the FLRF pitch angle; the maximum ERF pitch angle is $\sim 36^\circ$. In the following plots, which illustrate the results of the model on the structure of the tail, the FLRF pitch angle used is 50° , this was chosen by trial and error to find the largest pitch angle that resulted in an expanded PO region which contained a magnetic field that remained consistent with the small angle approximation.

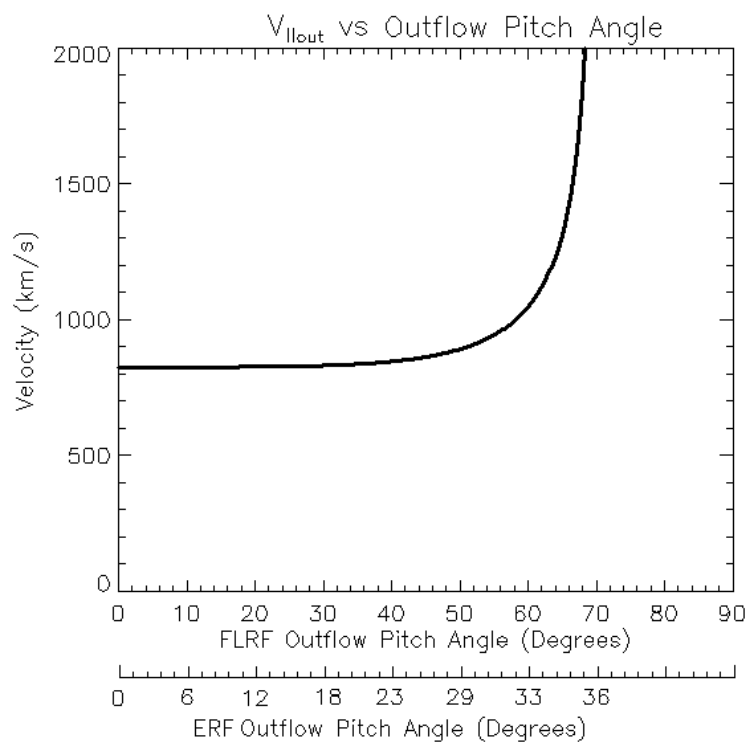


Figure 32: Diagram showing the ERF outgoing particle velocity vs. FLRF pitch angle and ERF pitch angle. The plot shows that as the pitch angle increases, the outgoing velocity also increases and tends to infinity at $\sim 71^\circ$ in the FLRF and $\sim 36^\circ$ in the ERF.

3.4.3 Structure of the tail

As mentioned previously, the ‘heating’ of the outflow plasma causes the PO region to expand. Figure 33 shows diagrams of the structure of the tail in both the cold and hot cases in the left and right panels respectively.

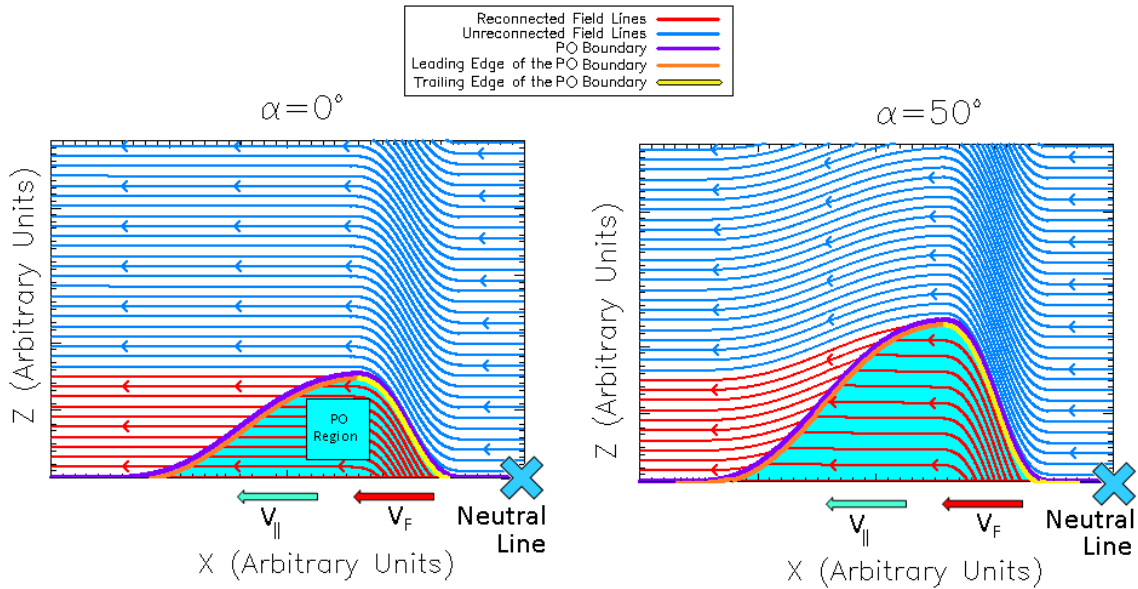


Figure 33: Diagrams showing the product of reconnection from the models described in this chapter. The panels show non-reconnected lobe field lines (blue), reconnected field lines (red) and the PO region (turquoise). The PO boundary (purple) can be divided into two surfaces named the leading (orange) and trailing (yellow) edges of the PO boundary. The left diagram shows the result of the cold particle model (c.f. O&C87) which has no expansion of the PO region; the right diagram shows the result of the hot particle model which has an expanded PO region and a compressed lobe (TCR). Note that in the hot particle model, the magnetic field strength of the PO region is smaller (field lines further apart) and the magnetic field strength of the lobe is greater (field lines closer together) than the equivalent in the cold particle model. Both plots show less magnetic flux after the passage of the flux bulge which removes flux from the tail. Unlike the MHD model, the PO region of this model has a magnetic field with a non-zero X component. Below the leading edge of the PO boundary, there is a very slight inclination to the field (i.e. $B_z > 0$).

In the diagrams, the lobe field lines are blue, the reconnected field lines are red, the PO region is shaded turquoise and the PO boundary is the purple

line. The key difference between the two diagrams is the expansion of PO region and the compression of the lobe, seen in the right plot, which is the result of the presence of hot plasma. In the hot particle model, the magnetic field strength and magnetic pressure of the lobe is greater (field lines closer together) and that of the PO region is lesser (field lines further apart) compared to the equivalent in the cold particle model. The compression of the lobe is consistent with the expectations of a TCR. Behind the PO region, less flux is present in both the hot and cold models, this is because the PO region carries flux away and contributes to the unloading of flux from the tail. As with the MHD model, the expanded PO region and the distorted field lines can be referred to as a ‘flux bulge’; unlike the MHD model, the field structure within the PO region has components in both the X and Z directions.

As shown in Figure 33, the surface which bounds the PO region is referred to as the PO boundary (purple boundary). This is split into two parts, the leading edge (orange boundary) is defined as the surface that cuts across the reconnected field; it links particles that have travelled the furthest on each field line. The trailing edge (yellow boundary) is defined as the part of the boundary below which, the reconnected field crosses the current sheet; the trailing edge of the PO boundary coincides with the outermost field line of the PO region. Below the leading edge of the PO boundary, there is a very slight inclination to the field.

In both the hot and cold models, the flux bulge is not at its maximum height as soon as reconnection ceases; the structure continues to grow in Z after reconnection ceases until the outflow particles reach the highest point in Z on the reconnected field lines. In this model, the electric field is non-

zero for t_R seconds; trial and error shows that the amount of time required for the structure to reach its maximum height is also $\sim t_R$ seconds. Figure 33 and the plots presented below are all t_R seconds after reconnection ceases to allow the structure to reach its maximum height in Z, unless stated otherwise.

Our model now provides a complete description of the field and plasma structure resulting from time-dependent reconnection within the tail. To obtain data on the structure, the model was run using the model specifications and an FLRF pitch angle of $\alpha = 50^\circ$. The pitch angle was chosen to be high enough to cause a noticeable lobe compression but not so high that it resulted in a violation of the small angle approximation ($\cos \theta \sim 1$); the largest angle of the field crossing the current sheet was $\sim 17.81^\circ$, this results in $\cos \theta \sim 0.95$. This returns a lobe compression ($\Delta B/B$ %) of 2.3%. The resulting outflow particle and field line velocities are 891 and 484 km s^{-1} respectively and the perpendicular velocity is 485 km s^{-1} ; after $2t_R$ the structure is $\sim 30 R_E$ in X.

3.4.4 Variations in the magnetic field signatures with height

In order to provide results which can be readily compared with observations, the structure and magnetic signature of the flux bulge resulting from the model is shown in Figure 34. Panel (a) illustrates the spatial structure of the tail in the X-Z plane (the model is invariant in the Y-direction) which has an expanded PO region and a compressed lobe. The X-line is located at $(X, Z) \sim (120, 0) R_E$ in the plot; note that the scale size of X is much larger than the scale size of Z. The other panels show the magnetic signature (B_X is in red, B_Z is in blue) vs. X for a range of sample heights: one just above the current sheet ($Z \sim 0 R_E$), a second through the PO region ($Z = 1 R_E$) and one through the lobe ($Z = 4 R_E$). The sample heights are marked in the tail diagram in the panel (a) by horizontal dark blue lines.

Outside of the structure panels (c) and (d) show a TCR is present, indicated by a bipolar B_Z and peak in B_X ; the bipolar signature has a positive trailing excursion which is larger in magnitude but smaller in X length compared to the negative leading excursion. The leading and trailing excursions are located above the leading and trailing edges of the PO boundary. Within the PO region, marked by the vertical blue lines in panels (b) and (c), the B_X plots show a peak across the structure; the magnitude of B_X in the PO region is less than that in the lobe. The plots also show a peak in B_Z below the trailing edge of the PO region.

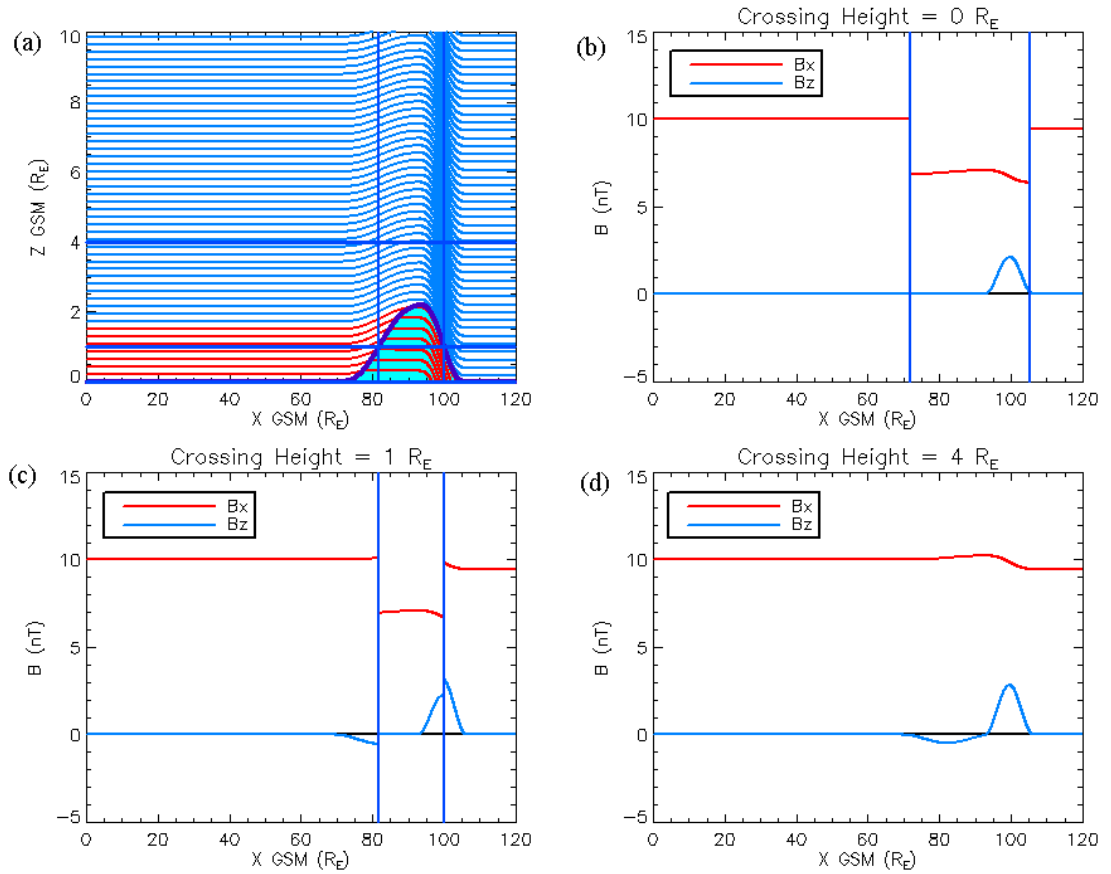


Figure 34: Diagram and magnetic signature of the model flux bulge. Panel (a) shows a diagram of the structure of the tail downstream from an X-line (located at $X = 120 R_E$). The dark blue horizontal line marks the sample heights ($Z = 0, 1, 4 R_E$). Panels (b), (c) and (d) show the magnetic signature of a flux bulge measured by virtual spacecraft at $Z = 0, 1, 4 R_E$ respectively; the panels show B_X (red) and B_Z (blue) vs. X distance. Within the PO region, marked by the vertical blue lines in panels (b) and (c), the B_X trace shows a peak across the structure and the B_Z trace peaks below the trailing edge of the PO region; the magnitude of B_X within the PO region is less than that in the lobe. Outside of the structure, panels (c) and (d) show a TCR; the bipolar signature has a trailing excursion which has a larger magnitude but is smaller in X length compared to the leading excursion.

Figure 35 shows a plot comparing two lobe crossings ($Z = 4, 14 R_E$), at different distances from the current sheet. In the $Z = 4 R_E$ plot, B_X is in red and B_Z is in blue, in the $Z = 14 R_E$ plot, B_X is the purple cross and B_Z is the purple line. The plot shows that the B_X profile is the same at both distances from the current sheet in the lobe. The plot also shows that the B_Z bipolar signature reduces in magnitude with distance from the current sheet however the size of the leading excursion relative to the trailing excursion doesn't change.

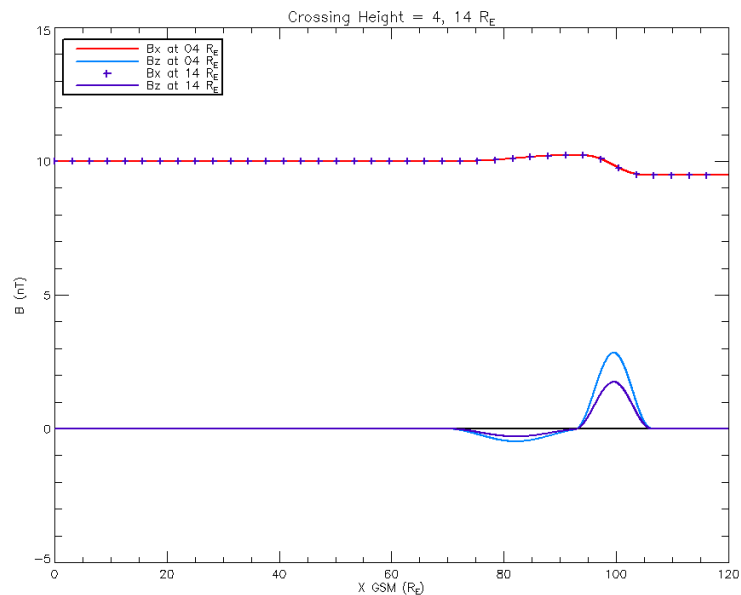


Figure 35: Comparison of the TCR at $Z = 4, 14 R_E$. In the $Z = 4 R_E$ plot, B_X is in red and B_Z is in blue, in the $Z = 14 R_E$, B_X is the purple cross and B_Z is the purple line. The plot shows that the B_X profile is the same at both distances from the current sheet in the lobe. The plot also shows that the B_Z bipolar signature reduces in magnitude with distance from the current sheet however the size of the leading excursions relative to the trailing excursion does not change.

3.4.5 Lobe Compression

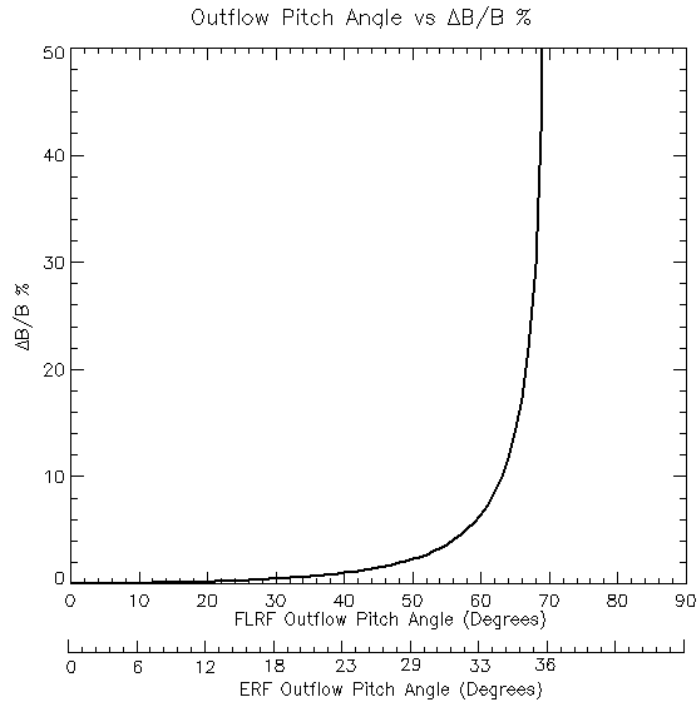


Figure 36: Diagram of pitch angle vs. $\Delta B/B$ % where $\Delta B/B$ % is the maximum percentage change (across all X values) in the magnetic field strength of the lobe due to compression. The plot shows $\Delta B/B$ % increases with pitch angle and is asymptotic at $\sim 71^\circ$ in the FLRF and $\sim 36^\circ$ in the ERF.

One of the factors controlling the reduction in the size of the lobe is the outgoing FLRF pitch angle; for a given inflow velocity, a greater pitch angle leads to a greater outflow perpendicular plasma pressure, a greater expansion of the PO region and hence a smaller lobe. Figure 36 shows the relationship (from the model) between the compression of the lobe and the pitch angle. The compression of the lobe is represented by the percentage increase of lobe B_x between the unexpanded and the expanded cases; for each pitch angle, this value is the largest compression of all X values at $1t_R$ seconds after reconnection ceases, at which time, the structure reaches its maximum size in Z and does not change afterwards. The plot has the same

general form as V_{\perp} vs. pitch angle in Figure 30, in that it increases with pitch angle and is asymptotic at $\sim 71^{\circ}$ in the FLRF and $\sim 36^{\circ}$ in the ERF.

The extent of the expansion of the PO region, in the direction perpendicular to the current sheet, depends on the size of the unexpanded PO region. To analyse this, values were taken from different X positions of the flux bulge. From left to right, Table 1 shows the Z size of the PO region in R_E before expansion (Z), after expansion (Z'), the difference between the two (Z' - Z), the percentage change, B_X in the PO region in nT after expansion, B_X in the lobe in nT after expansion and the percentage change of B in the lobe due to expansion. The values are arranged (in X) from the leading end of the structure (top of the table) to the trailing end (bottom of the table); the top four values are of the leading edge, the middle value is at the largest size of the unexpanded PO region and the bottom four values are of the trailing edge.

The table shows that at greater unexpanded sizes, the difference in size due to expansion is greater, the percentage increase is smaller and B_X in the PO region after expansion is greater. The table shows a greater expansion of the trailing edge compared to the leading edge, this can be explained by the smaller amount of flux and hence magnetic pressure above the trailing edge (only unreconnected flux) compared to the leading edge (unreconnected flux and reconnected flux without outflow). The flux bulge removes flux from the tail leading to a reduced B_X which explains the negative $\Delta B/B$ % values at the trailing edge.

Z (R _E)	Z' (R _E)	Z'-Z (R _E)	Percentage Increase	B _X (nT) POR	B _X (nT) Lobe	ΔB/B % Lobe
0.50	0.72	0.22	44.14	6.94	10.08	0.75
1.00	1.43	0.43	42.72	7.01	10.15	1.5
1.50	2.12	0.62	41.34	7.07	10.22	2.22
1.55	2.19	0.64	41.21	7.08	10.23	2.3
1.50	2.12	0.63	41.68	7.06	10.2	2.05
1.00	1.46	0.46	46.28	6.84	9.97	-0.33
0.50	0.76	0.26	51.23	6.61	9.73	-2.73

Table 1: Table showing (from left to right) the Z size of the PO region in RE before expansion (Z), after expansion (Z'), the difference between the two (Z'-Z), the percentage change, B_X in the PO region in nT after expansion, B_X in the lobe in nT after expansion and the percentage change of B in the lobe. The top four values are of the leading edge to, the middle value is at the largest size of the unexpanded PO region and the bottom four values are of the trailing edge. The table shows that at greater unexpanded sizes, the difference in size due to expansion is greater however the percentage difference is less.

3.4.6 Evolution with time after reconnection ceases

The evolution of the flux bulge as it moves away from the X-line after reconnection ceases is shown in Figure 37. The left column of panels show the structure and magnetic signatures 1t_R seconds after reconnection ceases; the right column of panels show the structure 2t_R seconds after reconnection ceases. For both plots the reconnection rate is non-zero from 0 to t_R seconds. The middle and bottom rows of panels show the magnetic field components (B_X in red, B_Z in blue) of a PO region sample (at Z = 1 R_E) and a lobe sample (at Z = 4 R_E).

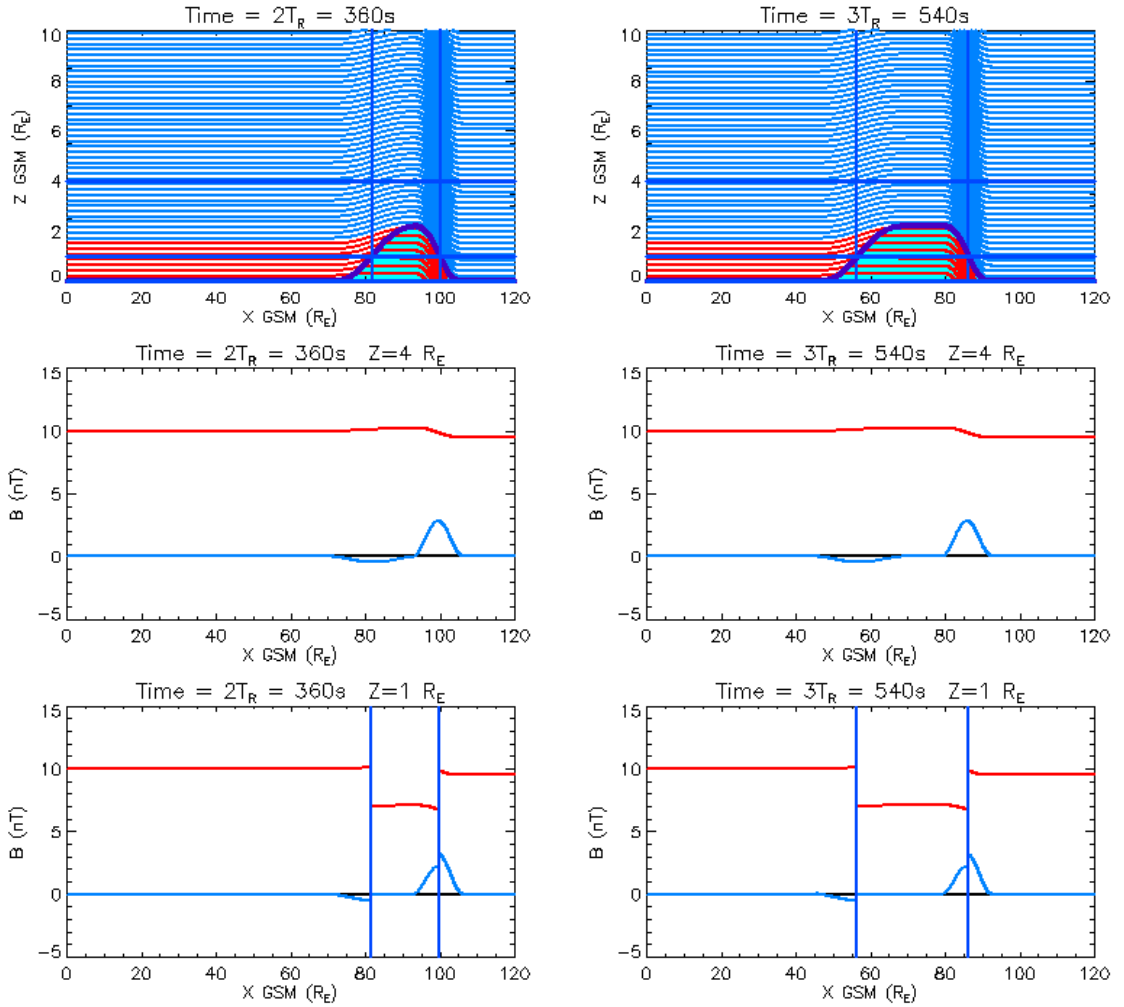


Figure 37 Diagram showing the effect of the passage of time after reconnection ceases. In all plots the reconnection rate is non-zero from 0 to $1t_R$ seconds. The left column and right column of plots show the structure and magnetic signatures $1t_R$ and $2t_R$ seconds after reconnection ceases respectively. The middle and bottom rows of panels show the magnetic field components (B_x in red, B_z in blue) of a PO region crossing (at $Z = 1 R_E$) and a lobe crossing (at $Z = 4 R_E$) respectively. The middle left plot shows a bipolar signature in B_z , the middle right plot shows that later in time the magnetic excursions are spatially separated ($B_z = 0$ between the excursions). Note that the excursions of the bipolar signature separate as time passes and once enough time has passed, the signature may become unrecognisable as a TCR.

The middle left plot shows a bipolar signature in B_z , the middle right plot shows that later in time the magnetic excursions are spatially separated ($B_z = 0$ between the excursions). The passage of time causes the PO region to expand in X . Thus the magnetic signature broadens and the two

excursions of the TCR bipolar signature (which coincide with the leading and trailing edges of the PO boundary) separate in time; the B_X increase and B_X decrease (which also coincide with the leading and trailing edges respectively) also separate. Once enough time has passed after reconnection ceases (and the flux bulge gets far enough away from the X-line), this result suggests the signature may become unrecognisable as a classic TCR signature.

Previous plots (e.g. Figure 37) show instantaneous snapshots of the plasma bulge in space. However, a real spacecraft detects time variation at an approximately fixed location, Figure 38 thus shows the model results variation against time; it simulates the observations a spacecraft would make at 4 distinct locations. In the top and bottom rows of plots, the virtual spacecraft are at $Z = 4, 1 R_E$ respectively. In the left and right columns of plots, the spacecraft are at $X = 75, 55 R_E$ respectively (note, the X-line is at $120 R_E$). The B_X and B_Z traces are similar to the spatial variation shown in Figure 37 except that the duration of the leading and trailing excursions of the bipolar signature in the lobe are now the same whereas in Figure 37 the durations were not the same.

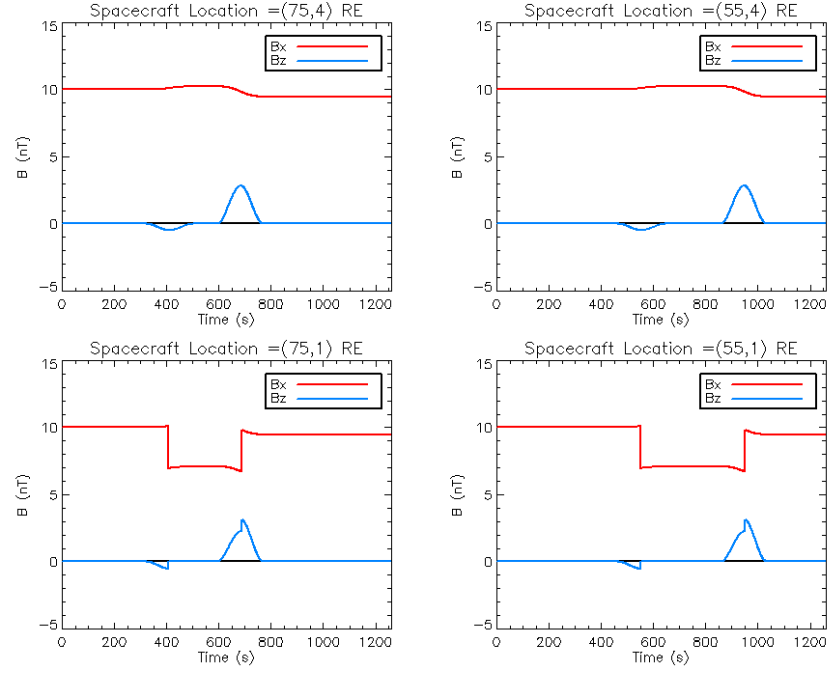


Figure 38: Plot showing the magnetic signature against time observed by four stationary virtual spacecraft. In the top and bottom rows of plots, the virtual spacecraft are at $Z = 4, 1 R_E$ respectively. In all plots, the electric field is non-zero for t_R seconds. In the left and right columns of plots, the spacecraft are at $X = 75, 55 R_E$ respectively (where the X-line is at $120 R_E$). The B_X and B_Z traces are similar to the spatial variation in Figure 37 except that the duration of the leading and trailing excursions of the bipolar signature in the lobe are now the same.

3.5 Discussion

Time dependent reconnection has been previously described by two types of models, both of which have different features and produce different magnetic structures. In the cold particle model, individual particles interact with the field line kink which is centred on the current sheet and the PO region contains a magnetic field that has components in both the X and Z directions. In the MHD model, the PO region expands causing a compression of the lobe and a TCR. The aim of this chapter is to reconcile the models. The new model is based on the methodology of the cold particle model, but the outflow is ‘heated’ through the inclusion of a simple

pitch angle scattering of particles as they cross the current sheet which gives the outflow a perpendicular pressure. This results in a PO region with a greater pressure than the lobe. To re-establish pressure balance the PO region expands and the lobe compresses leading to a TCR (the feature seen in the MHD model).

Creating the hot particle model requires modifying the stress balance equation transverse to the current sheet to account for an outflow with a non-zero pitch angle. The model shows that at greater outflow pitch angles and hence greater perpendicular velocities, a greater FLRF inflow velocity is required to maintain stress balance. Other effects of a greater pitch angle include a lower FLRF outflow velocity, this reaches a minimum at FLRF $\alpha \sim 58^\circ$ (ERF $\alpha \sim 32^\circ$). With increasing pitch angle above FLRF $\alpha = 58^\circ$, the FLRF inflow, FLRF outflow and perpendicular velocity all increase rapidly and tend to infinity at FLRF $\alpha \sim 71^\circ$ (ERF $\alpha \sim 36^\circ$). This implies a limit to the proportion of the magnetic energy (released by reconnection) that can be converted to thermal energy.

The flux bulge resulting from this model causes a TCR in the lobe. The magnetic signature of the TCR includes a peak in B_X and a bipolar signature in B_Z , the latter has a leading excursion which is smaller in magnitude but larger in X size than the trailing excursion. Within the PO region, B_X peaks across the region and B_Z peaks below the trailing edge of the PO region.

The PO boundary is inclined (at an angle to the current sheet) at the leading and trailing edges. The leading edge of the PO boundary is a surface comprised of the outflow particles that have travelled the furthest along each reconnected field line. Due to the different heights of the field lines, the furthest particle on each field line will have a different value of Z . As the field lines are not reconnected at the same time, the acceleration of the first particle on each field line occurs at different times and hence the furthest particle on each field line will all have the different X values. Hence the combination of the different X and Z values of the furthest particle on each field line leads to the line connecting the furthest particles (the leading edge of the PO region) being inclined and cutting across the mostly horizontal reconnected field. All of the particles and hence the entire leading edge, travels at $V_{\parallel\text{out}}$. The X distance between the furthest particle on the first and last reconnected field line is also the distance between the furthest particle on the first reconnected field line and the X -line at the moment reconnection ceased, which is $X = V_{\parallel\text{out}}t_R$, this is also the X -width of the leading edge.

The trailing edge of the PO boundary is the part of the PO boundary below which the field crosses the current sheet; reconnection has reoriented the magnetic field (which was initially horizontal) which gives the magnetic field (in the PO region) an inclination. As the trailing edge coincides with the outermost field line of the PO region, it and the adjacent lobe field are also inclined. The size of the trailing edge in X depends on the duration of reconnection. The distance between the first and last reconnected field line (which is also the distance the first field line travelled away from the X -line at the moment reconnection ceased) is $X = V_{FtR}$; reconnected field lines

cross the current sheet along this length and hence this is also the size of the trailing edge in X . All of the field lines and hence the trailing edge travels at V_F away from the X -line.

The expansion of the PO region displaces the lobe field. Due to the frozen-in condition, the magnetic field and plasma move as one; hence when the PO region expands, it displaces the lobe field which then drapes around it. At locations where the PO boundary of the expanded PO region is inclined (the leading and trailing edges), the draped field is also inclined which causes the leading and trailing magnetic excursions (of the B_Z bipolar signature). The magnitude of the trailing excursion is greater than that of the leading excursion; this is because the field at the leading edge partly drapes around and also goes through the leading edge, whereas at the trailing edge the field only drapes around the leading edge. In addition, the disproportionate leading and trailing excursion magnitudes is partly due to the steeper angle of the inclined boundary of the trailing edge compared to the leading edge which is caused by the reorientation of the magnetic field (and separatrix and hence the trailing edge of the PO boundary) which is due to reconnection. In the plots taken $2t_R$ after reconnection ceased, the PO boundary is horizontal between the leading and trailing edges. Above and below the horizontal part of the PO boundary, the field is not inclined (and does not change in strength) and hence changes in B_X and B_Z only occur above and below the inclined boundaries.

The expansion of the PO region causes a compression in the lobe and a peak in B_X in this region. The lobe compression was plotted against pitch angle and much like the velocity plots, the lobe compression increases with

pitch angle and tends to infinity at $\sim 71^\circ$ in the FLRF and $\sim 36^\circ$ in the ERF. The expansion of the PO region causes a reduction in magnetic field strength of this region, which is mostly in B_X . Table 1 shows that for a greater unexpanded size of the PO region, the expanded size and the difference in size caused by expansion is greater. However, the percentage change in size due to expansion is smaller (the percentage change in size is also referred to as the expansion factor).

Figure 34 shows that B_X in the PO region peaks at the centre (in X) of the PO region, this can be explained by considering the expansion of the PO region. According to Figure 33, at locations closer to the centre of the PO region (in X), the pre-expansion size of the PO region is greater; Table 1 shows that at greater pre-expansion lobe sizes (inferred from pre-expansion size of the PO region) the expansion factor of the PO region is smaller, leading to a smaller reduction in B_X and a greater post-expansion value of B_X within this region. This can be explained by considering the size of the lobe; the regions of smallest lobe have the greatest increase in pressure per metre of compression and hence require the least compression to regain pressure balance, this leads to the smallest reductions in B_X and hence largest value of B_X (shown in Table 1). Therefore at locations closer to the centre (in X) of the PO region, the expansion factor is smaller and B_X is greater which causes a peak in B_X within the PO region. This is also the cause of the slight angle of the field below the leading edge of the PO boundary, the reducing B_X coupled with a fairly constant B_Z leads to an increasing magnetic field angle. This effect can be seen in the diagram of Figure 33 but is too small to be seen in any of the magnetic field plots. The B_Z profile in the PO region (below the trailing edge) is caused by the

reorientation of the field during reconnection and hence the profile of B_Z matches the profile of the electric field present during reconnection.

The magnetic excursions are caused by an inclined field above the inclined boundaries and hence have the same velocity and X-size of the inclined boundary that cause them. Both the leading edge and leading excursion are caused by particles, they travel at $V_{\parallel\text{out}}$ and are $X = V_{\parallel\text{out}}t_R$ long. Both the trailing edge and trailing excursion are caused by reoriented field lines that cross the current sheet, they travel at V_F and are $X = V_F t_R$ long. Hence the broadening of the TCR signature with time is as a result of the leading excursion travelling faster (at $V_{\parallel\text{out}}$) than the trailing excursion (at V_F). When the excursion lengths (in X) are divided by their velocities, the resulting duration of the magnetic excursions (observed by a spacecraft) are both t_R and equal to each other, which explains why the excursions have different X-sizes but the same duration.

The magnetic signature changes in time. $1t_R$ seconds after reconnection ceases, the structure does not grow in Z but does grow in X; the magnetic signature broadens causing a widening of the B_X peak and the separation of the B_Z excursions. If enough time passes after reconnection ceases, the TCR signature may not be recognisable.

The results of the hot particle model can be compared to the results of the MHD model. In the lobe, the B_X plot of both models is similar; both show a peak in B_X coinciding with the B_Z bipolar signature. Both models have a bipolar signature with a leading excursion which is smaller in magnitude

than the trailing excursion. However in the MHD model, the duration of the leading excursion is smaller than that of the trailing excursion whereas in the hot particle model, the durations are the same.

In both models, with distance away from the current sheet, the excursions of the bipolar signature reduce in magnitude; the relative difference in size of the B_Z excursions increases in the MHD model with distance from the current sheet but doesn't change in the hot particle model. In the MHD model, B_X changes with Z . In the hot particle model, the tail is bounded by a rigid magnetopause; the system is in vertical pressure balance and hence the B_X plot does not show variation in Z . As the differences are due to the setup rather than physical reasons, the B_X plots cannot be directly compared.

In the MHD model, with time after reconnection ceases, the flux bulge expands in Z . This leads to an increase in magnitude of both the B_X and B_Z signatures; with increasing time, the relative difference between the two excursions decreases in B_Z but increases in B_X . In the hot particle model the structure expands in X ; this causes the peak in B_X to broaden but does not change the magnitudes and durations of the magnetic excursions of the B_Z bipolar signature, however it does cause them to separate with time.

During reconnection, the removal of flux from above the X-line reduces the lobe magnetic field strength (and changes the lobe Alfvén speed) which in principal must change the horizontal stress balance. This is not taken into

consideration in this model as the effect is small, the difference between the initial and final lobe B_x is $\sim 5\%$ of the initial lobe B_x .

In the real tail, reconnection can be expected to occur within the pre-existing plasma sheet. Once all of the plasma sheet flux is reconnected, reconnection of lobe flux will begin; as this flux will have a greater magnetic tension, the reconnected lobe flux will travel faster than the plasma sheet flux and have a greater effect. Thus any flux bulge which is initially made by the reconnection of plasma sheet field lines will be rapidly swept away by subsequently reconnected lobe field lines in a direction away from the X-line, along X. Hence, even if the plasma sheet is present, a structure created from lobe flux as modeled here will likely dominate.

The model results can be compared to observation. Flux bulges are formed from one X-line and so comparisons should only be made to observations of structures formed from one X-line. One region which is expected to contain only flux bulges is the region Earthward of the NENL however the magnetic field strength, particle density and velocity of the region differs too greatly from that of the model to make a useful comparison. Observations from further downtail are comparable. Tailward of the NENL, TCRs are caused by either flux bulges or plasmoids; a survey of TCRs that include flux bulges and discounts plasmoids is required for a direct comparison; while most of the studies do not separate flux bulges from plasmoids, the closest comparison that can be made is to structures observed in the region of the tail where the greatest proportion of TCRs are caused by flux bulges. Tailward of the DNL, flux bulges are formed from

one X-line, the DNL. Between the two X-lines, flux bulges can form from two sources, tailward travelling flux bulges formed at the NENL and Earthward travelling flux bulges formed at the DNL. As there are two sources of flux bulges between the X-lines, a greater proportion of the TCRs in this region are expected to be caused by flux bulges compared to the region tailward of the DNL and hence observations made between the X-lines are more comparable to the model results than observations made tailward of the DNL.

One survey exists where the majority of the observations are between the X-lines. Slavin et al. (1993) surveys TCRs between 50 - 210 R_E , two thirds of the structures are observed between the X-lines. The Slavin et al. (1993) survey found that the structures causing the TCRs had an average Z size of 15 R_E , an average velocity of 583 km s^{-1} and an average compression of 7.6%. The magnetic structure presented in the example model run causes a compression of 2.3% and is of Z size 4.4 R_E (from edge to edge). The structure has a particle and field line velocity of 891 and 484 km s^{-1} which results in an average velocity of 688 km s^{-1} . A comparison of the velocities shows that the two are fairly similar. The model flux bulge is faster than the average of the observed structures, the speed difference could be attributed to the lack of a plasma sheet; reconnected plasma sheet field lines will have a smaller magnetic field strength and travel slower than lobe field lines. Although the lobe field lines will sweep the plasma sheet field lines away, the observed reconnected lobe field lines may move slower than those modelled due to the presence of the slower moving reconnected plasma sheet field lines in their path. The average size and compression ratio of the structures observed in Slavin et al. (1993) is

greater than that we have reproduced in our model. However, the size and compression ratio of the model depend on the pitch angle, which is limited to conform to the small angle approximation. An improved model without the 50° limitation could potentially create structures with a size and compression more comparable to the observations. Further comparison of the results would benefit from surveys that only contain TCRs formed by flux bulges. This requires either two spacecraft in the lobe separated in space (along X) to observe the broadening of the bipolar signature or simultaneous observations in the lobe and PO region to identify flux bulges.

3.6 Conclusion

The goal of this study was to create a model that reconciles the features of two time-dependent reconnection models. The MHD model results in a flux bulge with a lobe compression (TCR); the cold particle model results in a flux bulge with a PO region which has a magnetic field component in X however it does not provide an expansion in Z and therefore cannot account for the lobe compression signatures (TCRs) regularly observed by spacecraft located in the tail lobes. A new model was created by modifying the cold particle model so it accounts for thermal energy and hence perpendicular pressure in the PO region. This was modeled by including a constant pitch angle scattering (α) of particles as they cross the current sheet. In the field line rest frame, a greater scattering pitch angle requires a greater inflow velocity for stress balance. As the scattering pitch angle increases, perpendicular velocity increases and outflow velocity decreases (until $\alpha \sim 58^\circ$ at which point both begin increasing). However, stress balance on reconnected field lines cannot be satisfied if the field aligned

inflow particle is scattered to more than $\alpha \sim 71^\circ$ in the FLRF and $\alpha \sim 36^\circ$ in the ERF.

The addition of thermal pressure alters the pressure balance perpendicular to the current sheet and thus the PO region must expand to equalise the pressure; this results in a reduction of the magnetic field strength within the PO region. It also has the effect of compressing lobe which increases its magnetic field strength; this causes a magnetic signature consistent with that observed during a TCR. These characteristics are explicitly illustrated by plotting the magnetic signature expected at a sample height at a given time. The sample heights are different distances from the current sheet, one passing through the centre (in Z) of the PO region (along the current sheet), one passing through the PO region (off centre) and one outside of the PO region (through the lobe).

The sample through the lobe indeed reproduces a signature consistent with that of a TCR (a peak in B_X and bipolar signature in B_Z). The B_Z bipolar signature of the TCR in this model shows a trailing excursion which is larger in magnitude and spans a smaller X distance than the leading excursion although the same bipolar signature has excursions of similar durations when plotted against time. The sample through the PO region shows a peak in B_X at the centre (in X) of the PO region and a peak in B_Z at the trailing end of the PO region. With time, the difference in velocity between the outflow particles and the recoiling field lines causes the structure to expand in X, this causes the two excursions of the bipolar B_Z TCR signature separate in time. The TCR signature and/or the flux bulge

may not be recognised in spacecraft observations if enough time passes (and the flux bulge is sufficiently far from the reconnection site).

Chapter 4

Plasmoid Evolution in a Simple Numerical Particle Simulation

4.1 Introduction

In the NENL model (Baker et al., 1996), the magnetosphere experiences a net increase in flux due to an imbalance between the dayside and nightside reconnection rates (where nightside reconnection occurs at the DNL). Once the amount of flux reaches a threshold value, reconnection is triggered at the NENL and a plasmoid is formed between the NENL and the DNL. If the reconnection rate of the NENL is greater than that at the DNL, then the plasmoid will be surrounded by flux that is open on the tailward side. The greater magnetic tension on the NENL side of the plasmoid will thus force the plasmoid downtail. The plasmoid is ejected tailward causing the removal of flux and plasma from the magnetosphere, as shown in Figure 39.

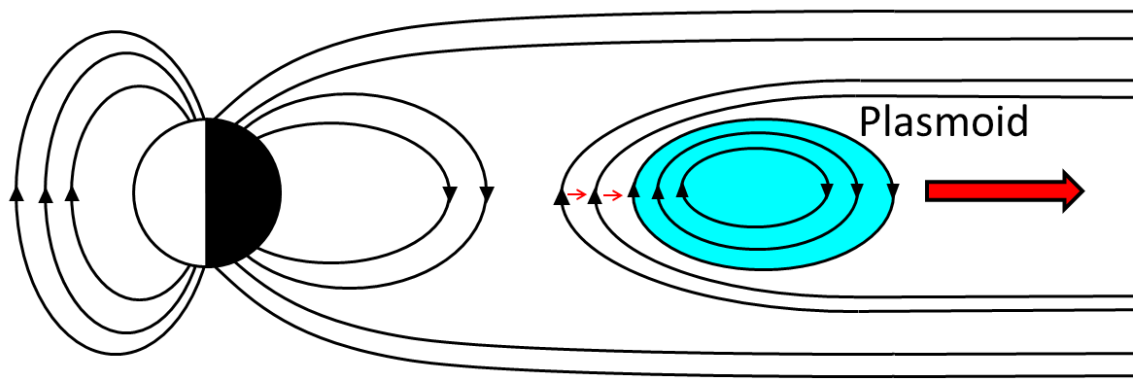


Figure 39: Diagram of the magnetosphere which contains a plasmoid (in turquoise) which is moving anti-sunward due to the magnetic tension force (small red arrows) of the reconnected magnetic field lines.

Several surveys of plasmoids have been conducted. Moldwin and Hughes (1992) observed 366 plasmoids between 16 - 210 R_E downtail. They found plasmoids had an average size of 16.7 R_E and an average tailward velocity of 497 km s^{-1} . Ieda et al. (1998) surveyed 824 plasmoids between 50 - 250 R_E downtail and found plasmoids had an average size of 10 R_E . Scholer et al (1984b) searched for plasmoids between 80 - 220 R_E using ISEE 3;. In the survey, 20 plasmoids were observed, which had an average plasmoid size of $\sim 80 R_E$ and an average velocity of 600 km s^{-1} .

The magnetotail has several features that change downtail, for example, it has a magnetic gradient, density gradient and particle velocity gradient (Zwickl et al., 1984; Slavin et al., 1985). These affect the plasmoid as it travels downtail; two studies have charted the downtail evolution of the plasmoid. The survey carried out by Ieda et al. (1998) found that plasmoids form in the near tail; the observed plasmoid size and speed increases downtail and are constant by 75 and 165 R_E respectively. The survey by Moldwin and Hughes (1992) found that the observed plasmoid

size increases downtail but neither velocity nor size change much past $100 R_E$. This partly explains the differences in average size of the plasmoids of the surveys mentioned above, 10 and $16.7 R_E$ for Moldwin and Hughes (1992) and Ieda et al. (1998) compared to $80 R_E$ for Scholer et al. (1984); the latter observes structures that are, on average, further tailward than the other surveys, hence leading to the greatest average plasmoid size.

In an effort to understand the formation and evolution of plasmoids further, a number of models have previously been created; they are typically based on one of two methodologies, MHD (e.g. Slinker et al., 1995) and single particle physics (e.g. particle in cell method, Price and Swift, 1986). The MHD models do not account for variations in the velocity of individual particles at a given location. This is not the case for the single particle models which will track each particle individually leading to more accurate velocities and information on the behaviour of the particles during plasmoid evolution, but at the expense, usually, of computational complexity.

In this chapter the movement and evolution of a plasmoid and its constituent particles is studied in a relatively simple numerical model by adapting the work on single particle interactions with a field line kink and methods of the previous chapter in order to apply them to closed-loop plasmoid-like magnetic structures. The study focuses on the movement of the particle populations (within the plasmoid) and their effect on the movement and evolution of the plasmoid itself. The effect of magnetotail gradients on the populations and the plasmoid as a whole is also included.

The model is based on the cold particle model described in detail in Chapter 3. Section 4.2 describes the adaptations required to apply the cold particle model to include the effects of particles with different velocities. The section also details the assumptions, equations and set up of the model. Section 4.3 presents the results of the movement of the plasmoid and of the particles separately, a comparison of the two and the results of the model are discussed in section 4.4.

4.2 Model

4.2.1 Plasmoid Specifics

The specifics of the plasmoid model created for this project are now detailed; a sketch of the model is shown in Figure 40. Plasmoids in the model are assumed to be made of concentric loops of field lines with plasma on each field line. The plasma is frozen into the field lines and hence have no net transport motion perpendicular to it. The field lines are kinked at the point they cross the current sheet and thus have magnetic tension which must be balanced by the changes in momentum of the particles as they move around the loop. In this model we address a simplified representation of the plasmoid as a single loop with field aligned particles which are reflected at the ends of the loop. This approach significantly reduces the complexity of the plasmoid while retaining the key characteristics of the plasmoid, mentioned above.

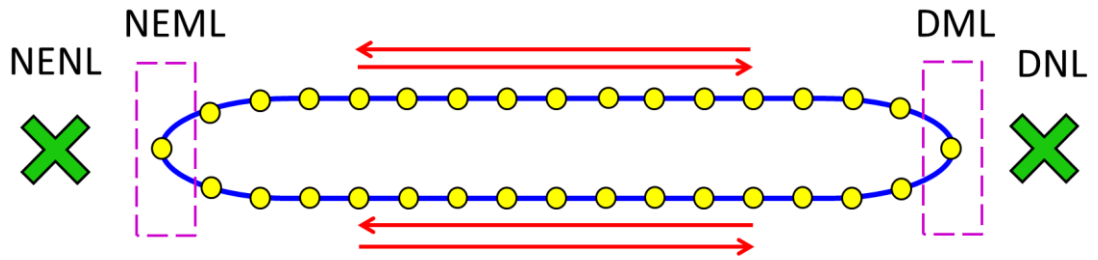


Figure 40: Sketch of the magnetic loop used to represent a plasmoid. The loop is formed from reconnection occurring at the NENL and DNL. The particles on the magnetic loop (yellow circles) can move in either direction along the loop. The magnetic field is kinked at the ends of the loop which are referred to as the near Earth and distant loop ends (NEML and DML respectively).

The loop is created by magnetic reconnection occurring at two points within the magnetotail; initially, unconnected magnetic flux tubes exist in the northern and southern tail lobes which are directed antiparallel to each other; they are then connected to each other by the action of reconnection, occurring simultaneously at the NENL and at the DNL, creating a closed magnetic loop between the two neutral lines. The two points where the magnetic loop crosses the current sheet are referred to as the Near Earth Magnetic Loop end (NEML) and the Distant Magnetic Loop end (DML). The effects of the X-lines on the plasmoid are not included in the model (for simplicity) and hence the DNL is assumed to move tailward with the plasmoid to avoid any subsequent interaction between the plasmoid and this neutral line, also both neutral lines are assumed to reconnect negligible amounts of flux during the runtime of the model.

In magnetotail reconnection, once all of the plasma sheet flux is reconnected, lobe field lines are then reconnected resulting in a plasmoid with an outer layer of lobe field lines. If the reconnection rate is greater at one X-line (usually at the NENL) then some of the lobe field lines will be

open on the tailward side of the plasmoid and will drape around the plasmoid and eventually apply a net (tailward) force on the Earthward side of the plasmoid. As the lobe field lines have a greater magnetic field strength and thus magnetic tension than the plasma sheet field lines, the interaction of particles with lobe field lines will have a greater effect on the particle dynamics, thus the modeled plasmoid is assumed to be made of lobe field lines. The plasma sheet magnetic field lines that may have been reconnected earlier in the process and the associated plasma are considered to be dynamically unimportant. However, note that normally these field lines and the plasma on them would form a core at the centre of a plasmoid which is not explicitly considered here.

The assumption is made that the magnetic field structure at the two ends of the loop maintains a sharply-kinked structure which does not unwind significantly during the period of plasmoid evolution modeled in this study (the terms kink and magnetic loop end refer to the same hairpin shaped magnetic field centred on the current sheet and the two terms are used interchangeably). Under this assumption, the principles of stress balance applied in the previous chapter can be used to understand the evolution of the two ends of the magnetic loop. However, the essential difference, and the new physics which has to be introduced, is that the plasma inflow into the magnetic field kinks is now variable. In particular the stress balance at one end of the magnetic loop and hence its motion, will be affected by the presence of particles which have previously been accelerated at the other end of the loop and vice versa. In this way, the net motion of the magnetic loop representing the plasmoid is expected to be the result of a complex set

of interactions between the fields and the particles within the loop. This simple model seeks to understand this net motion.

4.2.2 Stress Balance for Multi Speed Particles

Tracking the evolution of the plasmoid model created here requires knowing the velocity and position of the magnetic loop ends and all the particles on the loop at all times. These are controlled by the requirements of the stress balance and velocity equations introduced in Chapter 3, although the application of these conditions must now be modified to account for the presence of particles travelling at multiple speeds. Chapter 3 argued that the stress balance equation for particles interacting with a current sheet, across which the major component of the magnetic field reverses (with a small normal component as is appropriate for the region downstream from an active reconnection site), can be written as:

$$M_{\parallel} - P_{\perp} = \frac{B^2}{\mu_0} \quad (4.1)$$

For a cold inflow and outflow plasma ($P_{\parallel} = P_{\perp} = 0$) with density n and field aligned velocity V' in the field aligned rest frame, the stress balance equation becomes:

$$2nmV'^2 = \frac{B^2}{\mu_0} \quad (4.2)$$

This equation directly relates the change in momentum of the particles (in the FLRF) as they move around the kink in the field, to the associated field tension. In the FLRF, a plasma population has a flux of nV' particles per second and each particle experiences a change in momentum of $\Delta p = 2m_i V'$

as it reverses its direction during its interaction with the field kink. Alternately, if N separate populations are considered, in which particles of density n_N have a common velocity V'_N in the FLRF, then the stress balance equation relating the change of momentum of the particles of different speeds to the magnetic tension becomes:

$$2n_1mV_1'^2 + 2n_2mV_2'^2 \dots + 2n_{N-1}mV_{N-1}'^2 + 2n_NmV_N'^2 = \frac{B^2}{\mu_0} \quad (4.3)$$

Again, this equation reflects the total change of momentum of the N particle populations which each individually interact with the field line kink at a rate of $n_N V'_N$ particles per second, with an associated $\Delta p_N = 2mV'_N$ for each particle. Ultimately, extending this model philosophy to more and more particles implies the need to track single particles, in which case the problem becomes one of following which particles interact with the field line kink in a given time period, Δt . To reduce the equation to one which involves single particles, rather than densities, the assumption is made that there is only one particle at each speed that interacts with the magnetic loop end in the time step, such that $n_N V'_N = 1$. The stress balance is now the magnetic tension balanced by the combined rate of change of momentum for the N individual particles (each at its own speed) which interact with the end of the magnetic loop in the time Δt . Substituting in $n_N V'_N = 1$ into equation 4.3 (which now includes Δt) returns:

$$\frac{(\Delta p_1 + \Delta p_2 \dots + \Delta p_{N-2} + \Delta p_{N-1})}{\Delta t} = \frac{(2mV'_1 + 2mV'_2 \dots + 2mV'_{N-1} + 2mV'_N)}{\Delta t} = \pm \frac{B^2}{\mu_0} \mathbf{\hat{b}} \quad (4.4)$$

This model uses the same small angle approximation used in previous chapters and hence the major forces operate in the direction parallel to the current sheet (and thus the pressures approximate to the X-directed

component in the model). The above equation in principle relates to vector quantities; a contracting field line can, in principle, interact with a particle travelling towards or away from the kink in the field line (in the case of the latter the field line must be moving faster than the particle). Hence the direction of the particle, as well as its velocity is relevant to its contribution to the overall balance of stresses, and thus the vector form is adopted to account for particles moving in either direction.

The magnetic tension now has a unit vector, $\hat{\mathbf{b}}$, this is directed in the $+X_{\text{GSM}}$ direction. The above equation can apply to both ends of the magnetic loop (the NEML and DML); the magnetic tension of the NEML and DML act in opposite directions, which is accounted for in the \pm sign in front of the magnetic tension. The magnetic tension of the DML is directed along $+X_{\text{GSM}}$, which is the same direction as the unit vector $\hat{\mathbf{b}}$ and hence, if the equation is applied to the DML, the sign in front of the magnetic tension is positive. The opposite can be said for the NEML. It is worth noting that the velocities are now also vectors and hence can be travelling towards or away from a loop end.

Using a similar approach to the Chapter 3, equations are now derived linking the ERF particle velocity to the FLRF particle velocity. As discussed in Chapter 3, the difference between any velocity in the FLRF (\mathbf{V}') and that in the ERF (\mathbf{V}) is simply the field line velocity (which in this case is the speed of the relevant magnetic loop end):

$$\mathbf{V}'_{\parallel} - \mathbf{V}_{\parallel} = \mathbf{V}_F \quad (4.5)$$

In vector form, the above equation is relevant for both inflow and outflow velocities. Substituting equation 4.5 into equation 4.4 returns:

$$\frac{2m(\mathbf{V}_1 - \mathbf{V}_F) + 2m(\mathbf{V}_2 - \mathbf{V}_F) + \dots + 2m(\mathbf{V}_{N-1} - \mathbf{V}_F) + 2m(\mathbf{V}_N - \mathbf{V}_F)}{\Delta t} = \pm \frac{B^2}{\mu_0} \mathbf{b} \quad (4.6)$$

$$\frac{(\mathbf{V}_1 - \mathbf{V}_F) + (\mathbf{V}_2 - \mathbf{V}_F) + \dots + (\mathbf{V}_{N-1} - \mathbf{V}_F) + (\mathbf{V}_N - \mathbf{V}_F)}{\Delta t} = \pm \frac{B^2}{2m\mu_0} \mathbf{b} \quad (4.7)$$

$$\frac{\mathbf{V}_1 + \mathbf{V}_2 + \dots + \mathbf{V}_{N-1} + \mathbf{V}_N}{\Delta t} - \frac{N\mathbf{V}_F}{\Delta t} = \pm \frac{B^2}{2m\mu_0} \mathbf{b} \quad (4.8)$$

$$\frac{\mathbf{V}_1 + \mathbf{V}_2 + \dots + \mathbf{V}_{N-1} + \mathbf{V}_N}{\Delta t} \pm \frac{B^2}{2m\mu_0} \mathbf{b} = \frac{N\mathbf{V}_F}{\Delta t} \quad (4.9)$$

$$\mathbf{V}_F = \frac{\Delta t}{N} \left(\frac{\mathbf{V}_1 + \mathbf{V}_2 + \dots + \mathbf{V}_{N-1} + \mathbf{V}_N}{\Delta t} \pm \frac{B^2}{2m\mu_0} \mathbf{b} \right) \quad (4.10)$$

where \mathbf{V}_N refers to the inflow velocity of particles in the ERF. The equation shows the magnetic loop end velocity resulting from the stress balance of the magnetic tension and N particles in one time step. Using the equation relating the particle velocities in the FLRF and ERF (using both the inflow and outflow form of equation 4.5 separately) and the knowledge that (in the FLRF) $\mathbf{V}_{\parallel in}'$ and $\mathbf{V}_{\parallel out}'$ are equal and opposite ($\mathbf{V}_{\parallel in}' = -\mathbf{V}_{\parallel out}'$), the ERF outgoing velocity of any given particle can be calculated:

$$\mathbf{V}_{\parallel out} = \mathbf{V}_F + \mathbf{V}'_{\parallel out} = \mathbf{V}_F - \mathbf{V}'_{\parallel in} = \mathbf{V}_F - (\mathbf{V}_{\parallel in} - \mathbf{V}_F)$$

$$\mathbf{V}_{\parallel out} = 2\mathbf{V}_F - \mathbf{V}_{\parallel in} \quad (4.11)$$

These equations in principle allow us to calculate the different ERF outflow velocities of the particles and the magnetic loop end velocity from the ERF inflow velocities of the particles and the magnetic field strength at both the NEML and DML. However, the model requires an algorithm to search for consistent solutions, since changing \mathbf{V}_F results in changing the number of particles that will interact with the end of the magnetic loop. This

necessitates tracking of the speed and position of all particles and the two ends of the field line loop at all times.

4.2.3 Tracking

Creating a numerical particle model requires knowing the particle and magnetic loop end velocity and position at all times and hence both are tracked at each time step by the model. For each time step, there are a number of possible outcomes which depend on how many particles interact with the magnetic loop end; to find the solution which is physically plausible, the model calculates the values associated with many different interaction possibilities simultaneously and selects the appropriate one. Details of this can be understood with the aid of Figure 41.

Figure 41 contains 4 panels, each containing 3 particles (the circles) and a magnetic loop end (the blue curve). Panel A represents the time $t = 0$. At this time the 3 particles are approaching a contracting magnetic loop end (blue curve). Panels B, C and D are all one time step later ($\Delta t = 1$ and hence $t = 1$) and show the 3 possible final locations of the loop end (dashed blue curve) due to its interaction with 1, 2 and 3 of the particles respectively; the position of the particles at $t = 1$ does not take into account any interaction with the magnetic loop end, this information is used to calculate which particles must have interacted with the magnetic loop end during the time step. Of the three ($t = 1$) scenarios shown, only one is physically plausible. The dashed blue curve is the magnetic loop end position at $t = 1$; the magnetic loop end velocity and final position depends on the number of particles the magnetic loop end interacts with and hence it

is different in all three scenarios. Using the stress balance equation, the velocity of the magnetic loop end is calculated for all 3 possibilities.

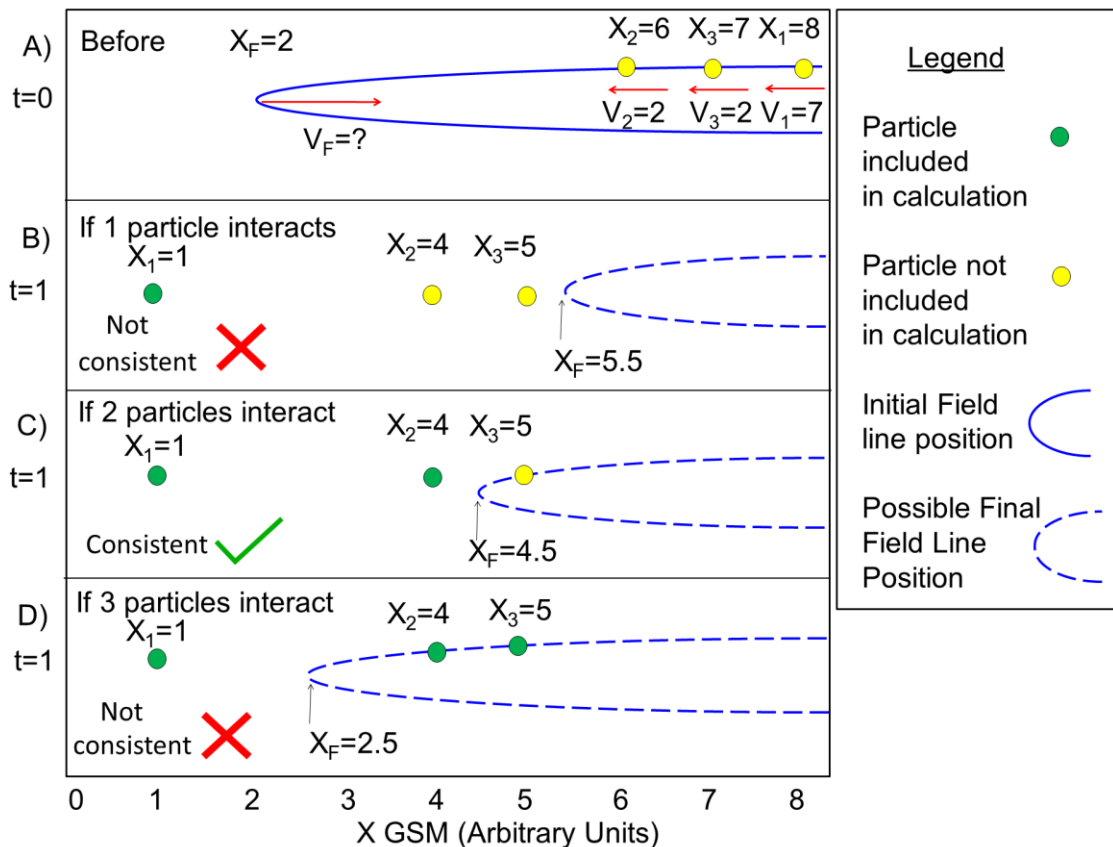


Figure 41: A simplified illustration of the method used to determine how many particles interact with the magnetic loop end during each time step. Panel A, at $t = 0$, shows 3 particles travelling towards a contracting magnetic loop end (blue curve). Panels B, C and D, at $t = 1$, show the position of the loop end (dashed blue curve) due to the interaction of the loop end with 1, 2 and 3 particles respectively where the final particle position assumes that there is no interaction of the particle and the magnetic loop end. The green circles are particles included in the magnetic loop end velocity calculations, the yellow circles are particles not included. Of the three scenarios, panel C is the only physically plausible scenario as the velocity calculation only considers particles that the loop end is predicted to move passed.

The subscripts of the particle position (X_N) refers to the order of the particle positions in X at $t = 1$. In each case, the colour of the particle indicates whether it has been included in the stress balance and magnetic loop end velocity calculation. Particles coloured green have been included in the calculation, particles coloured yellow have not. If the position of the loop end is such that it is passed a particle that was not included in the calculation, it is not a physically plausible solution.

In the first possibility, the stress balance and magnetic loop end velocity calculation involves only one particle (X_1); however, this solution implies that the resulting magnetic loop end position passes all three particles, but two of the particles are not included in the velocity calculations. This scenario is thus unrealistic since the velocity calculation does not take into account particles which the magnetic loop end passes. Another unrealistic scenario is seen in the third possibility; the velocity calculation is performed with all three particles but the implied velocity of the magnetic loop end obtained from the stress balance condition does not result in it passing the position of all three particles. Thus the second possibility is the only physically plausible scenario in this simplified example: in the scenario, the velocity calculation only considers particles that the loop end is predicted to move passed. In the algorithm, once a consistent solution for the number of interacting particles and the final magnetic loop end velocity is known, the velocity and position of each of the interacting particles is recalculated and the model is moved to the next time step.

4.2.4 Model Specifications

To make the model as realistic as possible, typically observed values of the undisturbed parameters in the tail are used, where appropriate, in the model. Thus the NENL is placed at $X_{\text{GSM}} \sim -25 R_E$ (Nagai et al., 1997) and the DNL at $X_{\text{GSM}} \sim -120 R_E$ (Zwickl et al., 1984; Slavin et al., 1985). From a study by Slavin et al. (1985), the magnetic field varies with downtail distance according to the equation:

$$|B| \sim B_X \sim 125(X^{-0.53 \pm 0.05}) \quad (4.12)$$

where X is the modulus of the X_{GSM} position in R_E and the magnetic field strength is in nT. This results in a value of 22.7 nT and 9.7 nT at $X_{\text{GSM}} = -25$ and $-120 R_E$ respectively. The equation is valid for $-130 < X_{\text{GSM}} < -20 R_E$; further tailward, $-220 < X_{\text{GSM}} < -130 R_E$, the magnetic field strength is constant at ~ 9 nT. The related work of Walker et al. (1975) shows that at $X_{\text{GSM}} \sim -900 R_E$, $|B| \sim B_X \sim 9$ nT. Hence B_X is set to the above equation between $-130 < X_{\text{GSM}} < -20 R_E$ and to a constant value of 9 nT at $X_{\text{GSM}} < -130 R_E$.

The lobe density and velocity was obtained from Zwickl et al. (1984); they found that the density and velocity between $-60 < X_{\text{GSM}} < 0 R_E$ is $\sim 0.01 \text{ cm}^{-3}$ and $\sim 140 \text{ km s}^{-1}$ and between $-120 < X_{\text{GSM}} < -180 R_E$ it is $\sim 0.1 \text{ cm}^{-3}$ and $\sim 170 \text{ km s}^{-1}$. The density and velocity of the lobe is assumed to vary linearly downtail (the latter has been observed by Slavin et al., (1985); by placing the densities and velocities mentioned above at the midpoint of the ranges and extrapolating the values, the density and velocity at the NENL are 0.00625 cm^{-3} and 138 km s^{-1} and at the DNL is

0.0775 cm^{-3} and 162 km s^{-1} . From here onwards all references to X_{GSM} refer to the nightside and hence the minus sign is dropped.

For simplicity only one species of particle was used in the model. As in the previous chapter, the inflow plasma is mostly of mantle and therefore solar wind origin (Rosenbauer et al., 1975) and hence is mostly made up of protons and electrons. Thus protons dynamics only is included in the model, assuming that they have a dominant effect on stress balance being larger in mass than electrons and assuming they are vastly more numerous than heavier ions (note that this may not always be the case during the substorm periods relevant to this study, when upwelling from the ionosphere may create a significant heavy ion population in the tail, Kistler et al., 1999).

A model which tracks a realistic number of protons in the lobe would have an extremely long run time. To reduce the run time of the model in order to operate within practical limits, groups of protons were tracked instead. The number of groups was significantly less than the realistic number of protons allowing for a faster runtime for the model. The groups are referred to as macro-particles which behave as one large particle, they move and interact as one. The particles in a group all begin at the same location (to the nearest metre cubed) and have the same initial speed. Any interaction between a field line and a group of particles with the same initial location and velocity results in all of the particles in the group having the same final location and velocity, hence the force and energy associated with the interactions does not change due to the use of macro-particles.

The number of macro-particles tracked was chosen based on the runtime of the model, the macro-particles was set to 1 million as this resulted in a runtime that was achievable in the timeframe of the project. Calculating the number of particles comprising each macro-particle (which is the number of particles in each group) required first calculating the macro-particle density. Using the densities mentioned above, the density at DNL is 12.4 times that at the NENL. The macro-particles were initially arranged in the model so that the number density increased linearly downtail and so that the macro-particle density at the DNL was 12.4 times that at the model NENL; for a run of 1 million macro-particles, the macro-particle density is $1.23 \times 10^{-6} \text{ m}^{-3}$ and $1.52 \times 10^{-5} \text{ m}^{-3}$ at the NENL and DNL respectively. The tail lobe has a mass density of $0.00625 \text{ cm}^{-3} \times 1.67 \times 10^{-27} \text{ kg}$ and $0.0775 \text{ cm}^{-3} \times 1.67 \times 10^{-27} \text{ kg}$ at the NENL and DNL respectively. By comparing the macro-particle density of the model lobe and the mass density of the real lobe, the mass of each macro-particle can be found:

$$n_{model} m_{model} = n_{real} m_{real}$$

$$m_{model} = \frac{n_{real} m_{real}}{n_{model}} \quad (4.13)$$

The macro-particle mass at the NENL and DNL is calculated and averaged; for a model of 1 million macro-particles, each macro-particle must have a mass of $4.2 \times 10^{-20} \text{ kg}$. As each macro-particle is a group of particles, the mass of each macro-particle indicates that each group contains ~ 25 million protons.

Due to the reduced number of particles necessarily used in the model, there are times when too few particles interact with the magnetic loop ends. This results in an unrealistically large solution for the loop end velocity; if this

happens infrequently, this leads to short bursts in velocity. To make the model more realistic and to reduce the occurrence of these bursts, the initial plasma was effectively heated by giving the particles a range of velocities in the direction parallel to the current sheet. This allows the particles to be more spread out in initial velocity space and reduces the number of occurrences when too few particles interact with the magnetic loop end during a simulation time step. To initiate this range of parallel velocities, a random velocity was added to the calculated velocity mentioned above. The random velocity is between -14.4 km s^{-1} and $+14.4 \text{ km s}^{-1}$ and the probability distribution of the random velocity is uniform. The upper and lower limits were arrived at by taking the velocity of the particles at the midpoint of the two X-lines (144 km s^{-1}) and using 10% of that value (with 10% being an arbitrary value).

Although a temperature has been included, its effect on the pressure is negligible. For a maxwellian distribution, the full width half maximum is the width of the distribution at a height of half the maximum. This is equal to $FWHM = 2\sigma\sqrt{2\ln 2}$. The equation includes the standard deviation which is $\sigma = \sqrt{\frac{kT}{m}}$. The velocity distribution of the population within the plasmoid can be approximated to a rectangular velocity distribution; in this case the full width half maximum is the velocity range of the particles (28.8 km s^{-1}). Using the previously mentioned equations, and substitution of the full width half maximum as 28.8 km s^{-1} , the thermal pressure (nkT , using the densities at the initial locations of the NEML and DML) in the plasmoid is between 2.5×10^{-6} and $2.5 \times 10^{-5} \text{ nPa}$, which is negligible compared to the dynamic pressure (0.0037 nPa) or magnetic tension (0.08 nPa) in the ERF.

In this chapter, all references to time refer to the time within the model (the plasmoid evolution time). The time step used in the model is one second. Hence the position and velocity of each particle and each magnetic loop end are updated every second. Despite the set-up discussed above, the loop end velocity will vary rapidly with time due to the coarseness of the time grid and the reduced number of particles which can realistically be tracked. Thus, in order to follow the overall trends, the loop end velocity was smoothed. This involved boxcar averaging the resulting time-series data, the width of the smoothing window was arbitrarily set to 5% of the total time. As the total model time is 1.5 hours, the smoothing window is 4.5 minutes (270 second). Thus in the results presented below, each smoothed data point is an average of 270 simulated data points. All of the data presented below are the raw values with the exception of the loop end velocity (which is shown in both its raw and smoothed form) and the plasmoid velocity, mean particle speed and mean particle velocity. In the following, reference is made to acceleration and deceleration, this refers only to speed of particles and magnetic loop ends and not velocity. Directions will be specified where necessary.

4.3 Results

The specifications were fed into the model; the model was run and the results are shown in Figure 42. Panel A shows the plasmoid size vs. downtail distance over 1.5 hours; the plasmoid size is defined as the length of the magnetic loop which is the distance between the NEML and DML, this is seen to oscillate over time. The plasmoid grows in size until $X = 200 R_E$ at which point, the plasmoid size oscillates; the oscillation

amplitude decreases with time. By the time the plasmoid has reached $600 R_E$, the plasmoid size has settled to $118 R_E$.

Panel B shows the position of the magnetic loop ends with respect to downtail distance over 1.5 hours, the location of the NEML and DEML are in green and blue respectively. The X-axis of the plot is downtail distance and the Y-axis is time. At $t = 0$, the loop is formed by reconnection occurring at both the NENL and DNL at $X_{GSM} = 25 R_E$ and $X_{GSM} = 120 R_E$, respectively. The plot shows the interaction of the magnetic loop ends with the plasma trapped on the loop which results in both loop ends heading downtail.

Panel C shows the plasmoid velocity (the average of the smoothed NEML and DML velocities, purple trace), the mean particle speed (red trace) and the mean particle velocity (green trace). The velocities are also expressed in energy, this is the energy per proton in keV, this is calculated using the proton mass and the velocity of the proton (which is the velocity of the macro-particle). The plasmoid velocity rapidly increases to 1450 km s^{-1} at $100 R_E$, then drops to a minimum of 750 km s^{-1} at $250 R_E$ and then slowly increases while oscillating reaching a final speed of 1000 km s^{-1} . The mean particle speed rapidly increases to 1400 km s^{-1} at $250 R_E$, reduces and then oscillates slightly; the speed eventually becomes constant at a velocity of 1200 km s^{-1} . The mean particle velocity increases until $200 R_E$ and is constant afterwards at 1000 km s^{-1} .

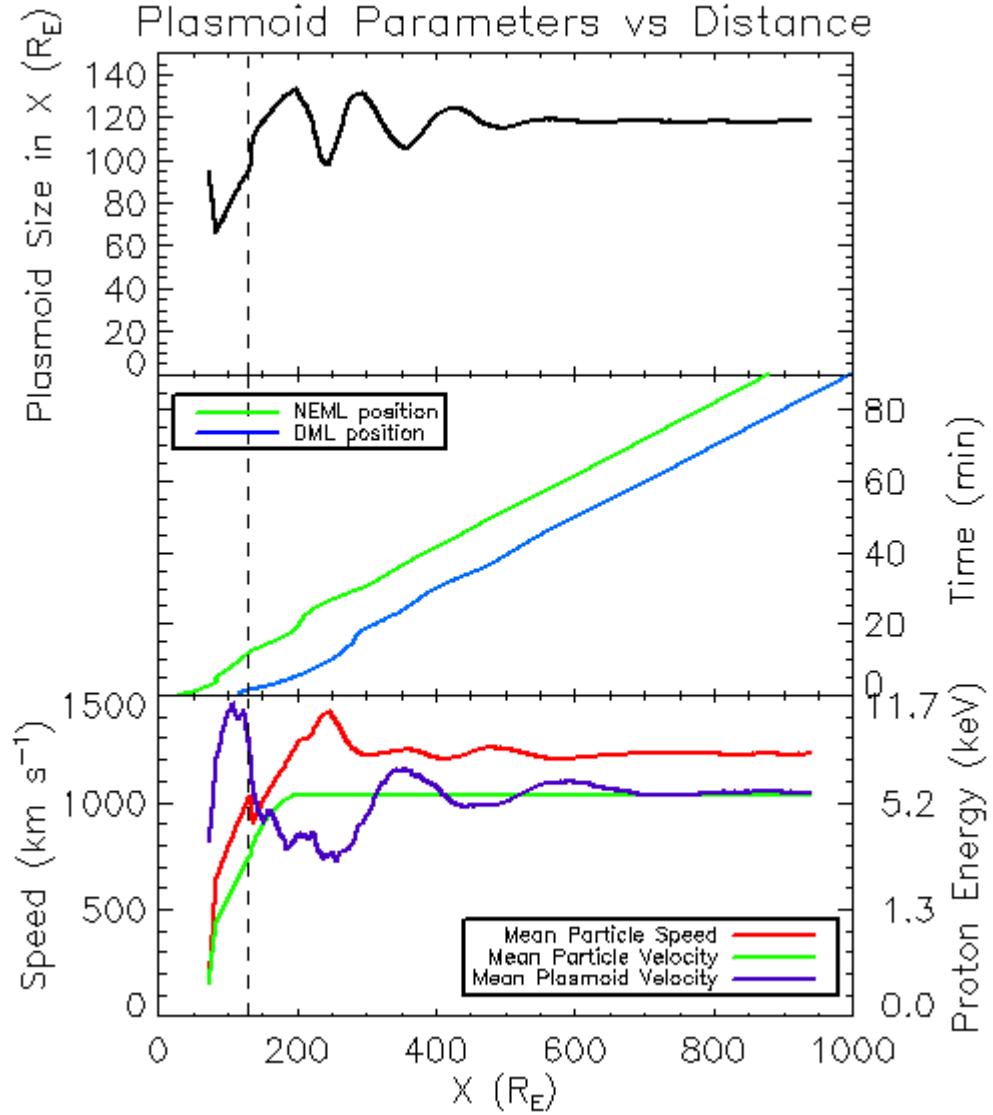


Figure 42: Plasmoid parameters vs. downtail distance over 1.5 hours. The dashed vertical line at $X = 130 R_E$ marks the location where the magnetic gradient ends. Panel A shows the length of the plasmoid in X . The plasmoid grows in size until $X = 200 R_E$ after which the plasmoid size oscillates. The amplitude of the oscillation decreases with time; by $X = 600 R_E$ the plasmoid size settles at $118 R_E$. Panel B shows the position of the NEML (green trace) and DML (blue trace) vs time, the plot shows both loop ends travel tailward. In Panel C, the plasmoid velocity (purple trace) rapidly increases to 1450 km s^{-1} at $100 R_E$, then drops to a minimum of 750 km s^{-1} at $250 R_E$ and then slowly increases while oscillating reaching a final speed of 1000 km s^{-1} . The mean particle speed (red trace) rapidly increases to 1400 km s^{-1} at $250 R_E$, then reduces to 1200 km s^{-1} and slightly oscillates. The mean particle velocity (green trace) increases until $200 R_E$ after which it becomes constant at 1000 km s^{-1} .

Figure 43 shows the variation of several plasmoid parameters versus time. Panel A shows the magnetic field strength at the location of the NEML (green trace) and DML (blue trace) as a function of time. The magnetic field strength at the DML peaks before reducing to 9 nT within the first 2 minutes while that at the NEML shows a steady decrease over time until 16 minutes (except at 4 minutes where it is briefly constant); after 16 minutes magnetic field strength at the DML becomes constant at 9 nT. Both variations in the magnetic field strength are caused by the position of the magnetic loop ends in the magnetic gradient of the tail. The dotted blue and green lines mark the times at which the NEML and DML leave the magnetic gradient respectively.

Panel B shows the plasmoid size increases rapidly, peaking at 12 minutes before oscillating; the amplitude of the oscillation decreases with time. At the maximum distance downtail the plasmoid size is $118 R_E$. Panel C shows the magnetic loop end velocity; the red and purple traces show the raw NEML and DML velocity and the green and blue traces show the smoothed NEML and DML velocity. The plot indicates that, during most of the period shown, both magnetic loop ends travel tailward; the averaged magnetic loop end velocity profile of the NEML and DML are two sinusoidal waves in close anti-phase with a decreasing amplitude. The oscillations of the loop end velocity then naturally coincide with the oscillations in the plasmoid size. By the end of the period shown, the velocity becomes constant at 1000 km s^{-1} .

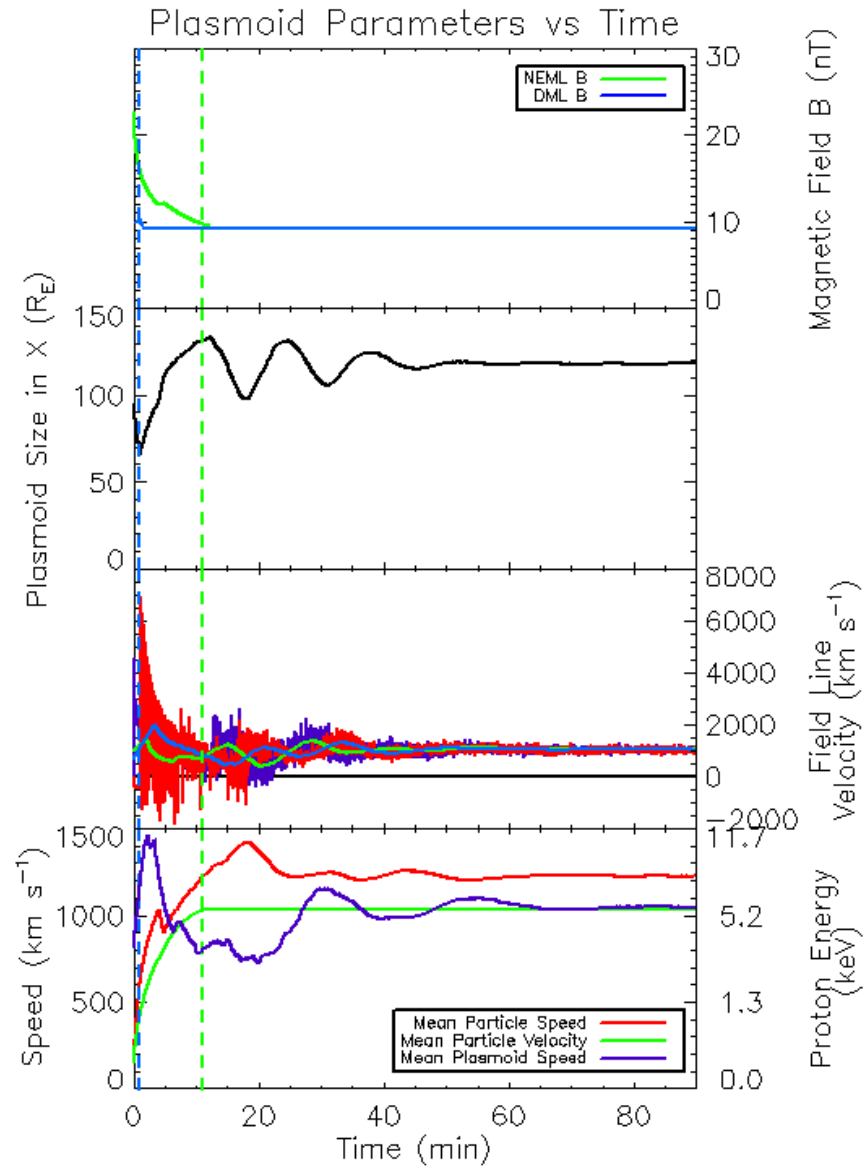


Figure 43: Plot showing various parameters of the plasmoid vs. time over 1.5 hours. The dotted line marks the times at which the NEML (green line) and DML (blue line) pass $130 R_E$. Panel A shows the magnetic field strength at the DML peaks and that at the NEML decreases with time, both eventually become constant at 9 nT. Panel B shows the plasmoid size grows until 12 mins before oscillating, the amplitude of which decreases with time, the final plasmoid size is $118 R_E$. In panel C, NEML and DML velocities are two sine waves in near anti-phase with decreasing amplitudes which eventually become constant at 1000 km s^{-1} . In Panel D, the plasmoid velocity (purple trace) rapidly increases to 1450 km s^{-1} at 2 mins, then drops to a minimum of 750 km s^{-1} at 20 mins and then slowly increases while oscillating reaching a final speed of 1000 km s^{-1} . The mean particle speed (red trace) rapidly increases and peaks at 1400 km s^{-1} at 18 mins, then oscillates before becoming constant at velocity of 1200 km s^{-1} . The mean particle velocity (green trace) increases until 11 mins after which it becomes constant at 1000 km s^{-1} .

Panel D shows the plasmoid velocity (the average of the smoothed NEML and DML velocities, purple trace), mean particle speed (red trace) and mean particle velocity (green trace). The mean particle speed rapidly increases and peaks at 1400 km s^{-1} at 18 minutes, then oscillates with peaks at 30 and 45 minutes. At the mean particle speed peaks, the plasmoid size troughs. The mean particle velocity increases until 11 minutes (which coincides with the NEML moving out of the magnetic gradient) after which it becomes constant at 1000 km s^{-1} . The plasmoid velocity rapidly increases to 1450 km s^{-1} at 2 minutes, then drops to a minimum of 750 km s^{-1} at 20 minutes and then slowly increases while oscillating reaching a final speed of 1000 km s^{-1} . This final speed is consistent with the magnetic loop end velocities and the mean particle velocity, showing that by the end of the run, the bulk plasma and the magnetic structure are moving in concert downtail.

The plasmoid parameters in Figure 43 can be explained with reference to Figure 44 which shows plots of the velocities of the individual macro-particles within the plasmoid vs. model X component at $t = 0, 40, 64, 112, 240$ and 592 seconds. Each red and purple dot represents an Earthward and tailward moving macro-particle respectively; the green and blue lines represent the locations of the NEML and DML respectively at the relevant time.

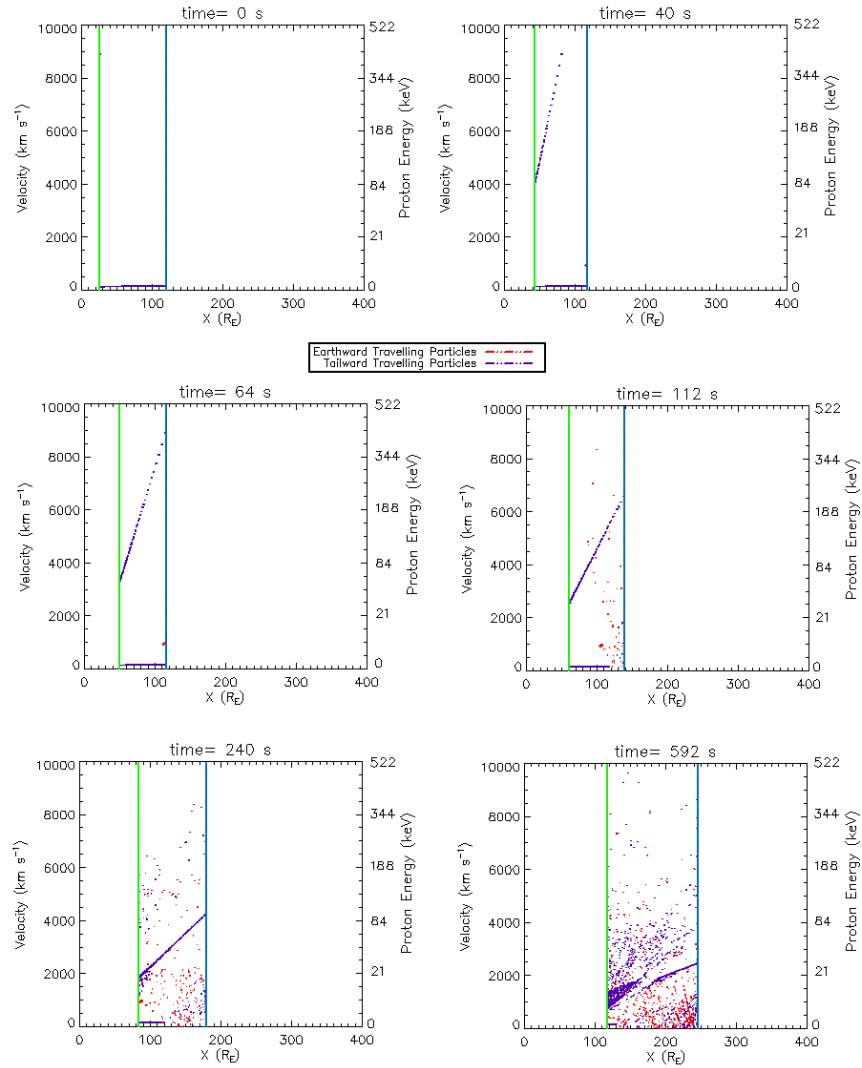


Figure 44: Plots of the velocities of the individual macro-particles within the plasmoid vs. X distance at $t = 0, 40, 64, 112, 240$ and 592 seconds. The plots contain the NEML and DML (green and blue lines respectively) and the Earthward and tailward travelling macro-particles (red and purple dots respectively). At 0 s, the particles are travelling tailwards (between $138 - 162 \text{ km s}^{-1}$, they appear as the purple line near the bottom of the plot). At 40 s, some particles have been accelerated at both magnetic loop ends, but remain as well separated populations in model space (one group is between $40 - 80 R_E$ with speeds of $4000 - 9000 \text{ km s}^{-1}$ and the other is near the DML between $120-130 R_E$ with speeds of 950 km s^{-1}). At 64 s, the first of the particles accelerated at the NEML reach and interact with the DML pushing it back and ceasing the acceleration of the undisturbed particles. At 112 s, a small clump of particles travelling Earthwards at 950 km s^{-1} can be seen near $X = 100 R_E$. By 240 s this group reaches the NEML, the loop end is pushed back and ceases accelerating the undisturbed particles momentarily. By 592 s, a complex mixture of particles can be seen within the model plasmoid. There are now two separate tailward travelling populations, one at $115 - 160 R_E$ ($500 - 2000 \text{ km s}^{-1}$) and one at $160 - 250 R_E$ ($1200 - 2500 \text{ km s}^{-1}$).

At $t = 0$ seconds (top left panel), the particles are all travelling tailward at the typical particle speed in the lobe (between $138 - 162 \text{ km s}^{-1}$ as set in the initial conditions); before any interaction with either magnetic loop end, the particles are referred to as the undisturbed particles and appear as the purple line near the bottom of the plot. At $t = 40$ seconds, particles which have been accelerated at both magnetic loop ends are clearly visible as two separate populations: those accelerated at the NEML (to $4000 - 9000 \text{ km s}^{-1}$) located between $40 - 80 R_E$ and those accelerated at the DML (to 950 km s^{-1}) located near the DML between $120 - 130 R_E$. The latter population is notably slower than the former population.

At $t = 64$ seconds, the first of the particles accelerated at the NEML reaches and interacts with the DML. This changes the stress balance conditions and pushes the DML back (against its tension, also noted as receding elsewhere in the chapter) and ceases the acceleration of the undisturbed particles momentarily. As the population pushes the DML back, it causes the plasmoid to expand; as the plasmoid had been contracting prior to this, this point in time marks the minimum size of the plasmoid which is $70 R_E$, this is the 1st minimum in the plot of plasmoid size in Figure 42 (at $80 R_E$ downtail) and Figure 43 (at 1 minute).

At $t = 112$ seconds, after being accelerated at the DML, a small clump of particles travelling Earthwards at 950 km s^{-1} , can be seen near $100 R_E$. By $t = 240$ seconds, half of the undisturbed particles have been accelerated at the NEML. The Earthward travelling population interacts with the NEML,

altering the stress balance condition there, pushing the NEML back and momentarily ceasing acceleration of the undisturbed particles.

By $t = 592$ s, a complex mix of particles of various speeds can be seen within the plasmoid loop. The majority of the particles are within two tailward travelling populations, one at $115 - 160 R_E$ ($500 - 2000 \text{ km s}^{-1}$) and one at $160 - 250 R_E$ ($1200 - 2500 \text{ km s}^{-1}$). In addition, the previously Earthward travelling population is accelerated (with a reversal in direction) at the NEML, this now tailward travelling population adds to the tailward travelling population at $115 - 160 R_E$

Figure 45 shows plots of the velocities of the individual macro-particles within the plasmoid vs. X distance at $t = 784, 1072, 1409$ and $t \gg 1409$ seconds. The red and purple dots represent Earthward and tailward moving particles respectively. The green and blue lines represent the locations of NEML and DML respectively.

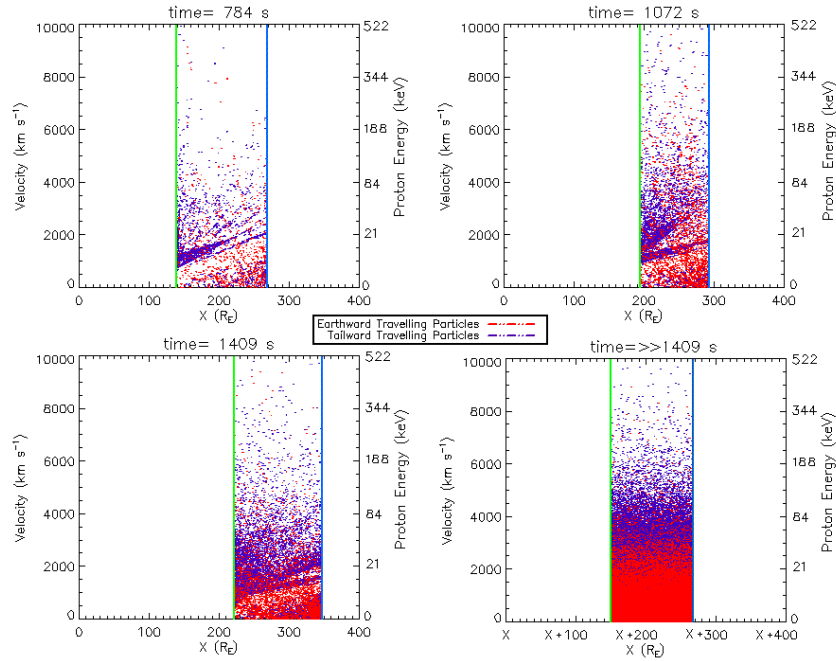


Figure 45: Plots of the velocities of the individual macro-particles within the plasmoid vs. X distance at $t = 784$, 1072 , 1409 and $t \gg 1409$ s. The plots contain the NEML and DML (green and blue lines respectively) and the Earthward and tailward travelling macro-particles (red and purple dots respectively). At 784 s, all of the undisturbed particles near the NEML have been accelerated, an Earthward travelling population can be seen ($200 - 270 R_E$, $0 - 1200 \text{ km s}^{-1}$) and the two separate tailward travelling populations can be seen ($140 - 210 R_E$, $700 - 2000 \text{ km s}^{-1}$ and $210 - 270 R_E$, $1500 - 2200 \text{ km s}^{-1}$). At 1072 s the (tailward travelling) population that was located further tailward, has been accelerated at the DML and the (tailward travelling) population that was located further Earthwards, interacts with at the DML. Part of this same population is accelerated tailward by the NEML (with no change in direction) to $1500 - 4000 \text{ km s}^{-1}$. Simultaneously part of the Earthward travelling population mentioned previously (784 s) interacts with the NEML. At 1409 s the population interacting with the NEML has a velocity gradient. At $t \gg 1409$ s, the density and velocity distribution has equalised across the plasmoid. The tailward travelling particles have a greater speed than the Earthward travelling particles.

At $t = 784$ s all of the undisturbed particles near the NEML have been accelerated, the decrease in pressure acting on the NEML causes the NEML to increase in tailward velocity to a value greater than that of the DML which causes the plasmoid to shrink. As the plasmoid had been expanding prior to this, this point marks the 1st maximum in the plot of plasmoid size (Figure 42 and Figure 43); the plasmoid is $132 R_E$ long at

this point. An Earthward travelling population can be seen ($200 - 270 R_E$, $0 - 1200 \text{ km s}^{-1}$) and the two separate tailward travelling population can be seen ($140 - 210 R_E$, $700 - 2000 \text{ km s}^{-1}$ and $210 - 270 R_E$, $1500 - 2200 \text{ km s}^{-1}$).

At $t = 1072$ seconds, the tailward travelling population (previously at the tailward end of the plasmoid) has been accelerated at the DML; in the case of the other population (the tailward travelling population previously at the Earthward end of the plasmoid), part of this population begins to interact with the DML; simultaneously part of that same population (near the NEML) is being accelerated by the NEML, the particles are accelerated without a change in direction and their post-acceleration tailward speed is between $1000 - 4000 \text{ km s}^{-1}$. In addition the Earthward travelling population (mentioned in $t = 784 \text{ s}$) begins to interact with the NEML. These populations increase the pressure in the direction away from the centre of the plasmoid leading to an expansion of the plasmoid, this point marks the 2nd minimum at $100 R_E$.

At $t = 1409$ seconds the plasmoid size reaches its 2nd maximum. A contribution is made to the subsequent plasmoid contraction by the particle velocity gradient; this is evident near the DML where the velocity of the interacting population decreases Earthward of the DML. This leads to a decreasing particle velocity, momentum and pressure of the population interacting with the DML, which slows down the DML and contracts the plasmoid. At $t \gg 1409$ seconds, the population and velocity distribution has equalised. It is clear from the plot that the tailward travelling particles have a greater average speed than the Earthward travelling particles.

4.4 Discussion

The formation of a plasmoid, as represented by a single closed loop of magnetic flux created by reconnection at two separate neutral lines, was modeled in a semi-realistic magnetic field, density and velocity gradient using a single particle numerical model, which is based on the principle of stress balance between the magnetic field tension and the change in particle momentum at a kink in the magnetic field centred on the current sheet. The model was run for 1.5 hours, representing the time for a typical plasmoid to be expelled from the Earth tail system.

Firstly, the typical interaction between magnetic loop ends and plasma is discussed. In the FLRF, the change in plasma momentum is balanced by the magnetic tension. A force is applied to the particles in the direction opposite to their initial direction of travel, resulting in a reversal in particle velocity in the FLRF. The velocity of the FLRF (which is also the magnetic loop end velocity in the ERF), depends on the balance of forces which in turn depends on the magnetic field strength, the inflow velocity in the ERF and the number of the particles interacting with the loop end.

At times when the dynamic plasma pressure (in the ERF) is greater than the magnetic tension, the magnetic loop end is pushed back in the ERF, in the direction opposite to the field tension. A particle interacting with the field line will be decelerated either with or without a change in direction. At times when the magnetic tension is greater than the dynamic plasma pressure (in the ERF), the magnetic loop end contracts. If a particle is travelling towards the contracting magnetic loop end (in the ERF), the

particle will be accelerated with a change in direction; if a particle is initially travelling in the same direction as the magnetic loop end and interacts (only possible if the magnetic loop end is moving faster than the particle) then the particle is accelerated with no change in direction.

At the beginning of a model run, all of the particles are travelling tailward and the plasma population has both a density and velocity gradient. The results show that the magnetic loop ends representing the plasmoid initially contract (shrinking the plasmoid) and accelerate any particles interacting with the loop ends. Once accelerated, these particles travel to the opposite end of the magnetic loop where their presence and enhanced momentum provides significant pressure to alter the balance of stresses. Due to the greater magnetic field strength at the NEML compared to the DML (at least during the initial stages of the model run), particles accelerated at the NEML have a greater outflow velocity and thus reach the other magnetic loop end earlier than their counterparts accelerated at the DML. The arrival of these particles (accelerated at the NEML) at the DML pushes the DML back in a tailward direction. Moreover, as there is a positive density gradient and negative magnetic field gradient (downtail), in the relatively near Earth tail, the NEML becomes increasingly slower as it migrates tailward due to the combined effect of the gradients on the stress balance (c.f. Alfvén speed reduces with distance). The tailward motion of the DML and the slowing down of the NEML are the cause of the plasmoid growth following the 1st minimum of the plasmoid size.

At the point in time at which the motion of the DML is reversed and it begins to move tailward, the acceleration of particles at this end of the

plasmoid ceases permanently. A small, localised population (that was accelerated at the DML prior to this point in time) travels Earthward, reaches the NEML and reverses the motion of the NEML temporarily whilst also ceasing the acceleration of particles at the NEML temporarily. When acceleration at the NEML resumes, a gap is present in the tailward population due to the temporary cessation of acceleration at the NEML.

This splits the population accelerated by the NEML into two (tailward travelling) populations, in addition both populations have a negative density gradient, the origin of which is explained as follows: The undisturbed population has a positive density gradient, hence the particles closest to the NEML have the lowest density and are accelerated first. They become the leading particles of the accelerated population (meaning they are located furthest tailward compared to the rest of the population, note they are travelling tailward). Any particles accelerated after the aforementioned particles have a greater density (due to the positive density gradient) and, as they are accelerated later, they will not be as far tailward as the leading particles. This gives the accelerated populations a negative density gradient; due to this, the density of the tailward travelling population at the Earthward end of the plasmoid is greater than the tailward travelling population at the tailward end; in addition to this, the density of the former population is increased by the arrival of the previously Earthward travelling population accelerated (with a reversal in direction) at the DML.

Once all of the initial undisturbed population has been accelerated, the NEML catches up to and interacts with this population. As the population

is faster after acceleration, the interaction of the NEML with the population post-acceleration, results in a faster loop end velocity than it had during its interaction with the then undisturbed population. The onset of this interaction causes the plasmoid to shrink and thus defines the 1st maximum in the plasmoid size.

As mentioned previously, the tailward travelling population is split in two, one at the Earthward end of the plasmoid and one at the tailward end. The population that was at the tailward end is accelerated at the DML, the population then travels Earthward to interact with the NEML, which has the effect of slowing the tailward motion of the NEML. At approximately the same time, the tailward travelling population initially at the Earthward end of the plasmoid, reaches and interacts with the DML, increasing the tailward speed of the DML. Both of these events contribute to the expansion of the plasmoid, such that the plasmoid size reaches a 2nd minimum at the onset of these events.

At some point later, the plasmoid reaches the 2nd maximum and begins to shrink once more. The accelerated populations possess a velocity gradient as a result of the loop ends moving down the negative magnetic and positive (undisturbed) particle density and velocity gradient of the lobe (leading to a reducing ERF outflow speed) and due to the velocity filter effect – where the faster particles travel ahead and the slower ones trail behind. The velocity gradient is most pronounced in the tailward travelling population. Overall, the decreasing velocity and thus momentum of particles interacting with the DML results in a decrease in the velocity of this end of the plasmoid, causing the plasmoid to contract once more. The

onset of this process marks the 2nd maximum. The accelerated tailward populations also contain a negative density gradient which would act to increase the speed of the DML with time (and expand the plasmoid) however its effect must not be as great as the velocity gradient at this time as the plasmoid shrinks in size.

The above explains the oscillation in loop end velocity and plasmoid size up to the 2nd plasmoid size maximum (which occurs at 25 minutes). A possible explanation for the subsequent oscillations is the movement of two populations in opposite directions to opposite ends of the plasmoid in anti-phase; this assumes the two populations have a similar mass, speed (in the frame of reference of the plasmoid) and that they interact with opposite loop ends at the same times. During the times they interact with the loop ends, they will apply a pressure directed away from the centre of the plasmoid and cause a temporary expansion of the plasmoid, once the populations have been accelerated and are no longer interacting with the loop end, the plasmoid will shrink. Both populations will then travel to the opposite loop end causing another plasmoid expansion. The interactions of the populations with the loop ends will also cause the NEML to decrease in tailward speed and the DML to increase in tailward speed, the opposite occurs immediately after the interaction, this could explain the loop end velocity traces which are sine waves in anti-phase. The results show two significant populations are seen moving oppositely to each other (at 1072 seconds in Figure 45) which cause the subsequent plasmoid expansion; observations of the oppositely directed populations passed the time of the 2nd maximum in plasmoid size (25 minutes) are difficult due to the degree of mixing of the populations.

Overall the particles within the plasmoid remain within identifiable groups during the first two cycles of the plasmoid size and loop end velocity oscillations. Thus the interactions of the groups can be relatively easily traced and their role in driving the plasmoid oscillations can be readily understood, as explained above. At later times, the identification of different groups is more problematic as a more complete mixing state is developed, interaction with the loop ends causes the particle populations to change from easily identifiable separate groups to a more uniform population. However, the same principles of stress balance are applied and the more uniform populations interacting with the loop ends result in a more steady evolution and motion, such that the early plasmoid oscillations, which are driven by the discrete groups, are seen to die away. The plasmoid thus reaches an equilibrium size and an equilibrium downtail velocity.

During the equilibrium phase ejection of the plasmoid down the tail, the mean plasmoid velocity and mean particle velocity must be equal, this is seen in Figure 42 and Figure 43. However, the mean particle speed remains higher than both the mean plasmoid velocity and mean particle velocity throughout the model run. Note that the velocity plots (Figure 44 and Figure 45) show that on average the tailward travelling population travels faster than the Earthward travelling population. The mean particle speed is derived from the sum of both the Earthward and tailward speeds, while the mean particle velocity is the vector addition of the Earthward and tailward velocities. The mean particle speed indicates that there is a net store of kinetic energy within the plasmoid which is available, through

interaction of particles with the loop ends, to drive the plasmoid structure continuously tailward. As the Earthward and tailward particle velocities are oppositely directed, they will partially cancel each other out with the result that the mean tailward particle velocity equals the mean plasmoid velocity.

Overall, the plasmoid travels tailward. Initially this is due to the magnetic gradient of the near-Earth tail. Particles are accelerated at both loop ends and gain momentum; particles accelerated at the NEML travel faster (after acceleration) than those accelerated at the DML due to the greater magnetic field strength at the NEML. The faster particles travel to the DML and push it back, which causes the population to be decelerated and lose momentum. Although the particles decelerated at the DML travel back to the contracting NEML, they do not have sufficient momentum to counter a rapid tailward motion of this magnetic loop end and are accelerated to high outflow speeds at this location, thus gaining momentum once more. The particles then travel towards the DML and the cycle continues. Overall, both magnetic loop ends thus travel tailward. Although the tailward movement of both loop ends is initially due to the magnetic gradient, the cycle of acceleration and deceleration (which transfers momentum tailward) causes the tailward movement of the plasmoid to continue after the plasmoid has moved out of the part of the lobe with a magnetic gradient ($X_{\text{GSM}} > 130 R_E$).

The mean particle velocity is an indicator of the energy of the particles within the plasmoid. This stops increasing when both field lines are out of the magnetic gradient. Hence in the cycle of acceleration and deceleration

there must be a net in gain energy whilst part of the plasmoid is within the magnetic gradient. Outside of the magnetic gradient there is no net gain in energy, hence the energy gained due to acceleration must be equal to the energy lost due to deceleration.

The mean particle speed can also be used as a proxy for energy. The coincidence of the peaks in mean particle speed with troughs of plasmoid size indicates a relationship between the two. The contraction of the magnetic loop causes a reduction in the net magnetic energy; the contraction also causes the acceleration of particles and hence an increase in particle energy. The opposite occurs when the magnetic loop expands. Thus total particle energy and mean particle speed are inversely proportional to the plasmoid size.

Comparing the model plasmoid to observational plasmoids highlights similarities and differences. The similarities include the evolution of the plasmoid with time. Moldwin and Hughes (1992) observed 366 plasmoids between 16 - 210 R_E downtail; they found plasmoids had an average size of 16.7 R_E and an average tailward velocity of 497 km s^{-1} . They split the tail into 3 bins ($X < 100 R_E$, near tail, $100 < X < 200 R_E$, middle tail, $X > 200 R_E$, distant tail) and found that the size and speed increases downtail. In the near, middle and distant tail, the average plasmoid size is 10, 16.5 and 19.5 R_E respectively and the average tailward plasmoid velocity is 373, 501 and 572 km s^{-1} respectively.

Ieda et al. (1998) surveyed 824 plasmoids between 50 - 250 R_E downtail, they found plasmoids had an average size of $\sim 10 R_E$. They found that plasmoid size increases from 4 R_E in diameter at $\sim 30 R_E$ downtail, to 10 R_E in diameter at 75 R_E downtail. The plasmoid size then dips to $\sim 9 R_E$ at 165 R_E before increasing back to $\sim 10 R_E$ at 200 R_E . They found that the speed increases from $\sim 300 \text{ km s}^{-1}$ at 30 R_E to $\sim 750 \text{ km s}^{-1}$ at 95 R_E , then decreases to $\sim 600 \text{ km s}^{-1}$ at 165 R_E at which point it becomes constant, indicated by a measurement of $\sim 600 \text{ km s}^{-1}$ at 200 R_E . The increase and subsequent decrease of plasmoid size and velocity is a pattern that is found in the early stages of the model. However the observations do not go far enough downtail to determine whether the plasmoid size and velocity continues to oscillate.

Scholer et al. (1984b) searched for plasmoids between 80 - 220 R_E using ISEE 3. They observed 20 plasmoids which had an average plasmoid size of $\sim 80 R_E$ with an average velocity of 600 km s^{-1} .

Comparing the three surveys, the latter observes much larger plasmoids (average size $\sim 80 R_E$) than the former two (average size $\sim 10 R_E$ and $\sim 16.7 R_E$). To compare the model results to observations, a survey of TCRs that include plasmoids and discounts flux bulges is required; while most of the studies do not separate plasmoids from flux bulges, the closest comparison that can be made is to surveys in a region of the tail where the greatest proportion of TCRs are caused by plasmoids. As mentioned in chapter 3, tailward of the DNL, TCRs are caused by either flux bulges formed by the DNL or plasmoids formed by both X-lines. Between the two X-lines, flux bulges form from the NENL and DNL. As there are two

sources of flux bulges in the region between the X-lines and only one tailward of the DNL; in the latter region, which is further downtail, a greater proportion of TCRs are expected to be caused by plasmoids compared to the region between the X-lines, hence the model results are compared to the survey with observations furthest downtail. The Earthward edge of the observation range of the Scholer et al. (1984b) study is $80 R_E$ downtail, this is further downtail than that of Moldwin and Hughes (1992) and Ieda et al. (1998), which is $16 R_E$ and $50 R_E$ respectively. Therefore the observations of Scholer et al. (1984b) are, on average, further downtail.

The model results are more comparable to studies conducted at distances further tailward, such as Scholer et al (1984b); in the study, 20 plasmoids were found between $80 - 220 R_E$ which had an average plasmoid size of $\sim 80 R_E$. Eight plasmoids were observed at the greatest downtail distances ($216 - 218 R_E$), four were between $34 - 75 R_E$ in diameter and four were between $105 - 146 R_E$ in diameter; for all eight, the diameter of the plasmoids are greater than the previously mentioned surveys. The size of model plasmoid is within the range of the observed plasmoids.

The model plasmoid has a size ($\sim 118 R_E$) and speed ($\sim 1000 \text{ km s}^{-1}$) that is greater than the average values found by the Scholer et al. (1984b) survey ($\sim 80 R_E$ and $\sim 600 \text{ km s}^{-1}$ respectively). The inclusion of omitted factors may lead to a smaller plasmoid; for example, the inclusion of a pre-existing plasma sheet outside of the structure would apply a pressure on the plasmoid leading to a slower, smaller plasmoid. Conversely, the inclusion of plasma sheet field lines at the core of the plasmoid would increase the

plasma pressure within the plasmoid; this will reduce the effect of magnetic tension and lead to a slower plasmoid. The inclusion of magnetic pressure would have the same effect as a greater magnetic tension and hence lead to a faster plasmoid.

The net plasmoid velocity ($\sim 1000 \text{ km s}^{-1}$) is greater than the range of the average observed value (497 - 600 km s^{-1}). One possible explanation is the lack of plasma sheet field lines within the model plasmoid. A plasmoid that includes plasma sheet field lines would contain more particles; more particles and hence more mass interacting with the magnetic loop ends will result in slower loop ends and hence a slower plasmoid.

4.5 Conclusions

Using a simple numerical particle model, the representative evolution of a plasmoid was followed over timescales corresponding to 1.5 hours. The plasmoid was represented by a simple closed magnetic loop and the model follows the current sheet interaction of particles trapped within the loop; the loop is initially formed from the reconnection of two lobe magnetic field lines, which are reconnected at neutral lines located at modeled downtail locations of $X = 25 R_E$ and $120 R_E$. The lobe particle density and velocity are set to increase linearly downtail from 0.00625 cm^{-3} and 138 km s^{-1} at $25 R_E$ respectively to 0.0775 cm^{-3} and 162 km s^{-1} at $120 R_E$. The magnetic field was set to reduce by $X^{-0.53}$ and decreased from 22.7 nT to 9.7 nT between $X = 25 R_E$ and $120 R_E$ respectively. The movement of the particles and magnetic loop ends (and hence the plasmoid) is governed by the stress balance conditions discussed in previous chapters.

Initially the two ends of the magnetic loop contract towards each other before both head tailward. The overall size of the plasmoid, defined as the distance between the two loop ends, initially grows as it moves downtail but then oscillates until reaching an equilibrium size of $118 R_E$. The particle population within the plasmoid is accelerated and split, the movement of these populations and their interaction with the loop ends causes the oscillation of the plasmoid size and velocity of the magnetic loop ends. Initially the oscillation is mostly due to the interaction of tailward travelling populations with the loop ends however after the 2nd maximum in plasmoid size, the oscillations are thought to be caused by the movement of two populations moving in opposite directions towards the

loop ends in anti-phase. As the populations become more evenly mixed, the oscillation damps and the plasmoid reaches an equilibrium size and constant velocity.

The plasmoid travels tailward, initially this is due to the magnetic gradient in the near-Earth tail. At the NEML, the magnetic field strength and hence velocity of the accelerated particles is greater than at the DML. Thus when particles accelerated at the NEML arrive at the DML, they push the DML back tailwards against the action of the field tension and cease the acceleration of particles at this end of the loop. The combination of a contracting NEML and receding DML leads to a net tailward velocity of the overall structure. Subsequently, the particles accelerated at the contracting NEML arrive at the receding DML and are decelerated, this transfers momentum from one end of the magnetic loop to the other and keeps the plasmoid moving tailward whilst the plasmoid is outside of the magnetic gradient. Outside of the magnetic gradient, the mean particle speed does not increase and hence the acceleration and deceleration of the particles leads to no net exchange of energy.

The mean plasmoid velocity increases sharply to 1450 km s^{-1} at $100 R_E$, then decreases sharply to 750 km s^{-1} at $250 R_E$, then oscillates whilst slowly increasing overall. The amplitude of the oscillation decreases and the plasmoid travels at a fairly constant velocity of 1000 km s^{-1} . Within the plasmoid, particles are moving both Earthward and tailward. The tailward particles generally have a greater speed than the Earthward travelling particles. However, the mean particle velocity is $\sim 1000 \text{ km s}^{-1}$ tailward

and is seen to be equal to the mean plasmoid velocity, as expected for a coherent field and plasma structure.

Chapter 5

Conclusions and Future Work

5.1 Conclusions

In this thesis, models and observations of the products of magnetic reconnection have been presented, the studies aim to better our understanding of the structures and their formation and evolution.

Chapter 2 presented multi-spacecraft observations of a TCR and the magnetic structure causing it at several different impact parameters, observed by the 4 Cluster spacecraft. The estimated velocity of the structure, calculated from the timing of distinct signatures, is $(99, 154, -31) |186| \text{ km s}^{-1}$ in GSM. The estimated size of the structure is $\sim 1.19 R_E$ in the direction of travel and is between 1.94 and $2.86 R_E$ in the direction perpendicular to the current sheet, assuming it is symmetrical about the current sheet.

C2 passed outside of the structure and observed a TCR. C1 and C4 passed through the structure at high impact parameters and C3 passed through the centre. C3 observed two plasma sheet drop-outs, between which, was a

region of CPS-like plasma (the latter is thought to be the PO region of the structure). The plasma sheet drop-outs are thought to be due to the passage of two X-lines past the spacecraft locations; coincident with the second drop-out, the spacecraft observes a rotation in the pitch angle of the ions from 0° to 180° which is consistent with the expected signature of a reconnecting X-line. The occurrence of magnetic reconnection is also indicated by the observation of parallel/anti parallel electron fluxes. The TCR is caused by the increase in pressure and expansion of the plasma between the X-lines in the direction perpendicular to the current sheet. Although the observations do not completely match the predictions of either the flux rope or flux bulge models, the observation of a region of CPS-like plasma between two plasma sheet drop-outs (interpreted as one active X-line and one dormant X-line) and a single TCR is evidence in favour of the multiple-X-line reconnection model.

Chapter 3 describes an adaptation to a simple single particle model of time-dependent reconnection in the magnetotail published by Owen and Cowley (1987). This previous model uses the cold plasma approximation to assess the stress balance conditions on reconnected field lines in the magnetotail. Although changes in the reconnection rate in this model lead to increases and decreases of the opening angle of the wedge of reconnected flux, it does not reproduce any localised thickening of the plasma sheet which is thought to be one of the causes of the ‘travelling compression regions’ (TCRs) regularly observed in the magnetotail lobes. In order to potentially produce such localised bulges and thus the TCR signatures in the model, the cold plasma approximation was relaxed by including a perpendicular plasma pressure to the particles forming the reconnection outflow jets.

This perpendicular pressure is assumed to arise from the pitch angle scattering of field-aligned inflow particles as they cross the current sheet on hairpin-like reconnected field lines. The study illustrated that under this assumption, for the field and plasma stresses to be balanced at greater pitch angles in the field line rest frame, a greater inflow particle velocity is required; as pitch angle increases the perpendicular velocity increases and the outflow velocity decreases until $\sim 58^\circ$ in the FLRF and 33° in the ERF, after which both increase. A limit of the maximum scattering of the initially field-aligned particles is found, this is $\sim 71^\circ$ in the FLRF and $\sim 36^\circ$ in the ERF.

The inclusion of a perpendicular pressure in the outflow plasma causes an expansion of the PO region perpendicular to the current sheet, which in turn leads to a compression of the lobe and thus potentially to a TCR if the reconnection rate varies with time. The study reports the signatures expected through the various regions of an Earthward travelling flux bulge created in the model. The bipolar B_Z signature of an Earthward TCR in this model has a positive excursion which is larger in magnitude and smaller in X distance than the negative excursion; when against time the excursions are of similar durations. Within the PO region, B_X peaks at the centre and B_Z peaks at the trailing end of the PO region. The study also examined the development of the structure with time after reconnection ceases. The difference in velocity between the accelerated particles and the recoiling field lines causes the structure to expand in the direction along the tail. This caused the positive and negative excursions of the bipolar signature to separate in time and space. The TCR and flux bulge may thus not be so readily identifiable in spacecraft observations if enough time has passed since formation.

Chapter 4 presents the results of a simple numerical particle model, used to model the evolution of a plasmoid over timescales corresponding to 1.5 hours. The plasmoid was modeled as a simple closed magnetic loop and the model follows the interaction of particles trapped within the loop with the hair-pin like magnetic field lines. The loop is created by the reconnection of two field lines at the neutral lines located at $X = 25 R_E$ and $120 R_E$. Gradients of the magnetotail were included in the model. The lobe particle density and velocity were set to increase linearly downtail from 0.00625 cm^{-3} and 138 km s^{-1} at $25 R_E$ respectively to 0.0775 cm^{-3} and 162 km s^{-1} at $120 R_E$ respectively. The magnetic field was set to reduce by $X^{-0.53}$ and fell from 22.7 nT to 9.7 nT between $25 R_E$ and $120 R_E$ respectively.

The movement of the particles and magnetic loop ends (and hence the plasmoid) is governed by the stress balance conditions. Initially the two ends of the magnetic loop contract towards each other, subsequently both head tailward. The overall size of the plasmoid, defined as the distance between the two loop ends, initially grows as it moves downtail but then oscillates until reaching an equilibrium size of $118 R_E$. The particle population within the plasmoid was accelerated and split, the movement of these populations and their interaction with the loop ends caused the oscillation of both the plasmoid size and the velocity of the magnetic loop ends. Initially the oscillation is dominated by the interaction of tailward populations with both loop ends however after 2nd maximum in plasmoid size, the oscillations are thought to be caused by the movement of two populations moving in opposite directions towards the loop ends in anti-

phase. As the populations become more evenly mixed, the oscillation damps and the plasmoid reached an equilibrium size and constant velocity.

The plasmoid travelled tailward, initially this is due to the magnetic gradient in the near-Earth tail. At the NEML the magnetic field strength and hence velocity of the accelerated particles was greater than at the DML. Thus when particles accelerated at the NEML arrive at the DML, they push the DML back tailwards against the action of the field tension and cease the acceleration of particles at this end of the loop. The combination of a contracting NEML and receding DML leads to a net tailward velocity of the overall structure as shown in Figure 42. Subsequently, the particles accelerated at the contracting NEML arrived at the receding DML and were decelerated, thus transferring momentum from one end of the magnetic loop to the other and thus keeping the plasmoid moving tailward whilst the plasmoid is outside of the magnetic gradient. Once outside of the magnetic gradient, the mean particle speed did not increase and hence the acceleration and deceleration of the particles lead to no net exchange of energy.

The mean plasmoid velocity increased sharply to 1450 km s^{-1} at $100 R_E$, then decreased sharply to 750 km s^{-1} at $250 R_E$, then oscillates whilst slowly increasing overall. The amplitude of the oscillation decreases and the plasmoid travels at a fairly constant velocity of 1000 km s^{-1} . Within the plasmoid, particles were moving both Earthward and tailward. The tailward particles generally have a greater speed than the Earthward travelling particles. However, the mean particle velocity was $\sim 1000 \text{ km s}^{-1}$

tailward and was seen to be equal to the mean plasmoid velocity, as expected for a coherent field and plasma structure.

5.2 Future work

There are several possible ways to extend and improve on the work of this thesis. Firstly, the observational chapter can be extended by identifying and analysing many more such events in which the Cluster spacecraft simultaneously observe the different regions within and around a travelling magnetic structure. A statistically significant number of events would be needed to properly determine the mode (or modes) of reconnection operating in the tail (and if relevant, their relative probability of occurrence). Alternatively, a further observational study may find structures, like the event studied in Chapter 2, which does not fully match the flux rope or flux bulge directly. If a prevalence of such results were found, it would suggest the need to develop an alternative model for the formation of such structures.

The flux bulge study presented in Chapter 3 could be extended in many ways to include more realistic model scenarios. For example, it would be relatively straightforward to investigate the effect of asymmetrical inflows (from the north and south tail), as was done for the cold case by Owen and Cowley (1987b). The study could also be extended by seeking to remove or relax some of the limitations and omissions within the current version. These could include removing the need to make the small angle approximation, such that the model could be extended to other contexts, or considering the effect of non-zero thermal pressure of the field aligned

inflow. In the latter case this would allow us to include the effect on the bulge structure of reconnection initially occurring on pre-existing plasma sheet field lines before moving onto the lobes.

The existence of flux bulges could be tested by using THEMIS (Angelopoulos 2008) observations. The data from this spacecraft could be used to identify flux bulges and observe the time evolution of the structure as the 5 THEMIS spacecraft all have ecliptic orbits around the Earth with different radii. At times when the spacecraft are aligned along X (all have the same Y value), the observations of an Earthward or tailward moving structure at different spacecraft will occur at significantly different times. The THEMIS spacecraft cover a distance range of $20 R_E$, the greatest time between observations would be on the scale of minutes whereas the Cluster spacecraft separations are $\leq 10,000$ km which results in observations separated by seconds. With this greater separation in time between observations, THEMIS may be more suited to identifying the temporal evolution of flux bulges and plasmoids, and perhaps, the oscillations associated with the plasmoid.

For a more complete model of a plasmoid than that presented in Chapter 4, multiple nested magnetic loops really need to be taken into consideration. This would then allow the exploration of the effect of the reconnection rates at the two neutral lines. This would require the inclusion of magnetic pressure variations along the current sheet, and would also likely require relaxing the small angle approximation. The inclusion of magnetic pressure would allow the modeling of smaller scale magnetic loops like flux ropes.

The plasmoid model could also be adapted to fold in the analysis presented in Chapter 3 by incorporating a change in the pitch angle (the heating of the outflow) as the particles cross the current sheet. This would result in a pitch angle distribution for particles within the plasmoid, and would result in an expansion of the plasmoid in the direction normal to the current sheet, which can be followed with time after multiple crossings of the current sheet. The effect of lobe density, lobe velocity, magnetic gradient and the pitch angle on the size in Z could be explored. If lobe magnetic field lines (that are not part of the plasmoid) are included in the model, then the TCR (and change in TCR with downtail distance and time) can be recorded. The inclusion of an initial population of plasma sheet plasma would also be a useful, more realistic addition to such an extension of the model presented in Chapter 4. This could be done by setting the first few reconnected magnetic field lines (and the plasma on them) to plasma sheet values. Another possible addition to the model is the plasma of the plasma sheet outside of the plasmoid; this would apply pressure to the plasmoid affecting its movement.

Chapter 6

Appendix

6.1 Bipolar signature database

The bipolar signature that is the subject of study of Chapter 2 was found by searching the Cluster data by eye between 2006 - 2007. A shortlist of bipolar signatures was compiled and the most intriguing bipolar signature was analysed during the course of the work presented in Chapter 2. The others were not studied in depth but are listed below as reference for other researchers who may wish to extend such analysis. Two lists have been created, the bipolar signatures of the top list are larger and clearer than those of the bottom list and are hence better candidates for study.

Number	Year	Month	Date	Time (UT)
1	2006	06	8	2012
2	2007	06	16	1848
3	2007	07	3	0324
4	2007	07	3	0326
5	2007	07	3	1622
6	2007	07	3	1627
7	2007	09	15	0203

Table 2: List of dates and times of largest and clearest bipolar signatures observed by Cluster between 2006 - 2007.

Number	Year	Month	Date	Time (UT)
1	2006	06	08	2018
2	2006	10	24	2019
3	2006	10	29	0241
4	2007	06	13	1949
5	2007	06	13	1952
6	2007	06	23	2137
7	2007	06	28	1252
8	2007	07	01	0540
9	2007	07	03	0323-0327
10	2007	09	29	0334
11	2007	09	29	0350
12	2007	10	28	1242
13	2007	10	30	0236
14	2007	11	11	1355
15	2007	11	11	1400
16	2007	10	26	0500-0900

Table 3: List of dates and times of additional bipolar signatures observed by Cluster between 2006 - 2007.

6.2 Distribution Functions

This section of the appendix calculates the effective perpendicular plasma pressure of mono-energetic, mono-pitch angle particles gyrating around a field line. This requires the distribution function of the population, which is assumed to be a Dirac delta function for simplicity. The Dirac delta function $\delta(x)$ was introduced by Paul Dirac (Dirac, 1958); it is a function which is infinite at the origin and 0 everywhere else:

$$\delta(x) \begin{cases} +\infty, & x = 0 \\ 0, & x \neq 0 \end{cases} \quad (6.1)$$

The integration of the Dirac delta function is equal to unity:

$$\int_{-\infty}^{+\infty} \delta(x) dx = 1 \quad (6.2)$$

The Dirac delta function satisfies the sifting property:

$$\int_{-\infty}^{+\infty} f(x) \delta(x - a) = f(a) \quad (6.3)$$

As mentioned previously, the particles are all travelling at the same velocity (v_i) and so one factor of the distribution function is a delta function with respect to velocity: $f(v) \propto \delta(v - v_i)$. The particles also all have the same pitch angle (α_i) so one factor of the distribution function is a delta function with respect to pitch angle: $f(\alpha) \propto \delta(\alpha - \alpha_i)$. The plasma pressure is assumed to be gyrotropic and so f is independent of gyrophase θ . Combining the two dependencies and including a constant, the distribution becomes:

$$f(\mathbf{v}) = k. \delta(v - v_i) \delta(\alpha - \alpha_i). \quad (6.4)$$

Calculating the pressure requires evaluating the triple integral in spherical polar coordinates in the form:

$$I = \int_0^{2\pi} \int_0^\pi \int_0^\infty f(r, \theta, \phi) r^2 \sin\theta \, dr \, d\theta \, d\phi \quad (6.5)$$

In the above, ϕ is the azimuthal angle in the X-Y plane, with $\phi = 0$ pointing along the positive x axis; θ is the polar angle between r and z , with $\theta = 0$ aligned along the positive Z axis. As this involves integrating in velocity space, r is replaced with v . In velocity space, the angle between the velocity vector and the magnetic field (assumed to point along the positive Z direction) is the pitch angle α , equivalent to the angle, θ above, while ϕ represents the gyrophase angle. Hence the triple integral becomes:

$$I = \int_0^{2\pi} \int_0^\pi \int_0^\infty f(v, \alpha, \phi) v^2 \sin\alpha \, dv \, d\alpha \, d\phi \quad (6.6)$$

Before calculating the pressure, the density must first be calculated. Using the equations from Paschmann et al. (2000):

$$n = \int f(\mathbf{v}) d^3\mathbf{v} \quad (6.7)$$

Where \mathbf{v} is the velocity vector and $d^3\mathbf{v}$ is the volume element. By substituting the volume element in spherical polar coordinates, which is $d^3\mathbf{v} = v^2 \sin\alpha \, dv \, d\alpha \, d\phi$, and the distribution function, which is $f(\mathbf{v}, \alpha, \phi) = k \cdot \delta(v - v_i) \cdot \delta(\alpha - \alpha_i)$, the density becomes:

$$n = \int_0^{2\pi} \int_0^\pi \int_0^\infty f(v, \alpha, \phi) v^2 \sin\alpha \, dv \, d\alpha \, d\phi \quad (6.8)$$

$$n = \int_0^{2\pi} \int_0^\pi \int_0^\infty k \delta(v - v_i) \delta(\alpha - \alpha_i) v^2 \sin\alpha \, dv \, d\alpha \, d\phi \quad (6.9)$$

$$n = k \int_0^{2\pi} d\phi \int_0^\infty \delta(v - v_i) v^2 dv \int_0^\pi \delta(\alpha - \alpha_i) \sin\alpha \, d\alpha \quad (6.10)$$

$$n = 2\pi k v_i^2 \sin \alpha_i \quad (6.11)$$

For stress balance calculations, an equation for the effective pressure perpendicular to the field line, caused by the gyration of a particle is required. The magnetic field is assumed to be directed in Z and the pressure is derived for a component perpendicular to the field (X is used in this case). For a particle with pitch angle α and gyrophase angle φ , the X component of its motion is:

$$v_X = v \sin \alpha \cos \varphi \quad (6.12)$$

Using the equations from Paschmann et al. (2000):

$$P = m \int f(\mathbf{v})(\mathbf{v} - \mathbf{v}_i)(\mathbf{v} - \mathbf{v}_i) d^3 \mathbf{v} \quad (6.13)$$

where \mathbf{v}_i is the bulk velocity and is equal to zero as the plasma is frozen-in and does not move perpendicular to the field line, hence:

$$P = m \int f(\mathbf{v}) \mathbf{v} \mathbf{v} d^3 \mathbf{v}$$

$$P_X = m \int_0^{2\pi} \int_0^\pi \int_0^\infty f(\mathbf{v}) [v^2 \sin^2 \alpha \cos^2 \varphi] [v^2 \sin \alpha dv d\alpha d\varphi] \quad (6.14)$$

From equation 6.4: $f(\mathbf{v}) = k \cdot \delta(v - v_i) \delta(\alpha - \alpha_i)$.

$$P_X = mk \int_0^{2\pi} \cos^2 \varphi d\varphi \int_0^\infty \delta(v - v_i) v^4 dv \int_0^\pi \delta(\alpha - \alpha_i) \sin^3 \alpha d\alpha \quad (6.15)$$

$$P_X = mk\pi v_i^4 \sin^3 \alpha_i \quad (6.16)$$

From equation 6.11: $n = 2\pi k v_i^2 \sin \alpha_i$

$$P_X = \frac{1}{2} n m v_i^2 \sin^2 \alpha_i \quad (6.17)$$

6.3 Stress Balance

The following is the rearrangement of the stress balance equation from Chapter 3.

$$V_o'^2 \left[(1 + \cos \alpha) - \frac{1 \sin^2 \alpha}{2 \cos \alpha} \right] = \frac{B^2}{n_{in} m \mu_o} = V_A^2 \quad (6.18)$$

$$1 + \cos \alpha - \frac{1 \sin^2 \alpha}{2 \cos \alpha} = \frac{2 \cos \alpha + 2 \cos^2 \alpha - \sin^2 \alpha}{2 \cos \alpha} \dots$$

$$\dots = \frac{2 \cos \alpha + 2 \cos^2 \alpha - (1 - \cos^2 \alpha)}{2 \cos \alpha} = \frac{3 \cos^2 \alpha + 2 \cos \alpha - 1}{2 \cos \alpha} \quad (6.19)$$

$$V_o'^2 \left[\frac{3 \cos^2 \alpha + 2 \cos \alpha - 1}{2 \cos \alpha} \right] = V_A^2 \quad (6.20)$$

$$V_o'^2 = V_A^2 \left[\frac{2 \cos \alpha}{3 \cos^2 \alpha + 2 \cos \alpha - 1} \right] \quad (6.21)$$

$$V_o' = V_A \left[\frac{2 \cos \alpha}{3 \cos^2 \alpha + 2 \cos \alpha - 1} \right]^{\frac{1}{2}} \quad (6.22)$$

$$V_o' = V_A \left[\frac{2 \cos \alpha}{(3 \cos \alpha - 1)(\cos \alpha + 1)} \right]^{\frac{1}{2}} \quad (6.23)$$

6.4 Forces at an interface

Reconnected field lines have a kink at the current sheet; the expansion of the PO region leads to another kink in the field at the PO boundary. The following proves that the pressures at a lobe field kink of a field line with a single kink centred on the current sheet, are equal to the sum of the pressures at the field kinks of a field line with one kink centred on the PO boundary and one at the current sheet within a PO region.

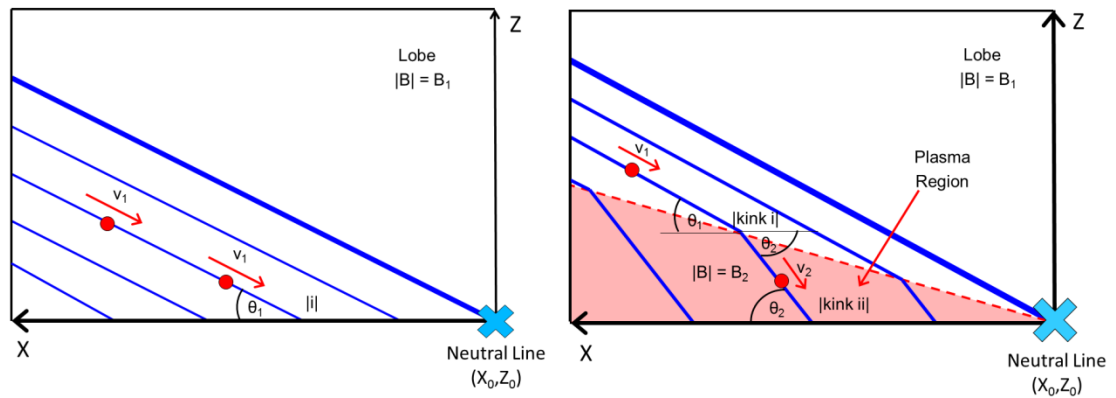


Figure 46: Figure showing magnetic field lines (in blue) and particles (red circles). The left panel shows the lobe which has a magnetic field strength of B_1 . The reconnected field lines in the diagram are at an angle of θ_1 , the kink of the field line is labelled $|i|$. The right panel shows the lobe (with B_1 and θ_1) and the heated PO region (pink shaded area where the magnetic field strength is B_2 and field lines are at an angle of θ_2), the heated PO region causes an additional kink in the field line labelled $|j|$.

Figure 46 shows the tail with and without a PO region, the magnetic field lines are in blue and the particles are the red circles. The left panel shows the lobe which has a magnetic field strength is B_1 . The field lines in the diagram are reconnected field lines at an angle of θ_1 to the current sheet, the kink at the current sheet is labeled $|i|$. The plasma has a density of n_1 and a velocity of v_1 . The pressures at this kink, resolved in the X direction are:

$$P_B = -\frac{B_1^2}{\mu_0} \cos\theta_1 \quad P_P = +n_1 m v^2 \cos\theta_1 \quad (6.24)$$

where P_B is the pressure caused by the magnetic field (in this case this is the magnetic tension) and P_P is the dynamic plasma pressure.

The right panel shows the lobe (with magnetic field strength and field angle of B_1 and θ_1 respectively) and the heated PO region (pink shaded area where the magnetic field strength is B_2 and the field angle is θ_2). The field lines in this panel have two kinks, one at the PO boundary |i| and one at the current sheet |ii|. The plasma initially has a density and velocity of n_1 and v_1 . After interaction with kink |i| the plasma has a density and velocity of n_2 and v_2 . The pressures resolved in X at the kink |i| are:

$$P_B = -\frac{B_1^2}{\mu_0} \cos\theta_1 + \frac{B_2^2}{\mu_0} \cos\theta_2$$

$$P_P = n_1 m v_1^2 \cos\theta_1 - n_2 m v_2^2 \cos\theta_2 \quad (6.25)$$

The pressures resolved in X at the kink |ii| are:

$$P_B = -\frac{B_2^2}{\mu_0} \cos\theta_2 \quad P_P = +n_2 m v_2^2 \cos\theta_2 \quad (6.26)$$

And the sum of the pressures, resolved in X, at both kinks is:

$$P_B = -\frac{B_1^2}{\mu_0} \cos\theta_1 \quad P_P = +n_1 m v^2 \cos\theta_1 \quad (6.27)$$

The equations show that the pressures at the field kink of the lobe field line with a single kink are equal to the sum of the pressures at the field kinks of a field line with one kink at the PO boundary and one at the current sheet within the PO region. As the pressure in the two scenarios is equal, the

simpler scenario of a reconnected lobe field line with a single kink at the current sheet will be used for the pressure calculations of the hot particle model.

6.5 Solution to Cubic Equation

The method for finding the roots of a cubic equation was obtained from Press et al. (1992). For a cubic equation:

$$x^3 + ax^2 + bx + c = 0 \quad (6.28)$$

where a, b and c can be real or complex. The first step is to calculate:

$$Q \equiv \frac{(a^2-3b)}{9} \text{ and } R \equiv \frac{2a^3-9ab+27c}{54} \quad (6.29)$$

If Q and R are real (which is the case when a, b, c are real) and $R^2 < Q^3$, then the cubic equation has three real roots. These can be found by calculating:

$$\theta = \arccos\left(\frac{R}{\sqrt{Q^3}}\right) \quad (6.30)$$

The three roots of the cubic equation are:

$$x_1 = -2\sqrt{Q} \cos\left(\frac{\theta}{3}\right) - \frac{a}{3} \quad (6.31)$$

$$x_2 = -2\sqrt{Q} \cos\left(\frac{\theta+2\pi}{3}\right) - \frac{a}{3} \quad (6.32)$$

$$x_3 = -2\sqrt{Q} \cos\left(\frac{\theta-2\pi}{3}\right) - \frac{a}{3} \quad (6.33)$$

Otherwise, calculate:

$$A = - \left[R + \sqrt{R^2 - Q^3} \right]^{-\frac{1}{3}} \quad (6.34)$$

Where the sign of the square root is chosen to make:

$$Re(R^* \sqrt{R^2 - Q^3}) \geq 0 \quad (6.35)$$

(the asterix denotes a complex conjugate). If Q and R are both real, equations 6.34 and 6.35 are equivalent to:

$$A = -sgn(R) \left[|R| + \sqrt{R^2 - Q^3} \right]^{\frac{1}{3}} \quad (6.36)$$

where the positive square root is assumed. Then calculate:

$$B = \begin{cases} \frac{Q}{A} & (A \neq 0) \\ 0 & (A = 0) \end{cases} \quad (6.37)$$

The three roots are then:

$$x_1 = (A + B) - \frac{a}{3} \quad (6.38)$$

The above is the single real root when a,b,c are real and:

$$x_2 = -\frac{1}{2}(A + B) - \frac{a}{3} + \frac{i\sqrt{3}}{2}(A - B) \quad (6.39)$$

$$x_3 = -\frac{1}{2}(A + B) - \frac{a}{3} - \frac{i\sqrt{3}}{2}(A - B) \quad (6.40)$$

the above are the complex roots. Equations 6.34 - 6.37 are arranged to minimize roundoff error and to ensure that no choice of branch for the complex cube can result in the spurious loss of a distinct root.

Bibliography

Akasofu, S.-I., C-I. Meng, and D. S. Kimball, 5599 Dynamics of the aurora, 4, Polar magnetic substorms and westward traveling surges, *J. Atmos. Terr. Phys.*, 28, 489-496, 1966a.

Angelopoulos, V. (2008), The THEMIS Mission, *Space Sci. Rev.*, 141, 5–34, doi:10.1007/s11214-008-9336-1.

Baker, D. N., Pulkkinen, T. I., Angelopoulos, V., Baumjohann, W., and McPherron, R. L.: Neutral line model of substorms: Past results and present view, *J. Geophys. Res.*, 101, 12 975–13 010, 1996.

Balogh, A., Carr, C. M., Acuna, M. H., Dunlop, M. W., Beek, T. J., Brown, P., Fornaçon, K.-H., Georgescu, E., Glassmeier, K.-H., Harris, J., Musmann, G., Oddy, T., and Schwingenschuh, K.: The Cluster Magnetic Field Investigation: overview of in-flight performance and initial results, *Ann. Geophys.*, 19, 1207– 1217, 2001.

Baumjohann, W., G. Paschmann, N. Sckopke, C. A. Cattell, and C. W. Carlson (1988), Average Ion Moments in the Plasma Sheet Boundary Layer, *J. Geophys. Res.*, 93(A10), 11,507–11,520, doi:10.1029/JA093iA10p11507.

Baumjohann, W., G. Paschmann, and C. A. Cattell (1989), Average Plasma Properties in the Central Plasma Sheet, *J. Geophys. Res.*, 94(A6), 6597–6606, doi:10.1029/JA094iA06p06597.

<http://www.agu.org/pubs/crossref/1989/JA094iA06p06597.shtml>

Baumjohann, W. and Treumann, R. A.: *Basic Space Plasma Physics*, Imperial College Press, 1997.

- Beyene, S., Owen, C. J., Walsh, A. P., Forsyth, C., Fazakerley, A. N., Kiehas, S., Dandouras, I., and Lucek, E.: Cluster observations of a transient signature in the magnetotail: implications for the mode of reconnection, *Ann. Geophys.*, 29, 2131-2146, doi:10.5194/angeo-29-2131-2011, 2011.
- Biernat, H. K., M. F. Heyn, and V. S. Semenov (1987), Unsteady Petschek reconnection, *J. Geophys. Res.*, 92, 3392-3396.
- Cowley, S. W. H. (1980) Plasma populations in a simple open model magnetosphere. *Space Sci. Rev.* 25, 217.
- de Hoffman, F. and Teller, E. (1950) Magneto-hydrodynamic shocks. *Phys. Rev.* 80,692.
- Dirac, P. A. M. *Principles of Quantum Mechanics*, London: Oxford University Press, 1958.
- Dungey, J. W.: Interplanetary Magnetic Field and the Auroral Zones, *Phys. Rev. Lett.*, 6, 47–48, 1961.
- Dungey, J. W.: The length of the geomagnetic tail, *J. Geophys. Res.*, 70, 1753, 1965.
- Eastman, T. E., L. A. Frank, W. K. Peterson, and W. Lennartsson (1984), The Plasma Sheet Boundary Layer, *J. Geophys. Res.*, 89(A3), 1553–1572, doi:10.1029/JA089iA03p01553.
- Elphic, R. C., Cattell, C. A., Takahashi, K., Bame, S. J., and Russell, C. T.: ISEE-1 and 2 observations of magnetic flux ropes in the magnetotail: FTEs in the plasma sheet?, *Geophys. Res. Lett.*, 13, 648–651, 1986.
- Escoubet, C. P., Fehringer, M., and Goldstein, M.: The Cluster mission, *Ann. Geophys.*, 19, 1197-1200, 2001.

Forsyth, C., Lester, M., Fear, R. C., Lucek, E., Dandouras, I., Fazakerley, A. N., Singer, H., and Yeoman, T. K.: Solar wind and substorm excitation of the wavy current sheet, *Ann. Geophys.*, 27, 2457-2474, doi:10.5194/angeo-27-2457-2009

Ganushkina, N. Y., I. Dandouras, Y. Y. Shprits, and J. Cao (2011), Locations of boundaries of outer and inner radiation belts as observed by Cluster and Double Star, *J. Geophys. Res.*, 116, A09234, doi:10.1029/2010JA016376.

Goldstein, J., M. Spasojević, P. H. Reiff, B. R. Sandel, W. T. Forrester, D. L. Gallagher, and B. W. Reinisch (2003), Identifying the plasmopause in IMAGE EUV data using IMAGE RPI in situ steep density gradients, *J. Geophys. Res.*, 108, 1147, doi:10.1029/2002JA009475. Hoshino et al., 1987

Gosling, J. T., D. N. Baker, S. J. Bame, E. W. Hones, D. J. McComas, R. D. Zwickl, J. A. Slavin, E. J. Smith, and B. T. Tsurutani, Plasma entry into the distant tail lobes: ISEE-3, *Geophys. Res. Lett.*, 11, 1078, 1984.

Hapgood, M. A., T. G. Dimbylow, D.C. Sutcliffe, P. A. Chaizy, P. S. Ferron, P. M. Hill and X. Tiratay, The Joint Science Operations Centre, *Space Sci. Rev.*, 79, 487, 1997

Harra, L. K. and Mason, K. O., *Space Science*, Imperial College Press, 2004

Hautz, R. and M. Scholer (1987), Numerical simulations on the structure of plasmoids in the deep tail, *Geophys. Res. Lett.*, 14(9), 969–972, doi:10.1029/GL014i009p00969.

Henderson, P. D., Owen, C. J., Alexeev, I. V., Slavin, J., Fazakerley, A. N., Lucek, E., and Reme, H.: Cluster observations of flux rope structure in the

near tail, *Ann. Geophys.*, 24, 651–666, 2006, <http://www.ann-geophys.net/24/651/2006/>.

Hones, E. W. Jr., D. N. Baker, S. J. Bame, W. C. Feldman, J. T. Gosling, D. J. McComas, R. D. Zwickl, J. A. Slavin, E. J. Smith, and B. T. Tsurutani, Structure of the magnetotail at 220 RE and its response to geomagnetic activity, *Geophys. Res. Lett.*, 11, 5, 1984.

Hughes, W. J., and D. G. Sibeck, On the 3-dimensional structure of plasmoids, *Geophys. Res. Lett.*, 14, 636, 1987.

Ieda, A., Machida, S., Mukai, T., Saito, Y., Yamamoto, T., Nishida, A., Terasawa, T., and Kokubun, S.: Statistical analysis of the plasmoid evolution with Geotail observations, *J. Geophys. Res.*, 103, 4453–4466, 1998.

Imber, S. M., J. A. Slavin, H. U. Auster, and V. Angelopoulos (2011), A THEMIS survey of flux ropes and traveling compression regions: Location of the near -Earth reconnection site during solar minimum, *J. Geophys. Res.*, 116, A02201, doi:10.1029/2010JA016026

Ivanova, V., Liu, J., Kiehas, S., Semenov, V., and Biernat, H.: Inverse reconstruction technique based on time-dependent Petschek-type reconnection model: first application to THEMIS magnetotail observations, *Ann. Geophys.*, 27, 4369-4377, doi:10.5194/angeo-27-4369-2009,

Johnstone, A. D., Alsop, C., Burdge, S., Carter, P. J., Coates, A. J., Coker, A. J., Fazakerley, A. N., Grande, M., Gowen, R. A., Gurgiolo, C., Hancock, B. K., Narheim, B., Preece, A., heather, P. H., Winningham, J. D., and Woodcliffe, R. D.: PEACE, A Plasma Electron and Current Experiment, *Space Sci. Rev.*, 79, 351–398, 1997.

Kiehas, S. A., Semenov, V. S., Kubyshkin, I. V., Tolstykh, Yu. V., Penz, T., and Biernat, H. K.: Effects of a moving X-line in a time-dependent reconnection model, *Ann. Geophys.*, 25, 293-302, doi:10.5194/angeo-25-293-2007, 2007

Kiehas, S. A., V. S. Semenov, M. V. Kubyshkina, V. Angelopoulos, R. Nakamura, K. Keika, V. V. Ivanova, H. K. Biernat, W. Baumjohann, S. Mende, W. Magnes, U. Auster, K.-H. Fornacon, D. Larson, C. W. Carlson, J. Bonnell, and J. McFadden, First Application of a Petschek-type Reconnection Model with Time-Varying Reconnection Rate to THEMIS Observations, *J. Geophys. Res.*, 114, A00C20, doi:10.1029/2008JA013528, 2009.

Kistler, L. M., F. M. Ipavich, D. C. Hamilton, G. Gloeckler, B. Wilken, G. Kremser, and W. Stüdemann (1989), Energy Spectra of the Major Ion Species in the Ring Current During Geomagnetic Storms, *J. Geophys. Res.*, 94(A4), 3579–3599, doi:10.1029/JA094iA04p03579.

Lee, L. C., and Z. F. Fu (1985), A theory of magnetic flux transfer at the Earth's magnetopause, *Geophys. Res. Lett.*, 12, 105–108, doi:10.1029/GL012i002p00105

Lepping, R. P., Jones, J. A., and Burlaga, L. F.: Magnetic Field Structure of Interplanetary Magnetic Clouds at 1 AU, *J. Geophys. Res.*, 95, 11 957–11 965, 1990.

McPherron, R. L. (1970), Growth Phase of Magnetospheric Substorms, *J. Geophys. Res.*, 75(28), 5592–5599, doi:10.1029/JA075i028p05592.

Millan and Baker, 2012, Acceleration of Particles to High Energies in Earth's Radiation Belts, *Space Sci. Rev*, 173, 103-131, 2012

Moldwin, M.B., and W.J. Hughes, On the formation and evolution of plasmoids: a survey of ISEE 3 geotail data, submitted to *J. Geophys. Res.*, 1992a.

Moldwin, M. B., and W. J. Hughes , Observations of Earthward and tailward propagating flux rope plasmoids: Expanding the plasmoid model of geomagnetic substorms, *J. Geophys. Res.*, 99, 183, 1994.

Mulligan, T. and Russell, C. T.: Multispacecraft modeling of the flux rope structure of interplanetary coronal mass ejections: Cylindrically symmetric versus nonsymmetric topologies, *J. Geophys. Res.*, 106, 10 581–10 596, doi:10.1029/ 2000JA900170, 2001.

Nagai, T., Nakamura, R., Mukai, T., Yamamoto, T., Nishida, A., and Kokubun, S.: Substorms, tail flows and plasmoids, *Advances in Space Research*, 20, 961-971, doi:10.1016/S0273-1177(97)00504-8, 1997

Neagu, E., J. E. Borovsky, S. P. Gary, A. M. Jorgensen, W. Baumjohann, and R. A. Treumann (2005), Statistical survey of magnetic and velocity fluctuations in the near-Earth plasma sheet: International Sun Earth Explorer (ISEE-2) measurements, *J. Geophys. Res.*, 110, A05203, doi:10.1029/2004JA010448

Owen, C. J. and Cowley, S. W. H. (1987) Simple models of time-dependent reconnection in a collision-free plasma with an application to substorms in the geomagnetic tail. *Planet. Space Sci.* 35,451.

Owen, C. J., and S. W. H. Cowley (1987b), A note on current sheet stress balance in the geomagnetic tail for asymmetrical tail lobe plasma conditions, *Planet. Space Sci.*, 35,467–474, doi:10.1016/0032-0633(87)90103-6.

- Owen, C. J., Slavin, J. A., Fazakerley, A. N., Dunlop, M. W., and Balogh, A.: Cluster electron observations of the separatrix layer during traveling compression regions, *Geophys. Res. Lett.*, 32, L03 104, 2005.
- Parker, E. N.: Sweet's Mechanism for Merging Magnetic Fields in Conducting Fluids, *J. Geophys. Res.*, 62, 509–520, 1957.
- Paschmann, G. and Daly, P.: Eds. Analysis Methods for Multi-Spacecraft Data, ISSI Science Report, SR-001, 1998.
- Paschmann, G., Fazakerley, A. N., and Schwartz, S. J.: Moments of Plasma Velocity Distributions, in *Analysis Methods for Multi-Spacecraft Data*, edited by G. Paschmann and P. W. Daly, pp. 125-158, ISSI, 1.1 edn., 2000.
- Petschek, H. E. (1964), Magnetic field annihilation, in *Physics of Solar Flares*, edited by W. N. Hess, NASA Spec. Publ., 50 , pp. 425 – 439.
- Phillips, J. L., Bame, S. J., Feldman, W. C., Goldstein, B. E., Gosling, J. T., Hammond, C. M., McComas, D. J., Neugebauer, M., Scime, E. E., and Suess, S. T.: Ulysses Solar Wind Plasma Observations at High Southerly Latitudes, *Science*, 268, 1030–1033, 1995.
- Press, Flannery, Teukolsky, and Vetterling, *Numerical Recipes in C*, 2nd Edition, (1992, Cambridge University Press)
- Pilipp, W. G., and G. Morrill, The formation of the plasma sheet resulting from plasma mantle dynamics, *J. Geophys. Res.*, 83, 5670, 1978.
- Price, C. P., and D. W. Swift (1986), Ion Tearing Mode Simulations with Open Boundary Conditions, *J. Geophys. Res.*, 91(A11), 11,993–12,004, doi:10.1029/JA091iA11p11993.
- Priest, E. R.: The Sun and its Magnetohydrodynamics, in *Introduction to SpacePhysics*, edited by M. G. Kivelson and C. T. Russell, pp. 58{90, Cambridge Un-versity Press, 1st edn., 1995. Seki et al., 2000

Reiff, P. H., T. W. Hill, and J. L. Burch (1977), Solar Wind Plasma Injection at the Dayside Magnetospheric Cusp, *J. Geophys. Res.*, 82(4), 479–491, doi:10.1029/JA082i004p00479.

Rème, H., Aoustin, C., Bosqued, J. M., Dandouras, I., Lavraud, B., Sauvaud, J. A., Barthe, A., Bouyssou, J., Camus, T., Coeur-Joly, O., Cros, A., Cuvilo, J., Ducay, F., Garbarowitz, Y., Medale, J. L., Penou, E., Perrier, H., Romefort, D., Rouzaud, J., Vallat, C., Alcayd, D., Jacquy, C., Mazelle, C., d'Uston, C., Mobius, E., Kistler, L. M., Crocker, K., Granoff, M., Mouikis, C., Popecki, M., Vosbury, M., Klecker, B., Hovestadt, D., Kucharek, H., Kuenneth, E., Paschmann, G., Scholer, M., Sckopke, N., Seidenschwang, E., Carlson, C. W., Curtis, D. W., Ingraham, C., Lin, R. P., McFadden, J. P., Parks, G. K., Phan, T., Formisano, V., Amata, E., Bavassano-Cattaneo, M. B., Baldetti, P., Bruno, R., Chionchio, G., Lellis, A. D., Marcucci, M. F., Pallocchia, G., Korth, A., Daly, P. W., Graeve, B., Rosenbauer, H., Vasyliunas, V., McCarthy, M., Wilber, M., Eliasson, L., Lundin, R., Olsen, S., Shelley, E. G., Fuselier, S., Ghielmetti, A. G., Lennartsson, W., Escoubet, C. P., Balsiger, H., Friedel, R., Cao, J.-B., Kovrazhkin, R. A., Papamastorakis, I., Pellat, R., Scudder, J., and et al., B. S.: First multispacecraft ion measurements in and near the Earth's magnetosphere with the identical Cluster ion spectrometry (CIS) experiment, *Ann. Geophys.*, 19, 1303–1354, 2001.

Rich, F. J., Vasyliunas, V. M. and Wolf, R. A. (1972) On the balance of stresses in the plasma sheet. *J. geophys. Res.* 77, 4670.

Richardson, I. G., S. W. H. Cowley, E. W. Hones Jr., and S. J. Bame (1987), Plasmoid-Associated Energetic Ion Bursts in the Deep Geomagnetic Tail: Properties of Plasmoids and the Postplasmoid Plasma

Sheet, J. Geophys. Res., 92(A9), 9997–10,013,
doi:10.1029/JA092iA09p09997.

Rosenbauer, H., H. Grfinwaldt, M.D. Montgomery, G. Paschmann, and N. Sckopke, Heos 2 plasma observations in the distant polar magnetosphere: The plasma mantle, J. Geophys. Res., 80, 2723, 1975.

Runov, A., Sergeev, V. A., Baumjohann, W., Nakamura, R., Apatenkov, S., Asano, Y., Volwerk, M., Vörös, Z., Zhang, T. L., Petrukovich, A., Balogh, A., Sauvaud, J.-A., Klecker, B., and Rème, H.: Electric current and magnetic field geometry in flapping magnetotail current sheets, Ann. Geophys., 23, 1391-1403, 2005.

Schindler, K.: A Theory of the Substorm Mechanism, J. Geophys. Res., 79, 2803–2810, 1974.

Scholer, M., G. Gloeckler, B. Klecker, F. M. Ipavich, D. Hovestadt, and E. J. Smith, Fast moving plasma structures in the distant magnetotail, J. Geophys. Res., 89, 6717, 1984.

Schödel, R., Baumjohann, W., Nakamura, R., Sergeev, V. A., and Mukai, T.: Rapid flux transport in the central plasma sheet, JGR, 106, 301–314, 2001.

Sckopke, N., G. Paschmann, H. Rosenbauer, and D. H. Fairfield, Influence of the interplanetary magnetic field on the occurrence and thickness of the plasma mantle, J. Geophys. Res., 81, 2687, 1976

Semenov, V. S., Heyn, M. F. and Kubyshkin, I. V., Reconnection of magnetic field lines in a nonstationary case, Sov. Astron., 27, 660–665, 1983a.

- Semenov, V. S., I. V. Kubyshkin, M. F. Heyn, and H. K. Biernat (1984), Temporal evolution of the convective plasma flow during a reconnection process, *Adv. Space Res.*, 4, 471–474.
- Semenov, V. S., Vasilyev, E. P., and Purovkin, A. I., A scheme for the non-steady reconnection of magnetic lines of force, *Geomagnet. Aeronomy (Engl. Transl.)*, 24, 370–373, 1984.
- Sergeev, V. A., Tsyganenko, N. A., and Angelopoulos, V.: Dynamical response of the magnetotail to changes of the solar wind direction: an MHD modeling perspective, *Ann. Geophys.*, 26, 2395-2402, doi:10.5194/angeo-26-2395-2008, 2008
- Shelley, E. G., R. D. Sharp, and R. G. Johnson (1976), He⁺⁺ and H⁺ Flux Measurements in the Day Side Cusp: Estimates of Convection Electric Field, *J. Geophys. Res.*, 81(13), 2363–2370, doi:10.1029/JA081i013p02363.
- Sibeck, D. G., R. E. Lopez, and E. C. Roelof (1991), Solar Wind Control of the Magnetopause Shape, Location, and Motion, *J. Geophys. Res.*, 96(A4), 5489–5495, doi:10.1029/90JA02464.
- Slavin, J. A., B. T. Tsurutani, E. J. Smith, D. E. Jones, and D. G. Sibeck (1983), Average configuration of the distant (<220 Re) magnetotail: Initial ISEE-3 magnetic field results, *Geophys. Res. Lett.*, 10(10), 973–976, doi:10.1029/GL010i010p00973.
- Slavin, J. A., E. J. Smith, B. T. Tsurutani, D. G. Sibeck, H. J. Singer, D. N. Baker, J. T. Gosling, E. W. Hones, and F. L. Scarf (1984), Substorm associated traveling compression regions in the distant tail: Isee-3 Geotail observations, *Geophys. Res. Lett.*, 11(7), 657–660, doi:10.1029/GL011i007p00657.

Slavin, J. A., Smith, E. J., Sibeck, D. G., Baker, D. N., and Zwickl, R. D.: AnISEE 3 study of average and substorm conditions in the distant magnetotail, *J. Geophys. Res.*, 90, 10 875, 1985.

Slavin, J. A., Smith, M. F., Mazur, E. L., Baker, D. N., Iyemori, T., Singer, H. J., and Greenstadt, E. W.: ISEE 3 plasmoid and TCR observations during an extended interval of substorm activity, *Geophys. Res. Lett.*, 19, 825–828, 1992

Slavin, J. A., Smith, M. F., Mazur, E. L., Baker, D. N., Hones Jr., E. W., Iyemori, T., and Greenstadt, E. W.: ISEE 3 observations of traveling compression regions in the Earth's magnetotail, *J. Geophys. Res.*, 98, 15 425–15 446, 1993

Slavin, J. A., C. J. Owen, and M. Hesse (1994), Evolution of the plasmoid-lobe interaction with downtail distance, *Geophys. Res. Lett.*, 21(24), 2765–2768, doi:10.1029/94GL02442.

Slavin, J. A., C. J. Owen, M. M. Kuznetsova, and M. Hesse (1995), ISEE 3 observations of plasmoids with flux rope magnetic topologies, *Geophys. Res. Lett.*, 22(15), 2061–2064, doi:10.1029/95GL01977.1995

Slavin, J. A., Hesse, M., Owen, C. J., Taguchi, S., Fairfield, D. H., Lepping, R. P., Kokubun, S., Mukai, T., Lui, A. T. Y., Anderson, R. R., Matsumoto, H., and Sutcliffe, P. R.: Dual spacecraft observations of lobe magnetic field perturbations before, during and after plasmoid release, *Geophys. Res. Lett.*, 26, 2897-2900, doi:10.1029/1999GL003606, 1999.

Slavin, J. A., Lepping, R. P., Gjerloev, J., Fairfield, D. H., Hesse, M., Owen, C. J., Moldwin, M. B., Nagai, T., Ieda, A., and Mukai, T.: Geotail observations of magnetic flux ropes in the plasma sheet, *J. Geophys. Res.*, 108, 1015-1032, 2003a.

Slavin, J. A., Lepping, R. P., Gjerloev, J., Goldstein, M. L., Fairfield, D. H., Acuna, M. H., Balogh, A., Dunlop, M., Kivelson, M. G., Khurana, K., Fazakerley, A., Owen, C. J., Reme, H., and Bosqued, J. M.: Cluster electric current density measurements within a magnetic flux rope in the plasma sheet, *Geophys. Res. Lett.*, 30, 1362-1365, 2003b.

Slavin, J. A., Owen, C. J., Dunlop, M. W., Boralv, E., Moldwin, M. B., Sibeck, D. G., Tanskanen, E., Goldstein, M. L., Fazakerley, A., Balogh, A., Lucek, E., Richter, I., Reme, H., and Bosqued, J. M.: Cluster four spacecraft measurements of small traveling compression regions in the near-tail, *Geophys. Res. Lett.*, 30, 2208–2211, 2003c.

Slavin, J. A., E. I. Tanskanen, M. Hesse, C. J. Owen, M. W. Dunlop, S. Imber, E. A. Lucek, A. Balogh, and K.-H. Glassmeier (2005), Cluster observations of traveling compression regions in the near-tail, *J. Geophys. Res.*, 110, A06207, doi:10.1029/2004JA010878.

Slinker, S. P., J. A. Fedder, and J. G. Lyon (1995), Plasmoid formation and evolution in a numerical simulation of a substorm, *Geophys. Res. Lett.*, 22(7), 859–862, doi:10.1029/95GL00300.

Sonnerup, B. U. Ö. and Cahill, L. J.: Magnetopause structure and attitude from Explorer 12 observations, *J. Geophys. Res.*, 72, 171-183, 1967.

Sonnerup, B. U. Ö. and Scheible, M.: Minimum and maximum variance analysis, in: *Analysis Methods for Multi-Spacecraft Data*, edited by: Paschmann, G. and Daly, P., pp. 185–220, ESA, Noordwijk, 1998.

Van Allen, J.A.: 1958, *Radiation Belts around the Earth*. San Francisco, Freeman.

- Walker, R. C., U. Villante, and A. J. Lazarus (1975), Pioneer 7 Observations of Plasma Flow and Field Reversal Regions in the Distant Geomagnetic Tail, *J. Geophys. Res.*, 80(10), 1238–1244, doi:10.1029/JA080i010p01238.
- Walsh, A. P., Fazakerley, A. N., Wilson, R. J., Alexeev, I. V., Henderson, P. D., Owen, C. J., Lucek, E., Carr, C., and Dandouras, I.: Near-simultaneous magnetotail flux rope observations with Cluster and Double Star, *Ann. Geophys.*, 25,1887-1897, 2007.
- Zhang, T. L., Baumjohann, W., Nakamura, R., Balogh, A., and Glassmeier, K.-H.: A wavy twisted neutral sheet observed by CLUSTER, *Geophys. Res. Lett.*, 29, 5-1, 2002.
- Zong, Q.-G., Fritz, T. A., Pu, Z. Y., Fu, S. Y., Baker, D. N., Zhang, H., Lui, A. T., Vogiatzis, I., Glassmeier, K.-H., Korth, A., Daly, P. W., Balogh, A., and Reme, H.: Cluster observations of Earthward flowing plasmoid in the tail, *Geophys. Res. Lett.*, 31, L18 803, doi:10.1029/2004GL020692 , 2004
- Zwickl, R. D., D. N. Baker, S. J. Bame, W. C. Feldman, J. T. Gosling, E. W. Hones Jr., D. J. McComas, B. T. Tsurutani, and J. A. Slavin (1984), Evolution of the Earth's Distant Magnetotail: ISEE 3 Electron Plasma Results, *J. Geophys. Res.*, 89(A12), 11,007–11,012, doi:10.1029/JA089iA12p11007.